A numerical study of shear jamming

Varghese Babu

A thesis presented for the degree of
Doctor of Philosophy

JNCASR

Theoretical Science Unit
Jawaharlal Nehru Center for Advanced Scientific Research
India
August 22, 2023

Declaration

I hereby declare that the matter embodied in the thesis entitled "A numerical study of shear jamming" are the results of the investigations carried out by me at the Theoretical Science Unit, Jawaharlal Nehru Center for Advanced Scientific Research, Bangalore, India, under the supervision of Prof. Srikanth Sastry and the same has not been submitted elsewhere for any other degree.

In keeping with the general practice in reporting scientific observations, due acknowledgment has been made whenever the work described is based on the findings of other investigators.

VARGHESE BABU

Certificate

I hereby certify that the matter embodied in this thesis entitled "**A numerical study of shear jamming**" has been carried out by Mr. Varghese Babu at the Theoretical Sciences Unit, Jawaharlal Nehru Centre for Advanced Scientific Research, Bangalore, India under my supervision and that it has not been submitted elsewhere for the award of any degree or diploma.

Supervisor
PROF. SRIKANTH SASTRY

Synopsis

This is a summary of the work done in the thesis titled “A numerical study of shear jamming” by Varghese Babu.

The jamming transition in granular matter is an example of a transition from a flowing to a rigid state in the absence of any significant structural rearrangement. This is typically observed in granular matter when density of the system is increased. This transition, although superficially similar to the freezing transition, cannot be explained by a similar equilibrium statistical mechanics approach as used for freezing, but some advances have been made in recent times. Development of a theory to understand jamming and the related glass transition has received extensive attention, with numerical simulations playing a major role.

The compression driven jamming transition has been well studied in frictionless sphere packings. Another way to bring about the jamming transition is using shear deformation, which has been experimentally observed. This thesis concerns with numerical observation of frictionless shear jamming transition, its relation to the isotropic jamming transition. In addition we also study the relation of frictionless shear jamming with frictional shear jamming.

The work is organised as follows

1. **Chapter 1**: This chapter motivates the problem of glass and jamming transition. We present hard-sphere model as a simple model to study the jamming transition. In addition to hard spheres, much work has been devoted to studying the soft sphere model in elucidating critical behaviour near the jamming transition, and the unusual solid state that one has close to it. We present an interesting property of the force and inter-particle gap distributions due to the stability of the jammed sphere packings against compression. We briefly describe corresponding results when frictional systems are considered. We review the shear jamming transition observed in experiments and previous numerical results on shear jamming in frictionless systems.

2. **Chapter 2**: In this chapter we describe in detail how shear jamming can be observed in well-annealed frictionless soft-sphere systems. We show that shear jamming is a conjugate phenomena to dilatancy - the tendency of granular materials to expand under shear. In particular we show that shear jamming occurs when materials are sheared at constant volume and dilatancy is observed when materials are sheared at constant pressure. Therefore our results show that friction is not necessary to observe dilatancy as previously thought. A generalized phase diagram for system at steady state shear is also presented.

3. **Chapter 3**: In this chapter we characterize the criticality of the shear jamming transition in frictionless soft-spheres. The criticality of isotropic jamming is well studied and displays many signs of a second order transition. Our results show shear jamming transition shares the critical features with isotropic jamming. In addition we find that the shear jammed configurations are marginally stable as well.

4. **Chapter 4**: In this chapter we study the rigidity transition of the contact network associated with shear jamming of frictional and frictionless disks. The rigidity transition associated with isotropic jamming in frictionless disks is strongly discontinuous while available work on frictional shear jamming suggest a continuous transition. Given the results of the previous chapter on the similarities of shear jamming and isotrpic jamming, we study the nature of rigidity transition associated with shear jamming. We find that for frictional systems sheared at a finite rate the transition appears continuous in agreement with previous results. This transition becomes "sharper" as the shear rate is lowered and under quasi-static shear the frictional as well as frictionless disk packings display a clearly discontinuous rigidity transition similar to that observed in isotropic jamming mentioned earlier.

5. **Chapter 5**: In this chapter we discuss the conclusions from our work. We summarize our results regarding shear jamming transition and indicate a few interesting directions that can be pursued.

Contents

Chapter 1

Introduction

1.1 Introduction

We are all familiar with phase transitions. Phase transition of a material involves a significant change in the nature of the material, like how water freezes to ice. The drastic change observed at the macroscopic level during this transition is reflected at the microscopic level as well where the molecular arrangement changes from being random (*i.e disordered*) (water) to an organized lattice (ice). From the point of view of statistical mechanics, such transitions are rather well understood in the language of equilibrium thermodynamics. When one takes a close look at the molecules, let us say in water, we see that they are always in thermal motion. This thermal motion continuously changes the arrangement of molecules in the system. These systems are in *equilibrium* and are *ergodic*. Therefore one can in principle calculate the free energy of these materials from equilibrium statistical mechanics and understand that phase transition occurs when one phase becomes more stable than the other, where a more stable phase will have smaller free energy. The calculation of free energy involves an average over all possible configurations accessible to the system at a given state point (say temperature and volume).

Now we consider another set of familiar materials where a similar transition from a flowing to a rigid state occurs. Granular materials like sand can be observed to exist in a rigid or a flowing state. How does this transition between flowing and rigid states compare with freezing of water? Comparison of water and sand is certainly quite a stretch, sand particles are significantly larger than water molecules. They are not affected by temperature, they do not undergo thermal fluctuations. A configuration of sand (arrangement) will stay as it is unless disturbed mechanically. Therefore any notion of an ensemble of states is only possible under external agitation, which is unusual. Due to these differences, behaviour of materials like sand and other granular materials cannot be explained using equilibrium statistical mechanics.

A related class of materials also displays a transition from a flowing to a solid state without any significant change in the structure is glass. Glass transition occurs when a liquid is cooled rapidly such that the system cannot rearrange itself into a crystalline state, but the viscosity diverges such that it behaves like a solid. A glass is a liquid that has lost its ability to flow.

This glass transition and the jamming transition represent a challenge to our understanding of materials through equilibrium statistical mechanics. Development of a theory to understand glass and jamming transition has been undertaken over the years. This thesis is a study of the jamming transition occurring under shear deformation. In this chapter, I summarise the existing understanding of the field with a focus on the jamming transition. We will start our discussion from the hard-sphere system which serves as a simple model where many if not all phenomena we discuss can be observed.

1.2 Jamming in Hard-spheres

One of the simplest models for studying the jamming, glass and freezing transition is the hard-sphere model. Hard-spheres are defined as spherical particles with inter-particle interaction defined by the following potential

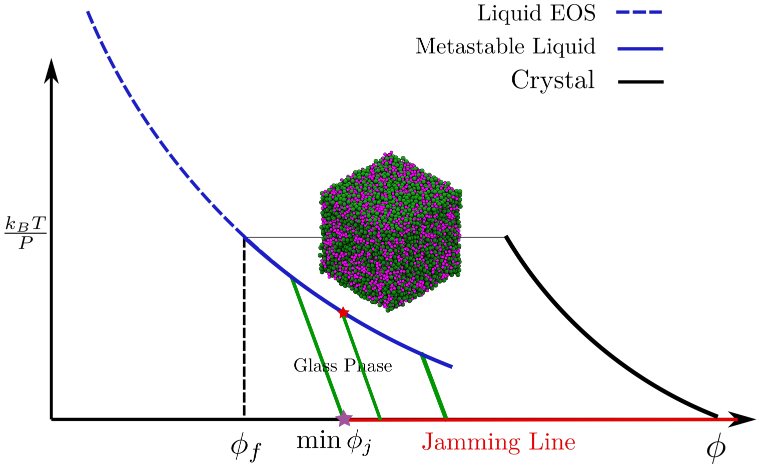

Figure 1.1: Schematic phase diagram for hard-spheres. ϕ_f is the freezing transition where the crystal becomes the stable phase. Configurations on the metastable liquid line can leave the equilibrium line and enter the glass phase depending on the compression rate. The configurations can only be compressed till the pressure diverges, which indicates the jamming point. Depending on the compression rate, jamming can happen on the jamming line indicated in red. The red star on the metastable liquid line shows a configuration of bi-disperse sphere packing.

$$v\left(|\vec{r}_{ij}|\right) = \begin{cases} \infty & |\vec{r}_{ij}| \leq \sigma_{ij} \\ 0 & |\vec{r}_{ij}| > \sigma_{ij} \end{cases} \tag{1.1}$$

where $\vec{r}_{ij}$ is the vector connecting the centers of the particles and $\sigma_{ij} = \frac{\sigma_i+\sigma_j}{2}$ with σ_i being the diameter of the particle. This potential means that a configuration of hard-sphere is such that there are no overlaps between the particles. Despite the simplicity the physics captured by the model is rich and serves as a concrete system in which one can observe many features related to crystal nucleation, metastable liquid, glasses, and jamming [1]. Therefore it is instructive to describe the behavior of this model in detail. An important feature of the HS system is that due to the nature of the potential, temperature does not play any role in the behavior of the system other than a simple rescaling of the velocities and the important variable in the system is ϕ or the packing efficiency.

Note that the free energy of hard-spheres is solely dependent on the entropy as $F = U - TS$, and $U = 0$ for hard-spheres. Therefore the equilibrium state for hard-spheres is the state with higher entropy or a more possible valid state. For concreteness let us consider the hard-sphere system in $d = 3$. The pressure of the hard-sphere system is given by [2]

$$p = \frac{P}{\rho k_B T} = 1 + \frac{2\pi}{3}\sigma^3 \rho g(\sigma^+) \tag{1.2}$$

where σ is the diameter of the hard-sphere $g(r)$ is the pair-correlation function, $g(\sigma^+)$ indicates the value $\lim_{r\to\sigma^+} g(r)$. Derivation of this equation can be found in [2] page 33. The equation of state

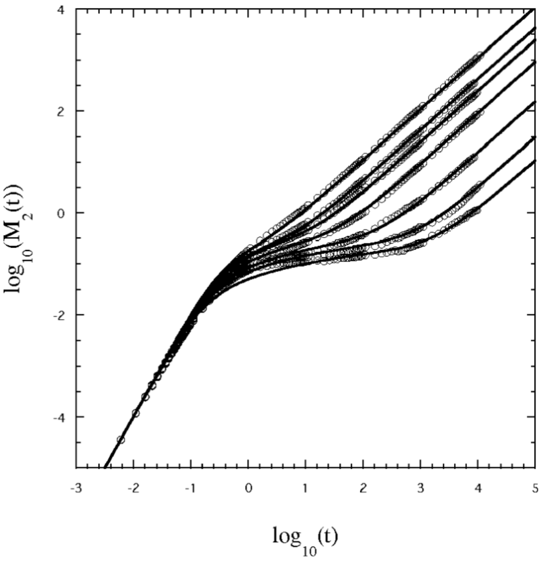

Figure 1.2: Mean-Squared Displacement ($M_2(t)$) for hard spheres in 3D with polydispersity. The densities goes from $\phi = 0.51$ to $\phi = 0.585$ (left to right) showing the emergence of a plateau. Figure taken from [4] with permission.

for the equilibrium hard-sphere liquid can be described by the Carnahan-Starling equation which is given by [3]

$$Z = \frac{PV}{Nk_BT} = \frac{1+\phi+\phi^2-\phi^3}{(1-\phi)^3}. \tag{1.3}$$

At low enough densities ($\phi < \phi_f = 0.494$) the system behaves as a fluid, with the pressure of the system being given by the value on the equation of state as shown in the Fig. 1.1. As one compresses the system the pressure increases and the system follows the equation of state along the dashed blue shown in Fig. 1.1. At lower densities, the entropy of the disordered configurations is more than the entropy of ordered ones and therefore the disordered state is the thermodynamically stable state. However as the density is increased at a certain point, the entropy of disordered configurations becomes lower than that of crystalline configurations. Beyond that point, crystal becomes the thermodynamically stable configuration. This packing fraction is ϕ_f or the freezing density. The liquid phase and the crystal phase are separated by a free energy barrier due to the need for a nucleation event. Therefore, unless a nucleation takes the system over the barrier to the crystal phase, the system remains in the liquid state. This is called a metastable liquid. This is indicated by the solid blue line in Fig. 1.1. At this density, it is instructive to look at the mean-squared displacement of the particles in the system. The mean squared displacement is defined as

$$\Delta(t) = \langle r(t)^2 \rangle = \frac{1}{N}\sum_{i=1}^{N} \left\langle |\boldsymbol{x}_i(t) - \boldsymbol{x}_i(0)|^2 \right\rangle$$

The mean square displacement gives the average displacement a particle undergoes for a given time interval. For the liquid state the MSD has two regimes (which can be readily seen from molecular dynamics simulation) of HS system: Ballistic for short intervals and diffusive for long intervals. As we compress the metastable liquid further, taking care that we avoid crystallization, the MSD will show a third intermediate regime as shown in Fig. 1.2. The ballistic regime at short times where the MSD increases as t^2 and the diffusive regime where MSD increases as t are separated by a plateau as one looks at the dynamics of dense supercooled liquids. The presence of the plateau implies a time period where the particle does not move significantly. This is usually described as by formation of cages around particles by other particles which by themselves are trapped in cages. The eventual diffusive motion happens when the cages are broken and the particles escape. This is the same behavior captured by $F_s(\vec{q}, t)$ when liquids undergo glass transition.

The appearance of the plateau is a signature of the approaching glass transition. As one goes to higher densities the length of the plateau increases exponentially. At a certain stage, the length of the plateau becomes larger than the experimental time. At this density we have a glass. Therefore the glass transition density depends on the experimental time scale. If we compress the glassy state further, then the pressure vs ϕ line deviates from the EOS as seen in Fig. 1.1, because we are not letting the system equilibrate as we compress. We can continue the compression till the pressure of the system diverges. This is the "**Jamming point**".

The jamming point described is not unique due to the fact that the glass transition density defined by the experimental time scale. Slower compression implies longer experimental times. Then the glass transition will be encountered at larger densities because we can observe the equilibration of the system. This in turn will lead us to a higher jamming density. This is the idea of jamming line. The density at which pressure diverges depends on the density of the equilibrated supercooled liquid from which we started the compression. In this thesis we will use ϕ_j to represent any value of the jamming point with $\phi_J = \min \phi_j$. This is represented by the red line in Fig. 1.1. Even though the density of the jamming point is not unique the properties of the jamming point remain the same [5, 6].

Hard-sphere are a simple model and can be easily studied numerically using monte carlo simulations. However due to the discontinuous nature of the interaction potential (Eq. 1.1), numerical schemes which involve the calculation of forces needs to be modified to study HS systems. For performing molecular dynamics simulations of hard-spheres an event driven algorithm has to be used [7].

As mentioned, the jamming transition is identified for hard-spheres as the point where pressure diverges. This transition point has many interesting properties which we will discuss now. We will study the jamming transition approaching the jamming point from the jammed region using the soft-sphere model. As we will see, one gets a solid with very interesting properties near the transition. In addition, because of the above mentioned numerical difficulties, it will be useful to study a more numerically tractable model to understand the jamming transition.

1.3 Soft-Sphere model

In the soft-sphere model, the interaction between particles is

$$v\left(|\vec{r}_{ij}|\right) = \epsilon \left(1 - \frac{|\vec{r}_{ij}|}{\sigma_{ij}}\right)^{\alpha} \Theta\left(\sigma_{ij} - |\vec{r}_{ij}|\right) \tag{1.4}$$

where σ_{ij} is $\frac{\sigma_i + \sigma_j}{2}$ with $\alpha \geq 2$. The value of α depends on the model chosen, in this thesis we will use $\alpha = 2$ which puts a harmonic repulsion between spheres. If $\alpha = 5/2$, then the model is Hertzian. Therefore, in the soft-sphere model, the particles are allowed to overlap at an energy cost. This allows us to compress the configurations beyond the jamming point. This model has been extensively used to study the jamming transition [8, 9]. We remark that soft-sphere configuration at zero potential energy implies zero overlaps and is therefore a valid HS configuration. Numerically, compression is carried out by a rescaling of the particle co-ordinates followed by an energy minimization. Such configurations are therefore always at a minimum of the potential energy landscape. Once we compress beyond the jamming point ϕ_j, there are no more HS configurations that are accessible. Therefore the energy minimization will not minimize the energy to zero (no overlaps) but to a finite energy [8]. Therefore for soft-spheres the jamming point can be identified as the point at which the potential energy of the configurations becomes non-zero. This is identical to the point at which the pressure of HS configurations diverge. We study jamming transition in the athermal limit $T = 0$.

By compressing the soft-sphere potential to densities above the jamming density we can study the jamming point from above. Also, the soft-sphere potential makes analysis of the configurations easier compared to HS systems. For soft-spheres we can define two particles to be in contact if there is an overlap between them and therefore a force acting between the particles. The criticality of the jamming transition can be demonstrated elegantly on the soft-sphere system. Unlike the glass transition which is defined using an experimentally accessible timescale, the jamming transition can be identified unambiguously from the non-zero pressure and shows many features of a genuine phase transition [9, 8]. Consider the average co-ordination number defined as $Z = \frac{2N_c}{N}$ where N_c is the number of contacts and N is the number of particles in the system. At the jamming point ϕ_j Z jumps from 0 to $2D = Z_{iso}$ which is the isostatic value. This means the number of degrees of freedom in the system is equal to the number of contacts in the system [8, 9, 10]. The number of degrees of freedom in the system is $D \times N$, and therefore

$$Z = \frac{2 \times N_c}{N} = \frac{2DN}{N} = 2D = Z_{iso} \tag{1.5}$$

As one compresses soft-spheres beyond the jamming density ϕ_j we can study how various quantities scale as a function of $(\phi - \phi_j)$. The virial pressure P scales as $P \sim (\phi - \phi_j)$ and the excess contact number $\delta Z = Z - Z_{iso} \sim (\phi - \phi_j)^{\frac{1}{2}}$ [9, 8]. An important point to note here is that while calculating the average co-ordination number one has to exclude the “rattlers”. Rattlers are particles that are not part of the force-network that sustains the pressure. Numerically, they can be identified as particles with less than $D + 1$ contacts.

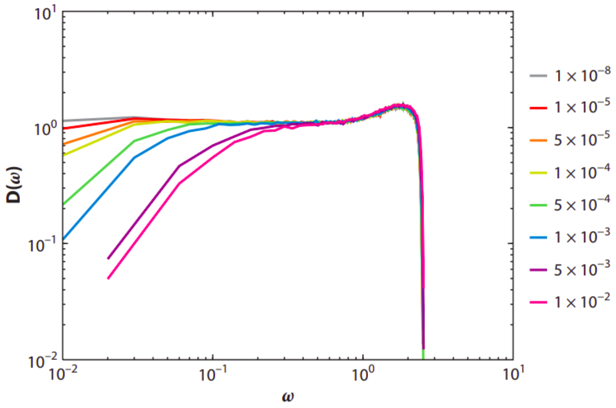

Figure 1.3: Density of state $D(\omega)$ near the jamming transition ϕ_J. The graphs from right to left are for $\Delta\phi = 10^{-2}$ to 10^{-8} where $\Delta\phi = \phi - \phi_J$. It can be seen that near ϕ_J there are many low-energy excitations possible in the system. The system is therefore at the threshold of stability. Image taken from [12] with permission.

Similar scalings are observed for the bulk modulus K and shear modulus G. For the potential Eq. 1.4 the following is observed

$$K \sim (\phi - \phi_j)^0 \tag{1.6}$$

$$G \sim (\phi - \phi_j)^{\frac{1}{2}}. \tag{1.7}$$

Therefore K remains non-zero while G is zero at the jamming point. This difference between K and G has been attributed to the fact that G is more sensitive to non-affine effects [11].

Density of states

One of the most studied and interesting aspects of the jamming transition is the behavior of the vibrational density of states (VDOS) $D(\omega)$. For a crystalline solid, the density of states for small ω goes as ω^{D-1} as calculated from the number of phonon modes in the Debye model. Soft spheres near the jamming transition are characterized by excess low energy modes compared to the Debye solid. This means that close to the jamming transition system is increasingly “soft”. The behavior of $D(\omega)$ close to the jamming transition is shown in Fig. 1.3. As shown in the figure, for configurations very close to jamming, there exist normal modes for $\omega \to 0$ which shows how the system is sensitive to very low energy perturbation. $D(\omega)$ is computed by diagonalizing the Hessian of a jammed soft-sphere packing and computing the distribution of the $\omega_i = \sqrt{\lambda_i}$ where λ_i is an eigenvalue of the Hessian. For a system of particles interacting with an inter-particle potential $v\left(|\vec{r}_{ij}|\right)$ where $\vec{r}_{ij}$ is the vector separating particles i and j, we can define the Hessian. Here the potential of the whole system is

$$V\left(\{\vec{R}_i\}\right) = \sum_{i<j} v(|\vec{r}_{ij}|) \tag{1.8}$$

For a system at a potential energy minimum (in the absence of thermal fluctuations (or at really low temperatures) if we leave the system "be", then it will go to a potential energy minimum) we can calculate the change in energy for small displacements from the minima. We can therefore expand Eq. 1.8 in $\{\delta\vec{R}_i\}$,

$$V\left(\{\vec{R}_i\}\right) - V_0 = \vec{\nabla}V|_{\{\vec{R}_i\}}.\delta\vec{R} + \sum_{ij} \delta\vec{R}_i.\frac{\partial V}{\partial\vec{R}_i\partial\vec{R}_j}|_{\{\vec{R}_i\}}.\delta\vec{R}_j$$

where the first term on the R.H.S is zero because the system is at the energy minima and the second term is a $dN \times dN$ matrix which is the Hessian of the system. The Hessian can be computed as follows. Denoting

$$t_{ij} = \frac{\partial v(r_{ij})}{\partial r_{ij}}; c_{ij} = \frac{\partial^2 v(r_{ij})}{\partial r_{ij}^2}$$

the Hessian is given by [13]

$$H_{ij}^{\alpha\beta} = \begin{cases} -\left(c_{ij} - \frac{t_{ij}}{r_{ij}}\right) n_{ij}^{\alpha} n_{ij}^{\beta} - \frac{t_{ij}}{r_{ij}}\delta_{\alpha\beta} & i \neq j \\ \sum_{k\neq i}\left(c_{ik} - \frac{t_{ik}}{r_{ik}}\right) n_{ik}^{\alpha} n_{ik}^{\beta} + \frac{t_{ik}}{r_{ik}}\delta_{\alpha\beta} & i = j \end{cases}$$

where $H_{ij}^{\alpha\beta} = \frac{\partial V}{\partial R_i^{\alpha}\partial R_j^{\beta}}|_{\{\vec{R}_i\}}$.

The low frequency behavior of $D(\omega)$ have been subjected to many studies [14, 15, 16, 17]. As seen from Fig. 1.3, $D(\omega)$ shows a plateau upto a certain characteristic frequency ω^* below which $D(\omega)$ deviates from the plateau. Through the speed of sound, this characteristic frequency is related to a characteristic length scale in the system [14, 15]. ω^* also shows a scaling

$$\omega^* \sim \delta Z \sim \Delta\phi^{\frac{1}{2}} \tag{1.9}$$

Different length scales which diverge at the jamming transition have been identified [12]. This along with the various scaling discussed makes a compelling case that the jamming transition could be second order phase transition.

Forces and gaps

Another important feature of the jamming transition is related to the structure of the packing and the force network associated with it. For a soft-sphere system, two particles in contact exert a repulsive force on each other f and we can compute the distribution of these inter-particle forces. Near the jamming transition, small inter-particle forces are distributed by a power law with exponent θ [10]

$$P(f) \sim f^{\theta}.$$

For reasons that will be clear soon, we will not discuss the exact values of this exponent here.

The behavior of the pair correlation function of the jammed packings has been extensively analyzed [8, 9, 10]. The distribution gaps h diverges as

$$P(h) \sim h^{-\gamma}.$$

The exponent γ was thought to have a value of $\frac{1}{2}$ as shown in the earlier studies [8, 9, 18, 19], however excluding the rattlers from the calculation leads to a lower value of $\gamma \approx 0.4$ [20, 21, 22]. This will be important for the discussion going forward. This divergence near the jamming transition implies the existence of a large number of near contacts in the system.

Wyart [23] and Lerner *et al* [22] studied the stability of isostatic jammed packing of hard-spheres against compression and showed that the exponents γ and θ are constrained by an inequality. We will look into this result in detail.

1.4 Stability of jammed packing of hard-spheres

The following discussion is based on the two very interesting papers by Wyart [23] and Lerner *et al* [22]. Consider a packing of N hard-spheres in a bounding box whose walls apply a pressure p on the spheres touching the wall. How do we analyze the stability of such a system? Naturally, we can ask what a perturbation does to the system. If some low energy excitation can take the system to a denser packing at the same pressure, then we can call this system unstable against such perturbation. If there exists no such excitation that can reduce the volume of the system then we can consider the system to be stable. Given that we know jammed packings are stable (they can sustain pressure), we will show that the absence of such excitation implies a certain inequality between the force and gap exponents. As described before small inter-particle forces in the system are distributed according to a power-law. Opening of contacts carrying these small forces (by application of a dipole force along the contact) can be considered a low energy excitation.

Before we get into how such stability is analyzed, we should go through the following ideas as they are to be encountered at different places in the rest of the thesis.

A closer look at isostaticity

We had defined isostaticity as the condition where the number of degrees of freedom is exactly matched by the number of constraints in the system. Here we will discuss some subtleties related to the isostaticity condition. This section follows the discussion presented in the supplemental materials of [24].

A given jammed soft-sphere packing is under force-balance, that is the total force acting on each particle is zero. Let us denote the number of particles in the system as N and they have N_c contacts between them. For a system of soft-spheres a contact is defined as an overlap such that the potential energy due to the overlap is non-zero. Therefore the two particles in contact exert a force against each other. For a given pair of particles i, j we denote the force between them as $\vec{f}_{ij}$.

This force is along $\hat{n}_{ij}$, the unit vector connecting the two centers of the particles in contact. For a given particle i, let us denote $z(i)$ as the number of contacts that the particle has. Let us denote the external forces acting on particle i to be $\vec{F}_i^{ext}$ and $\vec{\boldsymbol{F}}$ is a $DN \times 1$ matrix representing the external forces acting on all the particles. Let us denote $\alpha = 1 \dots D$ to be the dimensions. Therefore for the particle i to be in force-balance we have the following condition.

$$F_{i\alpha}^{ext} = \sum_{j=1}^{z(i)} n_{ji}^{\alpha} |\vec{f}_{ji}| \tag{1.10}$$

This can be expressed as

$$\vec{\boldsymbol{F}} = \boldsymbol{\mathcal{S}}^T . \vec{\boldsymbol{f}} \tag{1.11}$$

where $\vec{\boldsymbol{f}} = \{f_1, \dots, f_{N_c}\}$. This tells us that the in the absence of external forces the zero modes of $\boldsymbol{\mathcal{S}}^T$ are the force-balance solutions. The dimensions of $\boldsymbol{\mathcal{S}}^T$ is $dN \times N_c$. n_{ij}^{α} is anti-symmetric with respect to interchanging i and j while $|\vec{f}_{ij}|$ is symmetric. Hence we have $\sum_i F_{i\alpha} = \sum_i \sum_j n_{ij}^{\alpha} |\vec{f}_{ij}| = 0$. This means that D equations in the system (for each α) are not independent. If all N_c variables are independent, for $N_c \geq (N-1)D$ we can have solutions for this equation. In this thesis, since we deal with periodic boundary conditions, external forces are set to zero. Hence $\vec{\boldsymbol{F}} = 0$ and Eq. 1.11 represents a set of homogeneous equations. For $N_c = (N-1)D$ the only solution is the trivial solution. This does not represent a jammed state as forces will be zero between the particles. For a jammed state to exist $N_c > (N-1)D$. Each such solution is called a "self-stressed" state. A system with $N_c = (N-1)D + 1$ contacts has only one self-stressed state and for soft-spheres this is the configuration that is at the jamming transition. This is the definition of isostaticity we will use in numerical simulations. This is important to study the criticality of jamming transition [24].

Similarly, we can relate the displacements to each particle i, $\vec{\delta r}_i$ to the changes in distances between the particles. Consider $\delta\rho_{ij}$ be the change is the distance between the pair ij, then

$$\delta\rho_{ij} = \sum_{\alpha} n_{ij}^{\alpha} (\delta r_{j\alpha} - \delta r_{i\alpha})$$

upto first order.

$$\boldsymbol{\delta\vec{\rho}} = \boldsymbol{\mathcal{S}} . \boldsymbol{\delta\vec{r}} \tag{1.12}$$

If we have a set of displacements such that $0 = \boldsymbol{\mathcal{S}} . \boldsymbol{\delta\vec{r}}$ then that is a set of displacements such that the distances between any pairs do not change. This is a floppy mode as this is a set of displacements such that the energy of the system stays the same. The matrix $\boldsymbol{\mathcal{S}}$ is $N_c \times DN$. Given that there are D trivial floppy modes due to the translational invariance in the system, it can be shown that for $N_c \geq (N-1)D$ there cannot be any non-trivial zero modes for this equation. The matrix $\boldsymbol{\mathcal{S}}$ is related to the Hessian $\boldsymbol{\mathcal{H}}$ of the system by [24]

$$\boldsymbol{\mathcal{S}}^T \boldsymbol{\mathcal{S}} = \boldsymbol{\mathcal{H}}.$$

Opening a contact

Let us consider that we open a given contact ij such that we do not change the distances between any other pairs. Consider $\boldsymbol{\delta\vec{r}}$ be the set of displacements that open just the contact ij. We can denote this by

$$\boldsymbol{\delta\vec{\rho}^{\{ij\}}} = \boldsymbol{\mathcal{S}}.\boldsymbol{\delta\vec{r}^{\{ij\}}} \tag{1.13}$$

where $\delta\rho_k^{\{ij\}} = \delta_{k\{ij\}}s$ where k indexes the contacts. The question we are asking is how to find the $\boldsymbol{\delta\vec{r}^{\{ij\}}}$, if such a solution exists. The dimensions of $\boldsymbol{S}$ is $N_c \times ND$. Therefore Eq. 1.13 is a set of inhomogenous equations. For any response, we are not interested in the trivial set of displacements: global translations. Therefore we also require that $\sum_{k=1}^{N} \boldsymbol{\delta\vec{r}_k} = 0$. These introduce D relations among the variables and therefore there are $N_c + D$ constraints and ND variables. For a set of in-homogenous equations there exists an unique solution if $N_c = (N-1)D$. However in our case, in the absence of external forces and in the presence of PBC, a configuration with a single self-stressed state will have $N_c = (N-1)D + 1$ constraints. Therefore Eq. 1.13 does not have a solution in this case. Instead let us multiply Eq. 1.13 with $\boldsymbol{S}^T$. From Eq. 1.13 we get

$$\begin{aligned}\boldsymbol{\mathcal{S}}^T\boldsymbol{\delta\vec{\rho}^{\{ij\}}} &= \boldsymbol{\mathcal{S}}^T\boldsymbol{\mathcal{S}}.\boldsymbol{\delta\vec{r}^{\{ij\}}} \\ &= \boldsymbol{\mathcal{H}}.\boldsymbol{\delta\vec{r}^{\{ij\}}}\end{aligned} \tag{1.14}$$

We can invert $\boldsymbol{\mathcal{H}}$ by restricting ourselves to the space orthogonal to the zero modes of $\boldsymbol{\mathcal{H}}$.

$$\boldsymbol{\delta\vec{r}^{\{ij\}}} = \boldsymbol{\mathcal{H}}^{-1}\boldsymbol{\mathcal{S}}^T\boldsymbol{\delta\vec{\rho}^{\{ij\}}} \tag{1.15}$$

We can consider $\boldsymbol{\mathcal{S}}^T\boldsymbol{\delta\vec{\rho}^{\{ij\}}}$ to be an application of a force-dipole on the pair $\{ij\}$.

$$\boldsymbol{\mathcal{S}}^T\boldsymbol{\delta\vec{\rho}^{\{ij\}}} = \boldsymbol{\vec{F}^{\{ij\}}_{dipole}}$$

and

$$\boldsymbol{\vec{F}^{\{ij\}}_{dipole}} = \boldsymbol{\mathcal{H}}.\boldsymbol{\delta\vec{r}^{\{ij\}}} \tag{1.16}$$

If we can solve Eq. 1.16 for a given force dipole we can calculate the response to the force dipole.

Stability of hard-sphere systems against compression

As mentioned before, we will analyze the stability of a hard-sphere system held at a pressure against rearrangements due to any low energy perturbation. In a soft-sphere system, we can compute the response of the system due to a perturbation applied as external force using Eq. 1.16. Let us assume that we can compute the response for a hard-sphere system.

Now we will concentrate on a hard-sphere system at the iso-static point. This system is contained in a cubic box of volume V made of rigid walls. We study N frictionless hard-spheres of diameter σ_0. The packing is formed by pushing particles together to maintain a pressure p. The pressure is imposed by the forces exerted on the particles at the boundary of the wall. In this iso-static system, removal of a contact will result in the generation of one floppy mode. Let us consider a pair of particles in contact $\langle 12\rangle$. If we push apart this pair of particles by a distance s, where s is small enough that this does not lead to the creation of a new contact in the system, then we have a floppy mode in the system. We can denote displacement of particle i due this floppy mode by $\delta\vec{R}_i^{\langle 12\rangle}(s)$. (If we imagine that we are physically pushing two particles apart by a distance of s, then due to the other contacts these particles have with the rest of the system we would get a set of displacements for all the particles in the system, this could be extensive in system size or not. When we push two particles apart we are applying an external perturbation to the system like the force in Eq. 1.16; the floppy mode is the response of the system to the perturbation we have applied). We would like to ask the question of what would happen to the system when it flows along this floppy mode.

By the definition, the floppy modes do not create overlaps among the particles. Therefore the displacements $\{\delta\vec{R}_i\}$ will obey the following condition that the separation between any particle pair other than $\langle 12\rangle$ will be unaffected while the separation between $\langle 12\rangle$ by definition is s.

$$\delta\vec{R}_{ij}^{\langle 12\rangle}(s).\vec{n}_{ij} + \frac{\left(\delta\vec{R}_{ij}^{\langle 12\rangle}(s).\vec{n}_{ij}^{\perp}\right)^2}{2r_{ij}} + \mathcal{O}(\delta R^3) = s\delta_{\langle 12\rangle\langle ij\rangle}. \tag{1.17}$$

We need to calculate the change in a vector of length r_{ij} which lies along $\vec{n}_{ij}$ when $\delta\vec{R}_{ij}^{\langle 12\rangle}(s)$ is added to it where $\delta\vec{R}_{ij}^{\langle 12\rangle}(s) = \vec{R}_i^{\langle 12\rangle}(s) - \vec{R}_j^{\langle 12\rangle}(s)$. Splitting $\delta\vec{R}_{ij}^{\langle 12\rangle}(s)$ along $\vec{n}_{ij}$ and $\vec{n}_{ij}^{\perp}$ we can see that the new length would be from Pythagoras's theorem. The expression

$$\delta\vec{R}_{ij}^{\langle 12\rangle}(s).\vec{n}_{ij} + \frac{\left(\delta\vec{R}_{ij}^{\langle 12\rangle}(s).\vec{n}_{ij}^{\perp}\right)^2}{2r_{ij}} \tag{1.18}$$

is the change in the separation between two particles $\langle ij\rangle$. Eq. 1.17 is straightforward for when $\langle ij\rangle = \langle 12\rangle$ and this displacement is zero if the pair is not $\langle 12\rangle$.

Now we write the force-balance condition for the jammed system. For the configuration at isostaticity where there are no zero modes in the system and each particle is individually under force balance. This condition can be written as

$$\vec{F}_i + \sum_{j(i)} f_{ij}\vec{n}_{ij} = 0; \forall i \tag{1.19}$$

where the sum $j(i)$ is over all particles j in contact with i and $\vec{F}_i$ are the external forces acting on particles at the boundary. Multiplying a displacement field $\delta\vec{R}_i$ with Eq. 1.10 and summing over all particles we arrive at

$$\sum_{i=0}^{N} \vec{F}_i.\delta\vec{R}_i + \sum_{\langle ij\rangle} \delta\vec{R}_{ij}.\vec{n}_{ij} f_{ij} = 0 \tag{1.20}$$

We start with Eq. 1.17 for floppy modes and keeping terms up-to $\mathcal{O}(s^2)$ and applying the displacements obeying Eq. 1.17 onto the force-balance condition Eq. 1.20 we get

$$p\delta V^{\langle 12\rangle} = sf_{\langle 12\rangle} - \sum_{\langle ij\rangle\neq\langle 12\rangle} \frac{\left(\delta\vec{R}_{ij}^{\langle 12\rangle}(s).\vec{n}_{ij}^{\perp}\right)^2 f_{ij}}{2r_{ij}} + \mathcal{O}(s^3) \tag{1.21}$$

where $\sum_{i=0}^{N}\vec{F}_i.\delta\vec{R}_i^{\langle 12\rangle}(s)$ will be the work done by the external forces applied by the wall at the boundaries and is equal to $-p\delta V^{\langle 12\rangle}$. Introducing a dimensionless number

$$c_{\langle 12\rangle} = \lim_{s\to 0}\frac{\sum_{\langle ij\rangle\neq\langle 12\rangle}\frac{\left(\delta\vec{R}_{ij}^{\langle 12\rangle}(s).\vec{n}_{ij}^{\perp}\right)^2 f_{ij}}{2r_{ij}}}{\frac{N\langle f\rangle s^2}{\sigma_0}} = \frac{\sum_{\langle ij\rangle\neq\langle 12\rangle}\frac{\left(\vec{V}_{ij}^{\langle 12\rangle}.\vec{n}_{ij}^{\perp}\right)^2 f_{ij}}{2r_{ij}}}{\frac{N\langle f\rangle}{\sigma_0}} > 0 \tag{1.22}$$

where

$$\vec{V}_{ij}^{\langle 12\rangle} = \frac{d\delta\vec{R}_{ij}^{\langle 12\rangle}(s)}{ds}|_{s=0}$$

Using $c_{\langle 12\rangle}$ in Eq. 1.21 we get

$$p\delta V^{\langle 12\rangle} = sf_{\langle 12\rangle} - \frac{s^2\langle f\rangle Nc_{\langle 12\rangle}}{2\sigma_0} + \mathcal{O}(s^3) \tag{1.23}$$

where $\langle f\rangle$ is the average force and σ_0 is the diameter of the hard-spheres. Now we can see that small s the volume of the system always increases because $f_{\langle 12\rangle} > 0$. However, for larger s the second term becomes important and the system can flow along the floppy mode to create a denser packing as shown in Fig. 1.4. The second term is due to the component of the deformation vector orthogonal to the bond. Therefore this term corresponds to the buckling of the bonds due to the displacements imposed. The buckling of bonds can result in a reduction of the volume of the system. We can calculate this distance beyond which the system volume reduces as

$$s^* = \frac{f_{\langle 12\rangle}\sigma_0}{c_{\langle 12\rangle}\langle f\rangle N} \tag{1.24}$$

However, the system can only flow along the floppy mode till a new contact is formed, after which the system is iso-static and hence devoid of floppy modes. We denote by $s^\dagger$ the distance by which we can push $\langle 12\rangle$ till a new contact is formed. If $s^\dagger < s^*$ the the configuration is stable (w.r.t to this perturbation); no denser packing can be achieved by flowing along the floppy mode. Therefore we define the stability index for the contact $\langle 12\rangle$ as

$$k_{\langle 12\rangle} \equiv \frac{f_{\langle 12\rangle}\sigma_0}{s^\dagger c_{\langle 12\rangle}\langle f\rangle N} \tag{1.25}$$

if $k_{\langle 12\rangle} < 1$ then the packing is unstable against opening the contact $\langle 12\rangle$.

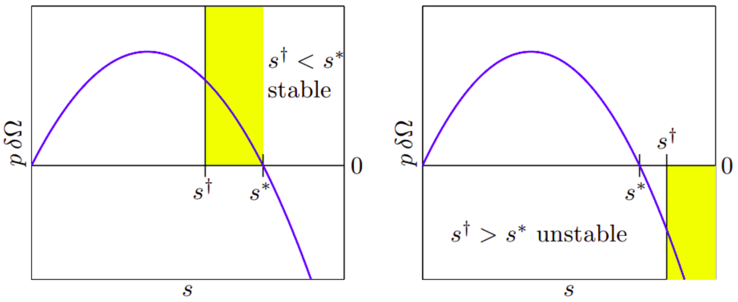

Figure 1.4: The figure corresponding to Eq. 1.23. If we can push the pairs beyond s^* then the system can flow along the floppy mode generated to create a denser packing. However if the system encounters a contact before s^*, further motion along the floppy mode is prohibited and hence the system is stable against going into denser packing. Image taken from [22] with permission.

From Eq. 1.24 we can see that the bond carrying the smallest force in the system will have the smallest s^* in the system. This is the bond that is closest to failing in the system. For the system to be stable against opening this bond, the smallest gap in the system $s^\dagger$ has to be smaller that s^*.

Suppose for a given packing we have N_c contacts in the system each of them carrying a force. If the smallest force is f_{min}, then the probability of picking a force smaller than $f_{min} + \epsilon$ where ϵ is a small quantity is $1/N_c \sim 1/N$ as there is only one force smaller than that value. This should be equal to $\int_0^{f_{min}} P(f)df$. Since $P(f) \sim f^\theta$, we have $f_{min} \sim N^{-\frac{1}{1+\theta}}$.

Similarly, we can estimate the smallest gap h_{min} in the system. If we increase the radii of all particles by h_{min} then the total number of contacts in the system will increase by 1. The average coordination number will be $2D + \frac{2}{N}$ as the system is isostatic. The average coordination number is $Z(h_{min}) = \int_0^{\sigma_0 + h_{min}} 4\pi s^2 g(s) ds$ in $D = 3$ where $g(s)$ is the radial-distribution function. The probability of finding a gap with the value h is $4\pi s^2 g(s) = P(h) = h^{-\gamma}$ where $s = \sigma + h$. Therefore $Z(h_{min}) \sim 2D + h_{min}^{1-\gamma}$. Equating this with $2D + \frac{2}{N}$ we get $h_{min} \sim N^{\frac{-1}{1-\gamma}}$ [25, 22]. From Eq. 1.25 we know that the $h_{min} \sim N^{\frac{-1}{1-\gamma}}$ has to be smaller than $s^* \sim \frac{f_{min}}{N} \sim N^{\frac{-(2+\theta)}{1+\theta}}$. This gives us the condition

$$\gamma \geq \frac{1}{2+\theta}. \tag{1.26}$$

Note that in deriving this we assumed that dimensionless number c_{ij} does not have a dependence of N. This is only true for contacts, which when opened result in a system-wide excitation. For contacts whose response to opening is localized this does not hold. The distribution of forces that correspond to localized response is characterized by an exponent θ_l and following a similar argument as above we get [22]

$$\gamma \geq \frac{1-\theta_l}{2}. \tag{1.27}$$

Numerical calculation of these exponents showed that these inequalities are in fact saturated for systems at the jamming point [24, 22, 26, 27]. Therefore jammed systems are at the threshold of stability - they are "marginally" stable.

Why are these exponents important? The exponents γ and θ are important because the mean-field theory of hard-sphere glasses and jamming has non-trivial predictions for these exponents - $\theta_e = 0.42311\ldots$ and $\gamma = 0.41269\ldots$ [28]. Note that then $\gamma = \frac{1}{2+\theta_e}$ which saturates stability criterion Eq. 1.26. Assuming that Eq. 1.26 and Eq. 1.27 are saturated in finite dimensions we get $\theta_l \approx 0.17$. A major success of the theory is that these exponents have been numerically measured for jamming in dimensions upto $D = 2$ [24, 26] for these exponents thereby suggesting that $D = 2$ is the upper critical dimension of the jamming transition. A discussion of the mean-field theory of hard-spheres is outside the scope of this thesis. Please refer to [29, 30, 31, 32, 33] and [28] for the details on the theory.

So far we had confined our discussions of jamming to simple numerical models for the ease of connecting with the theory glass and jamming transition. As we will see these are very useful in demonstrating many features observed in real granular materials. However, the interaction between real granular materials are frictional and plays an important role in various behavior observed. We will review the study of jamming frictional granular materials in the following sections.

1.5 Jamming with friction

The following discussion corresponds to modeling and experiments of dry granular materials. Unlike the jamming of frictionless sphere/disk packings, the contact force between particles is not necessarily along the line connecting the centers to the two particles. Frictional forces act along the tangential direction at the point of contact *i.e.* perpendicular to the normal component which acts along the vector connecting the particle centers. Therefore, in a static jammed configuration, the particles are in force balance as well as torque balance. The tangential frictional force is also constrained by the Coulomb threshold $|\vec{f_t}| < \mu|\vec{f_n}|$ where μ is the friction coefficient.

In the presence of friction the density and co-ordination number at which jamming occurs is generally smaller than the frictionless value and dependent on the protocol used to arrive at the state. The lowest packing fraction at which jamming can be observed is called random lose packing (RLP) which is reported to be around ≈ 0.55 [34].

The presence of additional constraints to force-balance conditions in the presence of friction leads to the generalization of the isostatic condition for jamming [11]. In addition to the force and torque balance condition the Coulomb condition also adds constraints to the system. Given N particles and N_c constraints, we ask if the contact network can have a solution of finite forces satisfying the above mentioned constraints. These include DN force-balance equations, $\frac{D(D-1)}{2}N$ torque balance equations. If the system has M contacts at the Coulomb threshold then there are $n_m N = M$ constraints as well. The number of free variables in this system of linear equations is

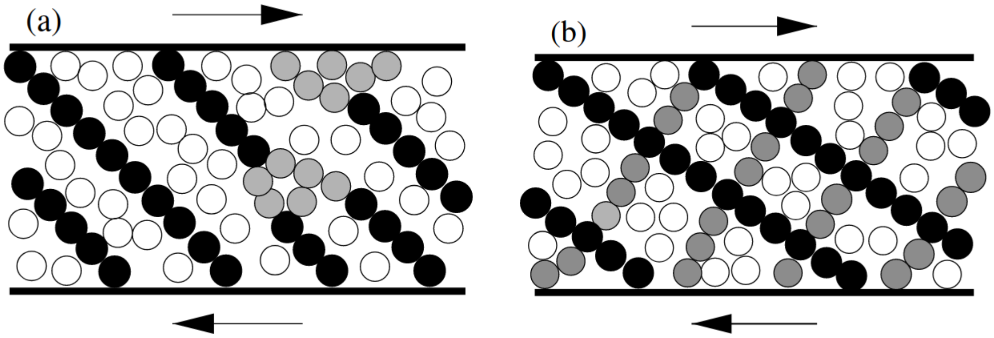

Figure 1.5: Schematic describing the shear jamming transition. Left figure shows the formation of force-chains in the compressive direction - fragile state. Right figure shows force-chains in the both compressive and dilative direction - shear jamming. Image taken from [41] with permission.

DN_c for the number force-vectors we have. This leads to the generalized isostaticity condition

$$Z_{\mu}^{iso} = D + 1 \tag{1.28}$$

where $Z_{\mu} = Z - \frac{2n_m}{D}$. For $\mu = \infty$ $n_m = 0$ and $Z_{iso}^{\mu} = D + 1$ while the frictionless limit cannot be obtained from this equation. For gently prepared samples this equation predicts the jamming very well [11, 35].

Once the jamming density and the isostatic value for the corresponding μ is identified, the pressure and excess contact number scales in a similarly to frictionless particles [34, 36] with the pressure scaling with exponent ≈ 1 and excess contact number scaling with exponent ≈ 0.5.

1.6 Amorphous materials under shear

So far we have discussed the effect of compression on the jamming transition. In this section, we discuss how materials acquire rigidity when subjected to shear deformation. Shear jamming was initially experimentally observed in dry granular materials [37] and later in colloidal suspensions [38]. Dry granular materials under shear develop rigidity and undergo a jamming transition at a certain strain. Note that these discussions are about the behavior of unjammed material when subjected to shear. This is different from what happens to materials that are jammed when subjected to shear (see [39, 40]).

1.6.1 Shear Jamming

Shear jamming with friction

Jamming due to shear was first proposed by Cates *et al* [41]. In this work the authors hypothesized the following picture. Imagine a system of granular materials subjected to simple shear (simple

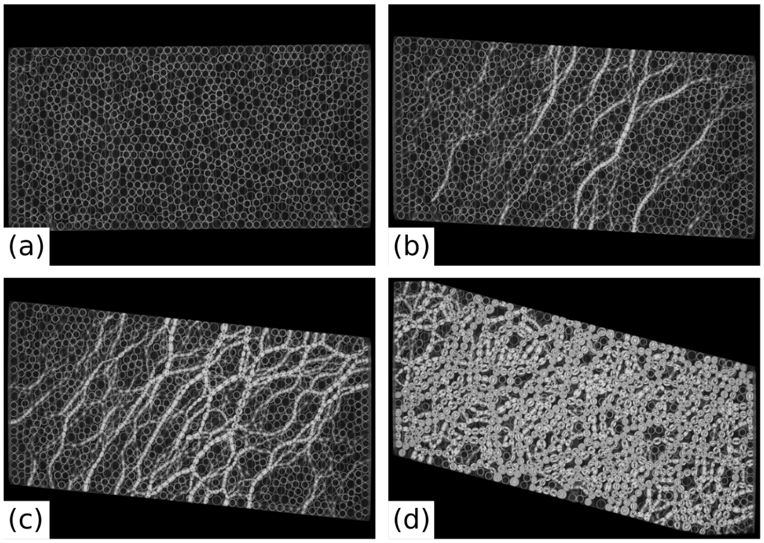

Figure 1.6: Snapshots from an experiment where simple shear is applied to photoelastic disk packing. **(a)** The unjammed initial configuration has no force network **(b)** as the material is sheared force network develops along the compressive direction **(c)** this force network gets stronger **(d)** eventually the system is jammed. Image taken from [42].

shear is a deformation in which parallel planes in a material remain parallel and maintain a constant distance while translating relative to each other). In simple shear, we can define two directions - a compressive and a dilative one, where the compressive direction is the diagonal along which particles are pushed towards each other, and the other diagonal is the dilative one. When particles along the compressive direction are pushed towards each other they exert forces on each other and a force network will be formed along the compressive direction. This force network can resist shear in one direction, it is like a pillar along the compressive direction. However when the system is strained further this "pillar" is compressed and it will buckle. When this happens, it will create force networks, or "pillar" like structures along the dilative diagonal, and then the system is truly jammed, resisting deformation along both directions. This scenario is shown schematically in Fig. 1.5. Configurations of granular materials generated during shear which can resist shear along one direction but not in the other are called fragile. Notice that friction is essential for configurations to exist in a fragile state. In the absence of friction, the force network along the compressive direction will not be able to resist shear in fragile matter. Note that shear can be applied in other ways too - for example, one can consider pure shear instead of simple shear where a square is deformed into a rectangle. In either case, one can identify a compressive and a dilative direction.

The shear-driven jamming in granular materials was first observed by Bi *et al* [37] in experiments with photoelastic disks. One can extract the force network of a disk packing in this system [43]. In these experiments, disk packings are in a stress-free state below the isotropic jamming point ϕ_J. These disk packings above a certain density $\phi_S < \phi_J$ develop force-network and undergo jamming when strain γ is increased. The fragile and shear jammed states were identified by the percolation of the strong force network. Strong forces were identified as forces that are larger than the average force. Disk packings in which the strong force-network percolates along only compressive direction were identified as fragile and those with a percolating force-network in both directions were identified as shear jammed. The fragile states only resist shear in the compressive direction while shear jammed state can resist in both directions. The shear jamming transition was associated with an increase in pressure P and stress σ with increasing strain γ. Ren *et al* [44] showed that the $P \sim \gamma^2$ for dry granular material and an interesting connection of shear jamming transition was made with dilatancy. Reynolds dilatancy [45], where a material expands in volume when subjected to shear when held at constant pressure is a conjugate phenomenon to shear jamming. If the material is held at constant volume during shear, then one observes shear jamming. Shear jamming is also observed in simulations of frictional sphere packings [46, 47].

Shear jamming in the absence of friction

The role of friction in the observation of shear jamming (and the conjugate phenomenon dilatancy) has been investigated through simulations. Despite dilatancy being originally proposed as a geometric phenomenon, numerical studies in frictionless systems showed an absence of dilatancy [48, 49]. Early studies on the shear jamming transition in frictionless systems were shown to happen in a range of densities below ϕ_J which vanishes in the thermodynamic limit [50, 51]. Vinutha *et al* [52] studied the structures formed during quasi static shear deformation of systems below ϕ_J and showed that these structures resemble jammed packings although they are only stable against deformation in the presence of friction.

However, these studies were conducted in a range of densities below $\phi_J \approx 0.64$ which is the minimum jamming density in the system. As mentioned earlier the jamming density is not unique and we can generate configurations that jam at higher density ϕ_j. Therefore there is a range of densities such that $\phi_J < \phi < \phi_j$ where one can find unjammed configurations. When these unjammed configurations are subjected to shear deformation, they undergo jamming [53, 54]. Unlike the shear jammed states observed in [50], these configurations exist in the thermodynamic limit.

1.7 Scope of the thesis

At this point, we can motivate the studies conducted on this thesis. The observation of *genuine* frictionless shear jammed states (those that exist in the thermodynamic limit) gives us the opportunity to study anisotropic jamming without the complication of friction. How does this help us? Since real-world granular materials have friction, we have to investigate how shear jamming in frictionless systems educate us in understanding frictional shear jamming. For example, does the relation between shear jamming and dilatancy hold for frictionless systems? Previous results [52, 55] have shown that sheared frictionless disks do capture many geometric features of sheared frictional disks. It is also important to understand the limitations of this analogy. In addition, we can compare shear and isotropic jamming in frictionless systems. The rigidity transition of the contact network in frictional and frictionless jamming has also received much attention recently [56, 57, 58, 59, 60]. The following questions arise in this regard,

1. Is dilatancy a geometric phenomenon as originally described?
2. How does the criticality of isotropic jamming compare with that of shear jamming?
3. What is the nature of rigidity transition in frictional and frictionless systems under shear?

These are a few directions we explore in this thesis. Following are the various chapters and their short description.

Chapter 2 explores the relationship between dilatancy and shear jamming in frictionless systems. We also investigate the steady state equation of state to understand the correspondence.

Chapter 3 compares the criticality of the shear jamming transition with isotropic jamming in frictionless systems. We check the marginal stability condition discussed in section 1.4 for configurations at the shear jamming transition. The interesting elastic properties of jamming as described in [50] are also investigated.

Chapter 4 studies the nature of the rigidity transition of the contact network associated with shear jamming in frictionless and frictional disk packings. We also compare our results with the previously studied rigidity transition.

Chapter 5 summarises the thesis and indicates some directions for future study.

Chapter 2

Shear Jamming and Dilatancy [1] [2]

---

[1] This work is done in collaboration with Dr. Deng Pan and Prof. Yuliang Jin at CAS Key Laboratory of Theoretical Physics, Institute of Theoretical Physics, Chinese Academy of Sciences, Beijing 100190, China and Prof. Bulbul Chakraborty at Martin Fisher School of Physics, Brandeis University, Waltham, MA 02454, USA. All simulations of the polydisperse system was done by Dr. Deng Pan and Prof. Yuliang Jin.

[2] The contents of this chapter has been published as ‘‘**Babu, Varghese, Deng Pan, Yuliang Jin, Bulbul Chakraborty, and Srikanth Sastry. "Dilatancy, shear jamming, and a generalized jamming phase diagram of frictionless sphere packings.**" Soft Matter 17, no. 11 (2021): 3121-3127.”

2.1 Introduction

As discussed in the previous chapter, granular packings display the remarkable phenomenon of *dilatancy*, wherein their volume increases upon shear deformation. Conventional wisdom and previous results suggest that dilatancy, as also the related phenomenon of shear-induced jamming, requires frictional interactions. In this chapter, we show that the existence of isotropic jamming densities ϕ_j above the minimal density (or the J-point density) ϕ_J, leads both to the emergence of shear-induced jamming and dilatancy in frictionless packings. Density- or stress-driven jamming is of central importance in comprehending a wide variety of complex rheological properties of granular matter, and forms an essential part of a broader understanding of the transition from flowing states of matter to non-flowing or structurally arrested states, including, *e. g.*, the glass transition.

Density-driven jamming, unjamming and yielding of frictionless hard and soft particles have been investigated extensively since the proposal of the jamming phase diagram [61], which has, as originally proposed, a unique density (packing fraction) at ϕ_J characterizing the jamming transition at zero temperature and shear stress. Since then it has been shown that the jamming density ϕ_j is protocol-dependent and therefore not unique [62, 63, 64, 65, 66, 5, 30, 6] satisfying in general $\phi_j \geq \phi_J$ [6]. However, critical behavior associated with jamming, for example the scaling relationship between pressure and density, remains the same, irrespective of ϕ_j [5].

An early proposal that shear deformation, besides density, can induce jamming [41], has recently been explored extensively in experimental and theoretical investigations [37, 44, 67, 68, 54, 52, 69, 70, 71, 72, 73, 74, 75, 76]. In shear jamming, the development of an anisotropic contact network under shear leads to the emergence of a state of finite shear stress and pressure, with their ratio peaking at a density-dependent characteristic strain [37, 44, 67, 68, 70, 71, 72].

The shear-strain dependent pressure was termed *Reynolds pressure* in [44], reflecting the idea that shear jamming occurs because constant volume conditions frustrate the tendency of granular materials to dilate under shear [45], a phenomenon widely referred to as *dilatancy.* Shear jamming and dilatancy in frictional granular matter have thus been viewed as two sides of the same coin.

Reynolds' dilatancy in granular materials has been extensively investigated, motivated by the relevance of the phenomena to soil mechanics [77, 78]. Many available results suggest an intimate relationship between frictional interactions and dilatancy: stress-dilatancy relations couple dilatancy and friction between particles [79]. Recent studies indicate that friction is important for observing shear jamming and dilatancy [80]. Numerical studies [50, 48, 49] have reported, and experiments [81] have also indirectly indicated, the absence of dilatancy in frictionless systems.

These observations are at variance with the simple picture suggested by Reynolds [45], where dilatancy arises purely from geometric exclusion effects of hard particles, which should therefore be observed also in frictionless systems. We demonstrate conditions under which dilatancy emerges naturally in frictionless sphere assemblies. We show that such conditions depend critically on the presence of a line of jamming points at densities ϕ_j above ϕ_J. These dense jamming points can be systematically obtained by using proper jamming protocols [6], and the distinction between ϕ_j and ϕ_J was shown to be robust in the limit of large system size [5].

In motivating our study, we note that, below ϕ_J, initially unjammed frictionless sphere assemblies develop structures under shear, with average geometric contact numbers that increase with density, which can be mechanically stabilized by friction [52]. If the unjammed configurations are at densities above ϕ_J, shear deformations may create contact networks that satisfy the isostatic jamming condition for frictionless packings which are mechanically stable, leading to the possibility of both shear jamming and dilatancy. Thus, the absence of dilatancy [48] and shear jamming [50] in earlier studies could be due to the failure to obtain unjammed initial configurations above ϕ_J rather than to the absence of friction. Mean-field theories, which are exact in large dimensions, indeed predicted the possibility of shear jamming [76] and shear dilatancy [82] in deeply annealed glasses of thermal hard spheres, where friction is absent. However, it is not clear if these two effects can be indeed disentangled from friction in realistic systems in physical dimensions.

In this chapter, we explicitly demonstrate the phenomena of shear jamming and dilatancy in two simulated frictionless granular models in three dimensions. Both effects emerge in systems with $\phi_j > \phi_J$, and vanish as $\phi_j \to \phi_J$, consistent with previous studies [50, 51, 48]. The *steady-states* in the large strain limit are governed by a universal equation of state (EOS), while the EOS for the initially isotropically jammed states at zero strain depends on the preparation protocol. This difference results in a discontinuous jump of the yield stress at ϕ_j for $\phi_j > \phi_J$, generalizing (in the athermal case) the Liu-Nagel jamming phase diagram [61].

2.2 Models and Methods

2.2.1 Models

The two models represent systems that consist of $N = 2000$ (unless otherwise specified) bi-disperse (BD) and poly-disperse (PD) spheres. The bi-disperse system consists of N equal-mass spheres with a diameter ratio $D_1/D_2 = 1.4$ and a number ratio $N_1/N_2 = 1$. The PD system contains N equal-mass spheres whose diameter distribution is characterized by $P(D) \sim D^{-3}$, for $D_{\min} \leq D \leq D_{\min}/0.45$. In both the BD and the PD models, the particles interact via a purely-repulsive, harmonic potential, $v_{ij}(r) = \frac{1}{2}(1 - r/D_{ij})^2$ (zero if $r > D_{ij}$), where r is the inter-particle distance and $D_{ij} = (D_i + D_j)/2$, is the just-touching distance between particles i and j. The volume fraction is $\phi = \rho(1/6)\pi\overline{D^3}$, where ρ is the number density N/V, and V is the volume of simulation box.

2.2.2 Simulation Details

Constant volume athermal quasi-static shear

(i) In the BD model, constant volume athermal quasistatic shear (AQS) simulations are carried out using LAMMPS[83]. To simulate a uniform simple shear deformation, at each step an affine transformation is applied to the position of each particle, $x' = x + \delta\gamma \times z, y' = y, z' = z$, where $\delta\gamma = 10^{-4}$, followed by energy minimization using the conjugate gradient (CG) method. The CG procedure stops when the maximum component of the force vector is less than 10^{-16}. The energy minimization stops when the maximum distance moved by any particle is less than the machine precision during an iteration. The norm of the equilibrium net force vector is of the order of 10^{-13} and the maximum component is of the order of 10^{-14} at the termination of minimization.

(ii) In the PD model, the affine transformation is applied with the same step size $\delta\gamma = 10^{-4}$, followed by energy minimization using the FIRE algorithm [84]. The minimization procedure stops when the percentage of force balanced particles with net force magnitude $|f| \leq 10^{-14}$ reaches 99.5%.

Constant pressure athermal quasistatic shear

In constant pressure AQS simulations, the energy minimization is replaced by the minimization of enthalpy $H = U + PV$ at the imposed pressure P. (i) In the BD model, the minimization stops when the maximum distance moved by any particle during a minimization step is less than the machine precision. (ii) In the PD model, the minimization stops if the percentage of force balanced particles reaches 99.5%, and the deviation from the target pressure is less than 10^{-4}.

Protocols to prepare initial configurations

(i) Mechanical annealing by cyclic AQS for the BD model. We first use the method in [5] to generate packings with jamming density $\phi_J \approx 0.648$. The initial configurations are hard-sphere (HS) configurations at a packing fraction of $\phi = 0.363$, which are equilibrated using the Monte-Carlo (MC) algorithm. We switch to the harmonic soft-sphere potential, rapidly compress the configurations by rescaling the volume of the simulation box (till $\beta P/\rho$ decays to ~ 1000, where β is the inverse temperature), and remove the resulting overlaps by using MC simulations. The temperature is then switched off, and the system is further quasistatically compressed, by inflating the particles uniformly, followed by energy minimization using the CG method. The compression stops when the energy per particle $e = E/N$, after minimization, remains above 10^{-16}. This is used as the criterion for jamming. Then the system is slowly decompressed till $e < 10^{-16}$, which generates configurations corresponding to jamming density $\phi_J \approx 0.648$.

We then use mechanical annealing to increase the jamming density from ϕ_J to $\phi_j > \phi_J$. The configurations obtained from the above procedure are compressed to various over-jamming densities $\phi > \phi_J$, and are unjammed using cyclic AQS, $\gamma = 0 \to \gamma_{max} \to 0 \to -\gamma_{max} \to 0$, where the strain amplitude $\gamma_{max} = 0.07$ [53], and the strain step $\delta\gamma = 10^{-3}$. These configurations correspond to jamming densities $\phi_j > \phi_J$. (ii) Thermal annealing by a swap algorithm for the PD model. We first prepare dense equilibrium HS configurations at ϕ_g, using the the swap algorithm [85]. At each swap MC step, we exchange the positions of two randomly picked particles as long as they do not overlap with other particles. Combined with standard event-driven molecular dynamics (MD), such non-local swap moves significantly speed up the equilibration procedure. The poly-dispersity of the model suppresses crystallization even in deep annealing, and optimizes the efficiency of the algorithm [85].

For each equilibrium configuration at ϕ_g, we then perform a rapid quench to generate the jammed configuration at ϕ_j (see Ref. [86] for the relationship between ϕ_g and ϕ_j). In particular, the J-point state at $\phi_J \simeq 0.655$ are quenched from random initial configurations with $\phi_g = 0$ [8]. The rapid quench is realized by inflating the particle sizes instantaneously to reach the target density, switching to the harmonic soft-sphere potential, and then minimizing the total potential energy using the FIRE algorithm [84]. The same jamming criterion is used as in the BD model.

Jamming densities of mechanically annealed bi-disperse sphere packings

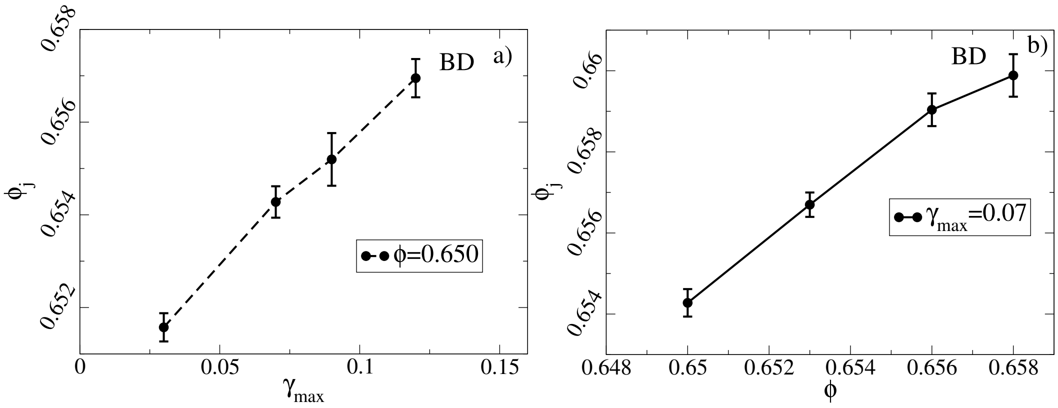

Figure 2.1: **Dependence of jamming density ϕ_j on protocol parameters of cyclic AQS, for the BD model.** **a)** Dependence of jamming density ϕ_j on the strain amplitude γ_{max}, for a fixed unjamming density $\phi = 0.650$. **b)** Dependence of jamming density ϕ_j on the unjamming density ϕ, for a fixed $\gamma_{max} = 0.07$. Error bars represent standard deviations.

An over-jammed BD system at packing density ϕ (compressed from $\phi_J \simeq 0.648$), unjams under constant volume cyclic AQS, and jams again at ϕ_j ($\phi_j > \phi > \phi_J$) upon a further compression. The jamming density ϕ_j depends on both the unjamming density ϕ and the strain amplitude γ_{max} of the cyclic shear. As shown in the FIG 2.1, ϕ_j increases with γ_{max} for a fixed ϕ, and increases with ϕ for a fixed γ_{max}. In the main text, we use $\gamma_{max} = 0.07$, because for this amplitude, the largest range of densities over which unjamming occurs is obtained [53].

Calculation of the stress tensor and the pressure

The stress tensor is calculated using the formula,

$$\hat{\sigma} = -\frac{1}{V} \sum_{i<j} \vec{f}_{ij} \otimes \vec{r}_{ij}, \tag{2.1}$$

where $\vec{f}_{ij}$ and $\vec{r}_{ij}$ are the inter-particle force and distance vectors between particles i and j. The pressure P is related to the trace of the stress tensor, $P = -(\sigma_{xx} + \sigma_{yy} + \sigma_{zz})/3$, which can be written as,

$$P = \frac{1}{3V} \sum_{i<j} \vec{f}_{ij} \cdot \vec{r}_{ij}. \tag{2.2}$$

We clarify that the observations here under quasistatic shear do not always apply when shear rates are finite.

2.3 Results and Discussions

2.3.1 Shear Jamming

We first show that an unjammed configuration at $\phi < \phi_j$, where $\phi_j > \phi_J$, can be jammed at a certain strain γ_j by uniform constant volume AQS. The onset of shear jamming is characterised consistently by a steep increase of the shear stress σ_{xz} (Fig. 2.2(a) and (b)), of the non-rattler contact number Z_{NR} (Fig. 2.2(c)), of the pressure around γ_j. We observe that Z_{NR} exceeds the isostatic value $Z_{iso} = 2D = 6$, where $D = 3$ is the spatial dimensionality, for $\gamma > \gamma_j$, indicating that the shear jammed systems are mechanically stable. The non-rattler contact number Z_{NR} jumps discontinuously at γ_j (Fig. 2.2(c)), associated with an abrupt increase of the potential energy PE (Fig. 2.2(d)). The value of γ_j, as well as the stress overshoot amplitude, depends on the distance to the isotropic jamming $\Delta\phi = \phi_j - \phi$, and the value of ϕ_j that characterizes the degree of mechanical/thermal annealing in the initial preparation procedure (Fig. 2.2 (b)). The data of $PE(Z_{NR})$, on the other hand, follow a universal function on the jamming side $Z_{NR} > Z_{iso}$, that is independent of the jamming strain γ_j, the model, and the jamming protocol (shear or compression), see (Fig. 2.2(d)). The data for $\phi_j \approx \phi_J$ in Fig. 1(b) also offers a clear visual demonstration (to be more precisely shown later) that shear jamming disappears in the limit $\phi_j \to \phi_J$

Additionally, Fig. 2.3 shows how the pressure P and the potential energy PE increase with strain. In the mechanical annealing protocol, the shear jamming strain γ_j, which is indicated by an abrupt jump of the pressure P in Fig. 2.4, is always greater than $\gamma_{max} = 0.07$, the training amplitude used in the cyclic shearing.

We also calculate the macroscopic friction $\mu = \sigma_{xz}/P$ of the configurations as a function of $\gamma - \gamma_j$ (Fig. 2.5), which shows a peak in the cases when there is a significant overshoot in the stress-strain curve (Fig. 2.2). This peak, appearing after the shear jamming strain γ_j, also exists in the uniform shear of over-compressed systems (Fig. 2.6). In both cases, the peak occurs near the yielding point.

2.3.2 Dilatancy

We next show that packings with $\phi_j > \phi_J$ dilate under constant pressure AQS. For this purpose, we modify the original AQS protocol, which is based on energy minimization at constant volume, to minimize instead the enthalpy, allowing changes in the volume of the simulation box to ensure a fixed pressure. In this constant pressure AQS protocol, the system traverses only those potential energy minima that have the specified pressure, P. Since the pressure is finite, the system is jammed throughout this process. For both BD and PD models, during the constant pressure shear deformation the system dilates until reaching a steady-state at packing fraction ϕ_s that depends on the pressure applied (Fig. 2.7). Correspondingly, the stress σ_{xz} increases initially with strain, and eventually also reaches a steady-state plateau after an overshoot (Fig. 2.7(b) and 2.7(d)). The

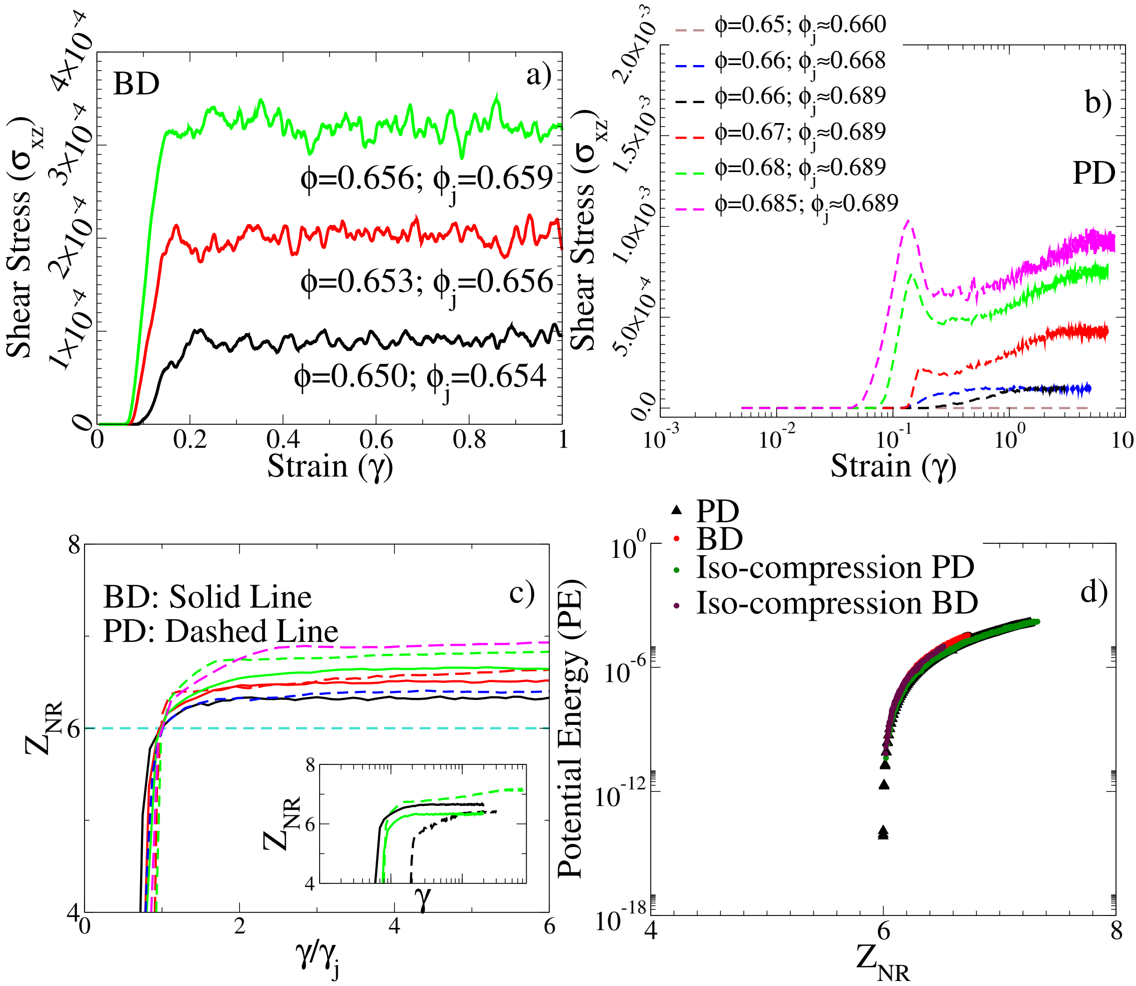

Figure 2.2: **Shear jamming.** Shear stress σ_{xz} as a function of strain γ for (a) BD model, (b) PD model, and a few different ϕ_j and ϕ. (c) Non-rattler contact number Z_{NR}, which is calculated after removing rattlers (particles with less than $D+1$ contacts) recursively, as a function of γ/γ_j. Inset shows unscaled data, configurations at different densities jam at different strains. (d) The potential energy PE is a universal function of Z_{NR} above jamming, for both BD and PD systems, for different ϕ_j and ϕ (and therefore different γ_j), and for both compression and shear jamming. The data are averaged over 20 and 64 independent samples in BD and PD systems respectively.

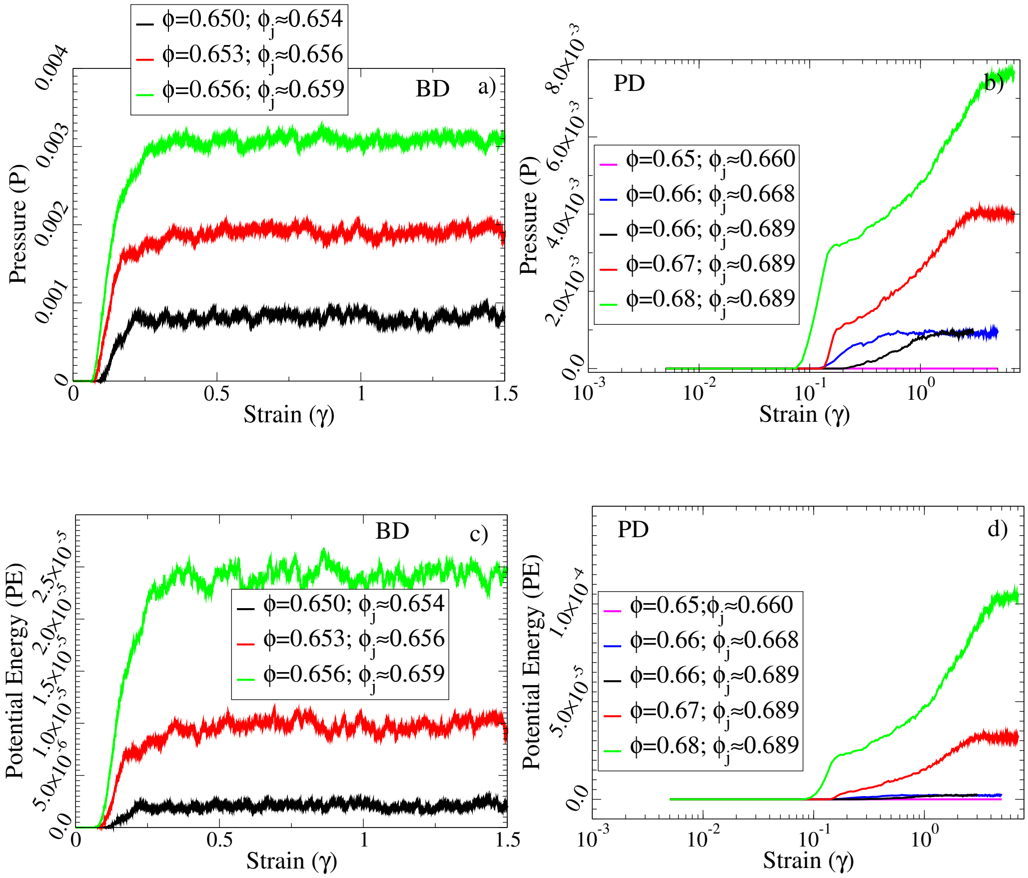

Figure 2.3: **Evolutions of a-b) pressure P and c-d) potential energy PE with strain γ during shear jamming.** The constant volume uniform AQS is applied. Data are presented for a few different ϕ and ϕ_j, obtained in both BD and PD systems.

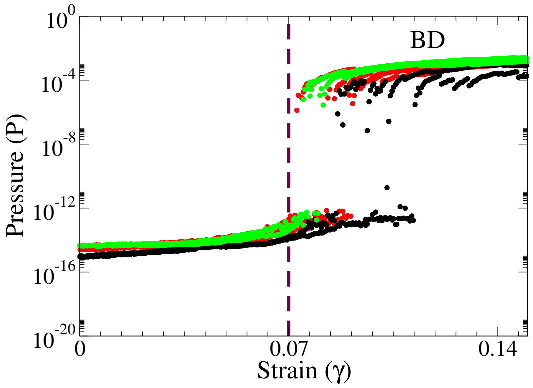

Figure 2.4: **Shear jamming under uniform shear in mechanically annealed BD systems.** The pressure increases abruptly as the system is strained beyond $\gamma = \gamma_{max}$, indicating shear jamming. We present multiple realizations for each ϕ_j, where $\phi_j = 0.659$ (green), 0.656 (red), and 0.654 (black). The densities at which shear is carried out are $\phi = 0.656$ (green), 0.653 (red), and 0.650 (black).

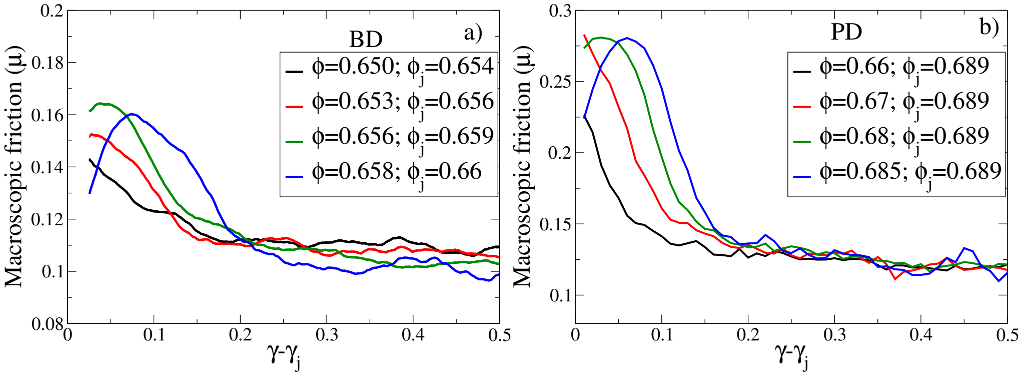

Figure 2.5: **Macroscopic friction μ as a function of distance from jamming strain $\gamma - \gamma_j$ for a) BD and b) PD systems.** The jamming strain γ_j is identified as the strain at which σ_{xz} increases above 10^{-11} in BD systems, and above 10^{-8} in PD systems.

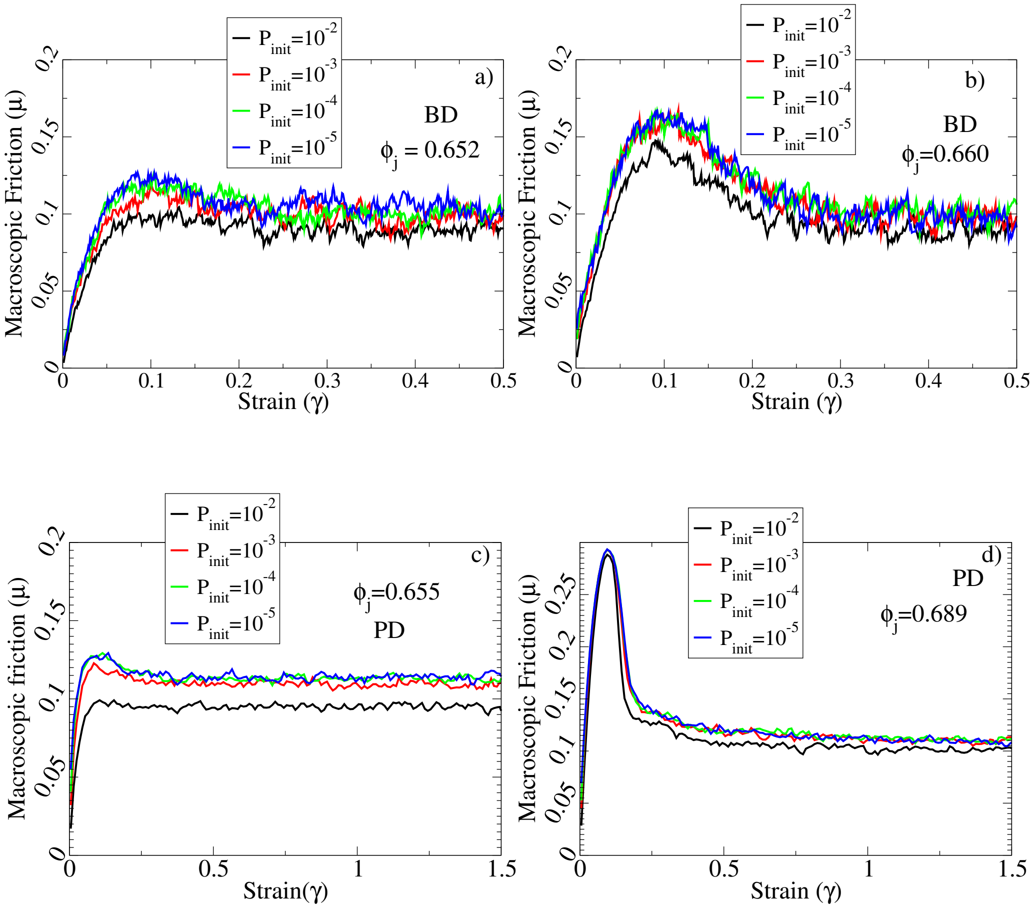

Figure 2.6: **Microscopic friction μ of over-compressed systems ($P_{init} > 0$, $\phi > \phi_j$) as a function of strain γ under constant volume shear.** Data are plotted for two different ϕ_j and four different P_{init} in both BD and PD models.

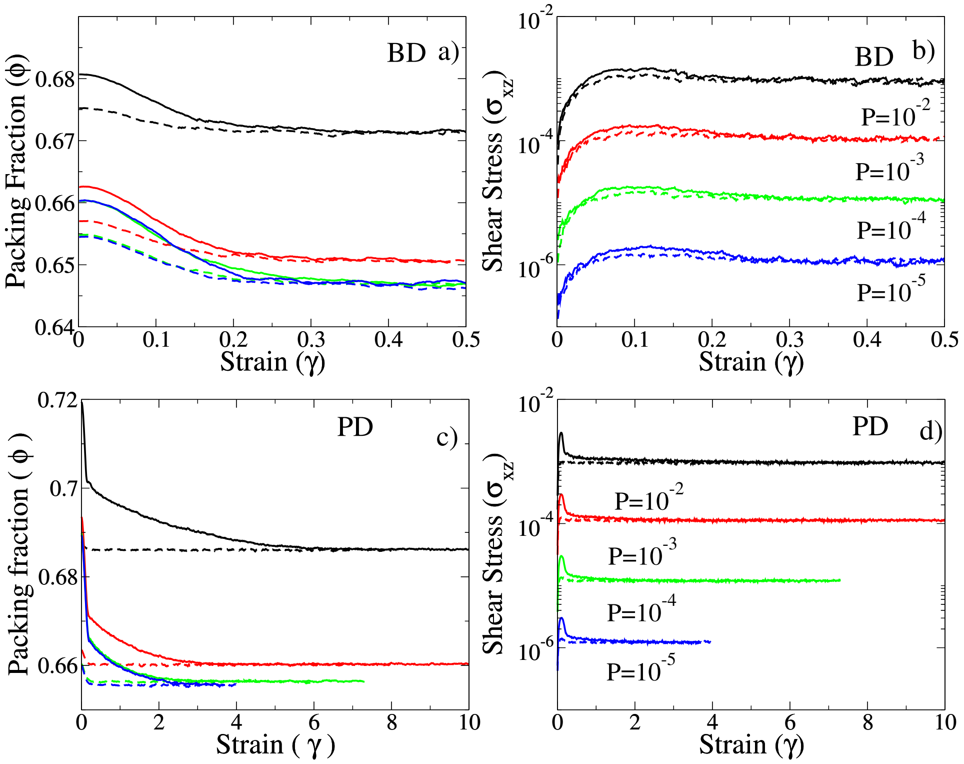

Figure 2.7: **Dilatancy.** The evolution of (a) packing fraction ϕ and (b) shear stress σ_{xz} as functions of strain γ under constant pressure AQS in the BD model, for $\phi_j = 0.654$ (dashed) and $\phi_j = 0.66$ (solid), and for a few different pressures P (indicated in (b)). (c,d) Same data in the PD model (P values indicated in (d)), for $\phi_j = 0.660$ (dashed) and $\phi_j = 0.689$ (solid). The data are averaged over 10 and 64 independent samples in BD and PD systems respectively.

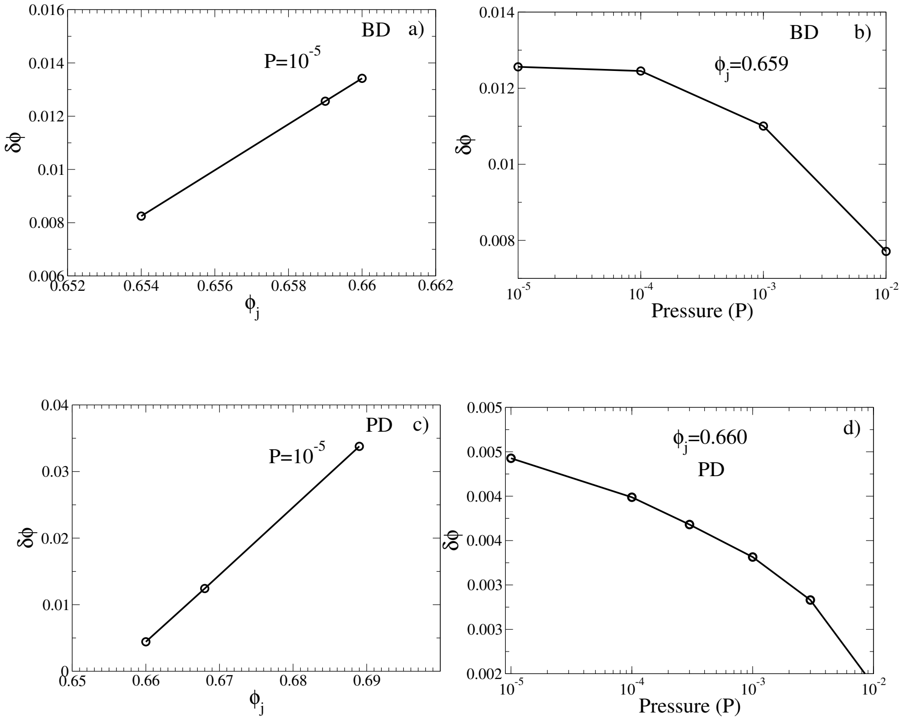

Figure 2.8: **Degree of dilation in constant pressure shear deformations. a) and c)** Degree of dilation $\delta\phi$ as a function of ϕ_j for a given pressure P, and **b) and d)** as a function of P for a given ϕ_j.

magnitude of stress overshoot is more significant in systems with larger ϕ_j. The presence of a maximum at a characteristic value of the strain is the constant pressure analog of the maximum in stress anisotropy observed in the constant volume protocol as shown in the Fig. 2.5. The development of the maximum in the stress anisotropy, or in the macroscopic friction $\mu = \sigma_{xz}/P$, therefore, seems to be a universal feature associated with shear jamming and dilatancy, in both frictionless [54] and frictional systems, under both uniform [68, 87, 88, 74] and cyclic shear deformations [72].

Figure 2.8 shows that, under constant pressure shear deformations, the degree of dilation $\delta\phi = \phi_{init} - \phi_s$, which is the difference between the initial density ϕ_{init} and the steady-state density ϕ_s, increases with the jamming density ϕ_j for a fixed pressure P, or decreases with P for a fixed ϕ_j.

The *degree of dilation* increases with ϕ_j and decreases with P, as seen from Fig. 2.7(a) and 2.7(c). In the limit $\phi_j \to \phi_J$ and $P \to 0$, the dilation effect disappears ($\delta\phi \to 0$), which is consistent with previous results [48]. The PD model shows more significant dilation, because higher ϕ_j, relative to ϕ_J, is obtained, thanks to the efficient swap algorithm. We emphasize that the dilatancy effect characterized by $\delta\phi$ is a steady-state property that is distinct from the increase of Reynolds pressure, which occurs at small strains under constant volume conditions and does not extend beyond yielding [76, 44, 89]. In contrast, the steady-state behavior is reached asymptotically at large strains often after many plastic failure events.

2.3.3 Steady state behavior

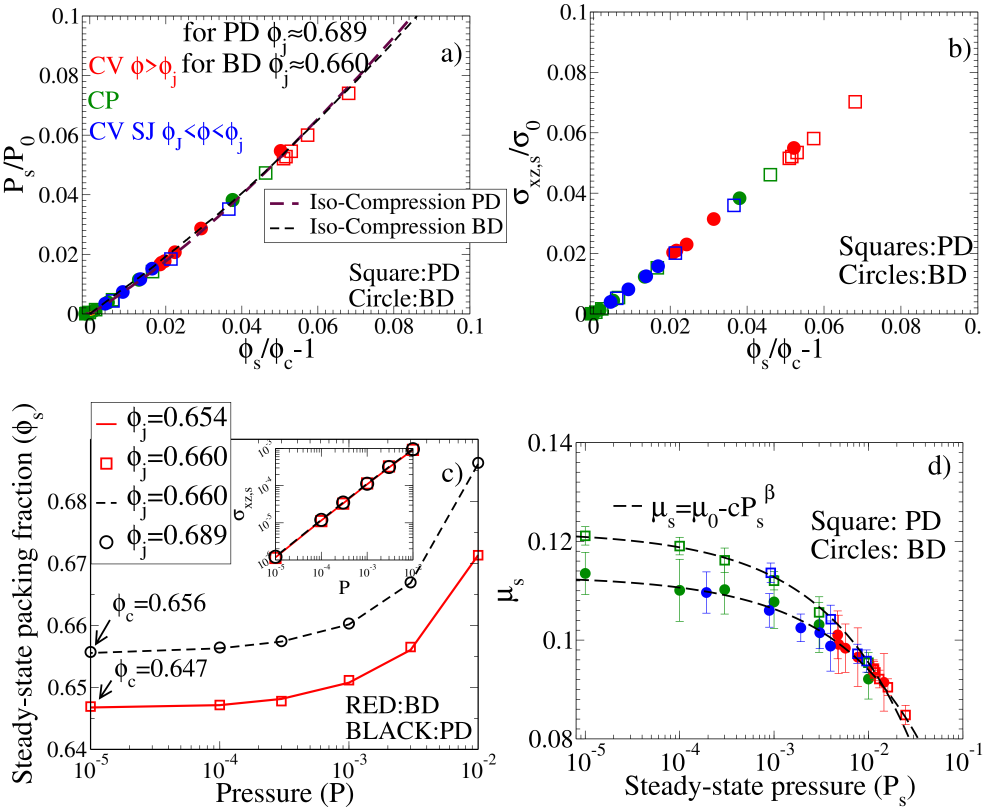

Figure 2.9: **Steady-state EOSs.** (a) The steady-state pressure P_s is a universal function of $\phi_s/\phi_c - 1$ after rescaling. The data are obtained from constant volume shear above ϕ_j (CV, red), constant volume shear below ϕ_j where shear jamming occurs (CV SJ, blue), constant pressure shear (CP, green), and isotropic compression from ϕ_J where the rescaled P_{iso} is plotted as a function of $\phi/\phi_J - 1$. See Table. 2.1 for the values of fitting parameters. (b) The rescaled Steady-state stress $\sigma_{xz,s}$ is a universal function of $\phi_s/\phi_c - 1$. (c) Steady-state density ϕ_s as a function of pressure P for different ϕ_j, obtained from constant pressure shear. Inset: the steady-state stress is independent of the jamming density for constant pressure shear deformation. (d) Macroscopic friction μ_s of steady-states as a function of pressure P_s.

The steady-states follow the EOSs, $P_s(\phi_s)$ and $\sigma_{xz,s}(\phi_s)$, which are independent of initial conditions (ϕ_j), as shown in Fig. 2.9(a) and 2.9(b). Extrapolating the EOSs to the limit of zero pressure and stress, we find that the steady-states converge to a *critical state* at density ϕ_c, i.e., $P_s(\phi_s \to \phi_c) \to$

0 and $\sigma_{xz,s}(\phi_s \to \phi_c) \to 0$, where $\phi_c \approx 0.648$ for the BD and $\phi_c \approx 0.656$ for the PD models (Fig. 2.9(c)). Within our numerical precision, the critical-state density ϕ_c coincides with the J-point density ϕ_J in large systems , $\phi_c \simeq \phi_J$, which confirms the absence of dilatancy in the limit $\phi_j \to \phi_J$. Our observation is qualitatively consistent with the mean-field theory [90], which suggests that shear jamming (and therefore dilatancy as well) diminishes with poor annealing.

Despite the fact that the steady-state stress is anisotropic, $P_s(\phi_s)$ agrees well with the isotropic EOS, $P_{iso}(\phi)$, obtained by an isotropic compression from ϕ_J (Fig. 2.9(a)). The critical scaling of P_s also obeys a linear relationship, $P_s(\phi_s) \sim \phi_s - \phi_c$, as in the isotropic jamming case, where $P_{iso} \sim \phi - \phi_J$ [8]. Fig. 2.9(a) further shows that, up to a scale factor, the EOSs for pressure collapse onto the same master curve, that is not only independent of the initial condition (ϕ_{j}), but also the polydispersity (BD or PD model), and the jamming protocol (constant volume shear, constant pressure shear, or isotropic compression). The stress EOSs $\sigma_{xz,s}(\phi_s)$ of steady-states (Fig.2.9(b)) for different shear protocols collapse on to a master curve, but unlike pressure, we cannot compare with the isotropic compression case, where the shear stress is always zero. Fig. 2.9 (c) shows the steady-state packing fraction ϕ_s *vs.* pressure, indicating more clearly the approach to the asymptotic density φ_c as pressure goes to zero, independently of protocol, but the value of φ_c is different for the two studied systems. Figure 2.9 (d) shows that, the macroscopic friction of steady states $\mu_s = \sigma_{xz,s}/P_s$ is non-zero, and slowly decreases with pressure as $\mu_s = \mu_0 - cP_s^{\beta}$ [91], where $\mu_0 = 0.113, \beta = 0.453$ for the BD model, and $\mu_0 = 0.122, \beta = 0.458$ for the PD model (see also Fig. 2.10). The exponent β is model-independent within the numerical error and close to (and not distinguishable within the precision of our data from) the value of 0.5 reported in [91]. The values of μ_0 are also close to the previously reported data $\mu_0 \simeq 0.1$ for mono-disperse spheres with Hertzian interactions [48]. This scaling of μ_s suggests that, near the critical-state ($\phi_s \to \phi_c$), the stress is proportional to the pressure, $\sigma_{xz,s} \sim \mu_0 P_s$, and the stress EOS is linear, $\sigma_{xz,s}(\phi_s) \sim \phi_s - \phi_c$, as shown in Fig. 2.11b.

Equations of state of steady-states

Here we explain how to obtain the steady-state equations of state (EOSs) of pressure $P_s(\phi_s)$ and of stress $\sigma_{xz,s}(\phi_s)$. For the EOS of pressure, we firstly calculate the average pressure-strain curve $P(\gamma) = \langle P^{ind}(\gamma)\rangle$ in constant volume shear simulations where the density $\phi = \phi_s$ is fixed, or the average density-strain curve $\phi(\gamma) = \langle \phi^{ind}(\gamma)\rangle$ in constant pressure shear simulations where the pressure $P = P_s$ is fixed. Here $P^{ind}(\gamma)$ and $\phi^{ind}(\gamma)$ are the pressure and density of individual samples at strain γ, and $\langle \ldots \rangle$ represents the sample average. We then extrapolate the large-γ limits of $P(\gamma)$ and $\phi(\gamma)$ as the steady-state values P_s and ϕ_s. By varying the control parameter ϕ_s in constant volume shear, and P_s in constant pressure shear, we obtain the pressure EOS $P_s(\phi_s)$ for both protocols (Fig. 2.11). The same procedure is applied to get the stress EOS $\sigma_{xz,s}(\phi_s)$.

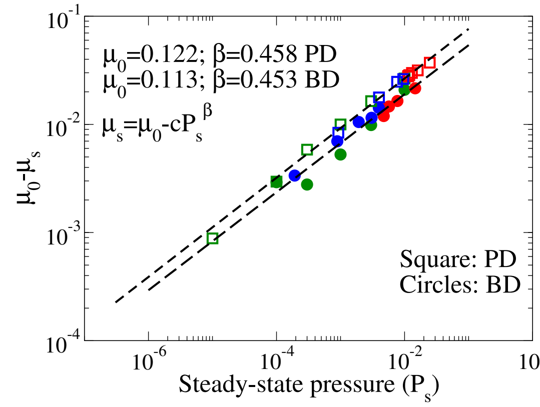

Figure 2.10: **Scaling relationship between the steady-state macroscopic friction μ_s and pressure P_s.** The data for both BD ($\phi_j \approx 0.660$) and PD ($\phi_j \approx 0.689$) systems are fitted to the empirical scaling form $\mu_s = \mu_0 - cP_s^\beta$ (dashed lines). The data obtained from constant pressure shear (green), constant volume shear for $\phi_J < \phi < \phi_j$ (shear jamming, blue), and constant volume shear for $\phi > \phi_j$ (red) are presented.

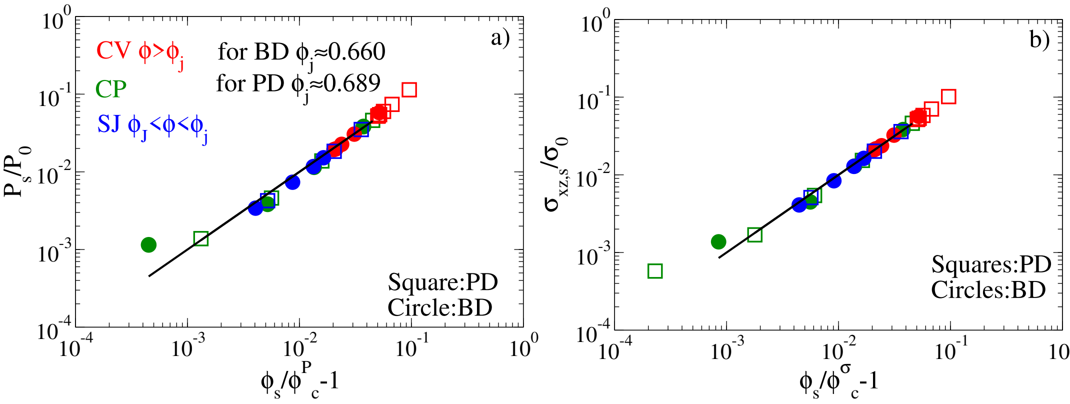

Figure 2.11: **Critical scalings of steady-states.** We fit the EOS data of (a) pressure and (b) stress to Eq. 2.3 and 2.4. The fittings are represented by solid lines.

	P_0	ϕ_c^P	σ_0	ϕ_c^σ	P_0'	ϕ_J
BD	0.261	0.647	0.024	0.647	0.29	0.648
PD	0.217	0.656	0.021	0.656	0.21	0.655

Table 2.1: Values of fitting parameters in Eq. 2.3, 2.4, and 2.5, for both BD ($\phi_j = 0.660$) and PD ($\phi_j = 0.689$) models. The steady-state data, P_0, ϕ_c^P, σ_0 and ϕ_c^σ, are obtained from constant pressure shear; the constant volume shear gives the same results because the EOSs are independent of shear protocols (see Fig. 2.11).

To estimate the density ϕ_c of the critical state, we fit the EOS data $P_s(\phi_s)$ and $\sigma_{xz,s}(\phi_s)$ to the asymptotic linear scalings near the zero pressure limit,

$$P_s(\phi_s) = P_0(\phi_s/\phi_c^P - 1), \tag{2.3}$$

and

$$\sigma_{xz,s}(\phi_s) = \sigma_0(\phi_s/\phi_c^\sigma - 1), \tag{2.4}$$

where $P_0, \sigma_0, \phi_c^P, \phi_c^\sigma$ are fitting parameters (see Fig. 2.11). The values of the fitting parameters are summarized in TABLE 2.1, which show that consistently $\phi_c^P = \phi_c^\sigma$ within the numerical uncertainty. We therefore determine the critical-state density as $\phi_c = \phi_c^P = \phi_c^\sigma$.

Equation of state of isotropic-jamming

We first measure the pressure $P_{iso}^{ind}(\Delta\phi)$ at a given $\Delta\phi = \phi - \phi_J^{ind}$ for each individual sample, where ϕ_J^{ind} is the individual sample jamming density determined according to the jamming criterion described in the methods section. To do that, we compress the configuration from ϕ_J^{ind} in small increments of density $\delta\phi = 10^{-4}$, up to the target density $\phi > \phi_J^{ind}$. We then average over samples to obtain the EOS, $P_{iso}(\Delta\phi) = \langle P_{iso}^{ind}(\Delta\phi)\rangle$. The isotropic jamming density ϕ_J is determined from the average value of ϕ_J^{ind}, $\phi_J = \langle\phi_J^{ind}\rangle$. The isotropic jamming EOS satisfies the linear scaling near ϕ_J,

$$P_{iso}(\phi) = P_0'(\phi/\phi_J - 1), \tag{2.5}$$

where $P_0' = 0.29$ (BD model) and 0.21 (PD model) are used to re-scale P_{iso} such that the isotropic jamming and the steady-sate EOSs collapse onto the universal curve (Fig. 3a). The values of ϕ_J and P_0' are listed in Table 2.1.

2.3.4 Generalized zero-temperature phase diagram

To summarize the above described behaviors on shear jamming and dilatancy, we propose a generalized zero-temperature jamming phase diagram. The original jamming phase diagram, introduced by Liu and Nagel [61], conjectures that, in the athermal limit, the jammed states at ϕ_J should be extremely fragile under shear – the yield stress vanishes at ϕ_J continuously from above jamming, $\sigma_Y(\phi_J) = 0$, suggesting that infinitesimal shear stress is required to yield (unjam) a packing at ϕ_J. While this picture is well supported by previous numerical studies where $\phi_j \approx \phi_J$ [92, 8, 48], here we show explicitly a remarkable discontinuity of the yield stress σ_Y (as well as the yield pressure P_Y) at the jamming density ϕ_j, when $\phi_j > \phi_J$. (see Fig. 2.12 for the PD system and Fig. 2.13 for the BD system). This discontinuous nature is independent of the definition of σ_Y (here we define $\sigma_Y = \sigma_s$, see Fig. 2.14 for other definitions).

On the contrary, the pressure P_{iso} under isotropic compression vanishes continuously at ϕ_j (Fig. 2.12 (a)), which is independent of ϕ_j, as shown previously [5]. It demonstrates the reason why under constant pressure shear, the volume expands from the initial isotropic states to the final steady-states (Fig. 2.7), and the unjammed states below ϕ_j jam under constant volume shear, as

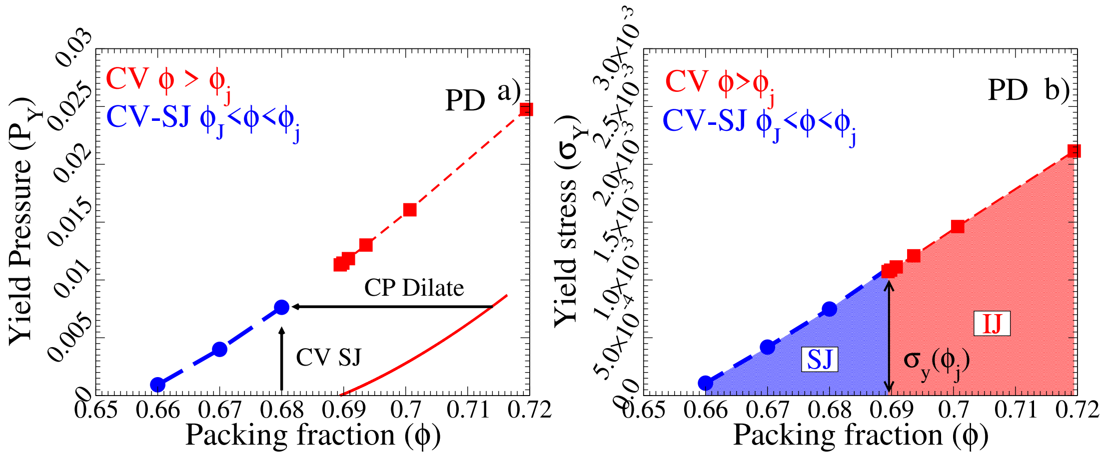

Figure 2.12: **Generalized zero-temperature jamming phase diagram.** (a) Yield pressure P_Y (where $P_Y = P_s$) and (b) yield stress σ_Y (where $\sigma_Y = \sigma_s$) as functions of volume fraction ϕ, obtained from constant volume shear of PD systems above $\phi_j = 0.689$ (red points) and below (blue points). Above ϕ_j, the system is initially jammed by the isotropic compression (IJ), and remains jammed under shear as long as $\sigma_{xz} < \sigma_Y$, while below ϕ_j, the initially unjammed system is shear jammed (SJ) at γ_j (Fig. 2.2), and becomes unjammed again (yields) once σ_{xz} reaches σ_Y. The isotropic compression EOS $P_{iso}(\phi)$ is also plotted (red line). The same data are shown in Fig. 2.9(a) and (b) in rescaled plots.

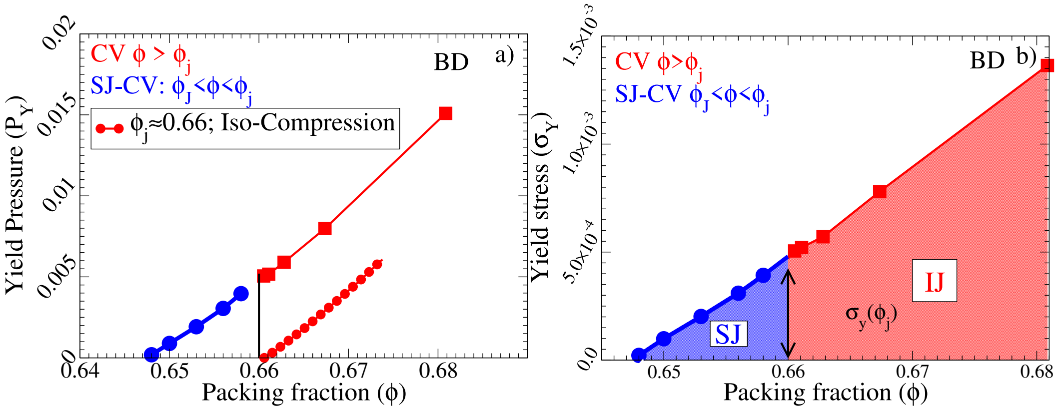

Figure 2.13: **Generalized zero-temperature jamming phase diagram for the BD model. a)** Yield pressure ($P_Y = P_s$) as a function of packing density ϕ, obtained by constant volume shear deformations for both $\phi > \phi_j = 0.66$ (isotropic jamming, IJ) and $\phi < \phi_j$ (shear jamming, SJ). The isotropic compression pressure $P_{\rm iso}$ is also plotted. **b)** Yield stress ($\sigma_Y = \sigma_{xz,s}$) as a function of ϕ.

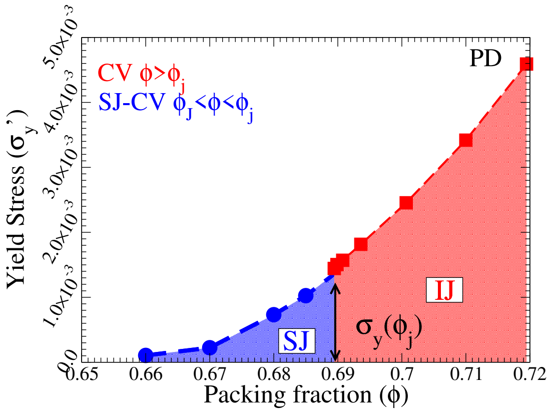

Figure 2.14: **Generalized zero-temperature jamming phase diagram for the PD model, where the yield stress σ'_Y is defined as the peak value of the shear stress in the stress-strain curve.** The jamming density is $\phi_j = 0.689$.

shown in Fig. 2.2. Interestingly, the yield stress σ_Y of shear jammed systems at a constant density ϕ below ϕ_j is a continuation of that of isotropically jammed ones. This observation is consistent with the universality of the EOSs as shown in Fig. 2.9. The stress jump $\sigma_Y(\phi_j)$ at the isotropic jamming transition point ϕ_j vanishes as $\phi_j \to \phi_J$, as does the regime of frictionless shear jamming.

2.4 Conclusions

We conclude by firstly comparing the dilatancy effect between amorphous and crystal/polycrystal assemblies. In the seminal paper [45] where the concept of dilatancy was introduced for the first time, Reynolds proposed a pure geometric mechanism based on the idea that one type of lattice packing (e.g., a tetrahedral arrangement) could expand its volume under shear by transforming into another type of lattice packing (e.g., a cubic arrangement) Here we recover the same geometric mechanism for amorphous packings, which has been missed in previous studies [48, 49]. Like lattices, the amorphous ensemble also includes multiple states with different packing densities, although jammed packings at $\phi_j = \phi_J$ are more abundant. The paths connecting these states, driven by external agitations such as shear, are accompanied by dilatancy, shear jamming, and additional rich phenomena such as avalanches, plasticity, shear softening and hardening, and yielding.

There are a couple of parallel studies[93, 94] focusing on frictionless shear jamming. Here we show that shear jamming is necessarily associated to another interesting phenomenon, shear dilatancy, in frictionless granular systems. We further reveal the universality of the EOSs of dilated systems (steady-states at large strains) and those of isotropic jamming (initial states at the zero strain). The evolution from the initial states to the steady-states is highly non-trivial, for which the Liu-Nagel jamming diagram has to be generalized.

Chapter 3

Criticality of the frictionless shear jamming transition[1]

---

[1] The contents of this chapter has been published as "**Babu, Varghese, and Srikanth Sastry. "Criticality and marginal stability of the shear jamming transition of frictionless soft spheres." Physical Review E 105, no. 4 (2022): L042901.**"

3.1 Introduction

As mentioned in the introduction, the jamming density ϕ_J has many properties of a critical point. The configurations at ϕ_J are isostatic with average co-ordination number $z = 2d = z_{iso}$, where d is the spatial dimension [8, 9, 12]. As the system is compressed above the jamming density (for soft-spheres) the excess co-ordination number $\delta z = z - z_{iso}$ scales as $\delta z \sim (\phi - \phi_J)^{\frac{1}{2}}$, independent of the interaction potential and the configurations are mechanically stable [9, 8, 12]. The pressure vanishes linearly with $(\phi - \phi_J)$, with a pre-factor depending on the interaction potential [8, 5, 12]. Close to, and above, the jamming density, the vibrational density of states (VDOS) $D(\omega)$, where ω is the frequency, displays anomalous behavior, with the presence of excess low-frequency modes compared to the Debye solid which describe a normal elastic medium, with a characteristic frequency ω^* vanishing as the jamming point is approached, with a power law dependence on $(\phi - \phi_J)$ [95, 96, 14]. Such aspects of critical-like behaviour near the jamming point has been widely investigated and established [12, 97].

The requirement of mechanical stability of jammed packings has been shown to imply an inequality, or bound, between exponents that characterise the distribution of inter-particle forces f, which exhibits a power law form $P_e(f) \sim f^{\theta_e}$ at small forces, and the distribution of distances, or gaps h, between particles that are nearly in contact, which exhibits a well known power-law singularity, $g(h) \sim h^{-\gamma}$ [23, 22]. The bound, $\gamma \geq 1/(2 + \theta_e)$, was argued to be saturated at jamming [23] and that such a *marginal stability condition* provided a mechanism to explain the avalanches of rearrangement observed [98, 75].

The mean field theory of glass transition in hard spheres in the limit of infinite dimensions [99, 28], interestingly, leads to predictions concerning the behavior at jamming, and in particular a prediction for the exponents θ_e and γ to be $\theta_e = 0.42311..$ and $\gamma = 0.41269...$ While the predicted value of γ is close to those observed in two (2D) and three dimensional (3D) packings, as well as higher dimensions [21], leading to the possibility that $d = 2$ constitutes the upper critical dimension for the jamming transition, the reported values of exponent θ [100, 22, 21] exhibits a wide range. However, as noted in [22], the presence of localized excitations in finite dimensions leads to a modified distribution $P_l(f) \sim f^{\theta_l}$ and marginal stability condition $\gamma \geq (1 - \theta_l)/2$. The localized excitations were associated with sphere arrangements prone to buckling, or *bucklers*, in [24], and separating out the distributions of forces corresponding to bucklers leads to the verification of marginal stability condition, with the exponents predicted by mean field theory.

In this chapter, we examine the validity of these aspects of criticality and marginal stability for the shear jamming transition for frictionless soft spheres in two and three dimensions, and show that they are indeed valid. The jamming of granular matter under shear has been observed experimentally [37, 44] and numerically [52, 55, 69] for frictional systems. However friction is not necessary for the shear jamming transition [54, 73, 50, 101, 93, 102, 51]. In [50], critical behavior near the shear jamming transition for frictionless soft spheres were considered in 3D. Although the density range over which shear jamming occurs was seen to vanish in the thermodynamic limit, the behavior of the pressure, contact number z and the bulk modulus were shown to exhibit the same behavior as a function of shear stress (equivalently, shear strain above the jamming strain)

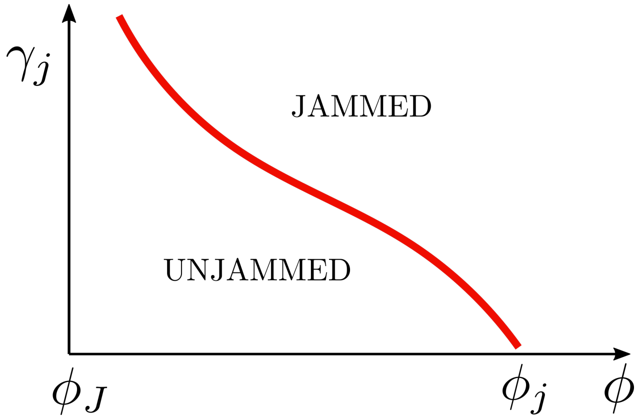

Figure 3.1: Schematic showing the existence of shear jamming for configurations above the minimum jamming density ϕ_J.

as at the isotropic jamming point. The key difference is that both the bulk modulus B and the shear modulus G remain finite at the shear jamming point, unlike the isotropic case where only the bulk modulus is finite. Nevertheless, only a single eigenvalue of the elastic modulus tensor becomes finite, and the finite values of B and G can be understood in terms of a rotation of the eigenvectors, leading to the conclusion that shear jamming and isotropic have the same symmetry and critical behavior. Similar conclusions have been arrived at in other investigations [76, 93].

It is therefore of interest to investigate the critical behavior of shear jamming over such density intervals, which we do, building on previous work [50, 102, 69, 93]. With the distance from the shear jamming strain $\gamma - \gamma_j$ playing the role of the excess density above jamming, $\phi - \phi_j$ for isotropic jamming, we find that the scaling of pressure, excess contact number and shear stress and the behavior of the VDOS $D(\omega)$ is the same as at isotropic jamming. In addition, we explore in detail the marginal stability condition, employing the approach of [24] to distinguish localized excitations, or *bucklers*, and demonstrate that the behavior for shear jamming is consistent with that for isotropic jamming and mean field predictions. Other than a preliminary investigation in [55], the applicability of the marginal stability condition for shear jamming has not been investigated. Our results thus clearly demonstrate that properties related to criticality and marginal stability for shear jamming are the same as for isotropic jamming.

3.2 Models and Methods

The systems we study are bi-disperse soft sphere mixtures $(50:50)$ in 2D and 3D with a harmonic repulsive inter-particle potential. The interaction potential is given by $v(|\vec{r}_{ij}|) = \epsilon(1 - \frac{|\vec{r}_{ij}|}{\sigma_{ij}})^2$ for $|\vec{r}_{ij}| \leq \sigma_{ij}$ where $\vec{r}_{ij}$ is the vector connecting the centers of particles i and j and $\sigma_{ij} = \frac{\sigma_i + \sigma_j}{2}$ with σ_k being the diameter of particle type k ($\sigma_2/\sigma_1 = 1.4$). The first step in our study involves generating configurations with jamming density $\phi_j > \phi_J$. For this we follow the protocol similar to the one used in [5] which we describe for $d = 3$ briefly; other procedures that could be employed are outlined in [53, 101]. At the packing fraction $\phi = 0.5935$ we generate configurations by initializing particle centers randomly and performing an energy minimization to generate a configurations with no overlaps (A configuration with no overlap is considered unjammed). This configuration is treated as a configuration of hard-spheres and equilibrated by hard-sphere Monte Carlo simulation using HOOMD [103, 104]. We then compress the system in steps of $\delta\phi = 10^{-4}$, performing an energy minimization after each compression. Compression is carried out by changing the box dimensions of the system. When the jamming density ϕ_j is crossed, the energy after minimization e/N will be greater than 10^{-24}. When the energy crosses a threshold (here $\frac{e}{N} > 10^{-7}$) we stop the compression and start decompressing the system with smaller steps of $\delta\phi = 10^{-5}$. During the decompression when we are able to minimize the energy to $\frac{e}{N} < 10^{-24}$ we stop the process and identify the jamming density. The jamming densities obtained through the procedure is distributed around $\phi \approx 0.661$, which depends on the density of the initial equilibrated fluid [5]. From the configurations at ϕ_j we generate unjammed configurations at $\phi_J < \phi < \phi_j$ by scaling the volume.

These configurations are sheared uniformly using Athermal Quasi Static (AQS) shear to observe shear jamming at a strain γ_j, employing LAMMPS [83]. AQS shear for a strain step $\delta\gamma$ is carried out by performing an affine transformation $x_i \rightarrow x_i + \delta\gamma \times y_i; y_i \rightarrow y_i; z_i \rightarrow z_i$ of coordinates followed by energy minimization. We generate configurations close to the jamming strain γ_j and identify γ_j as follows: We increment strain in steps of $\delta\gamma = 10^{-3}$ until $\frac{e}{N} > e_{thresh} = 10^{-7}$, at which point we redefine the strain step and threshold energy as $\delta\gamma \rightarrow -1 \times \delta\gamma/10$ and $e_{thresh} \rightarrow e_{thresh}/10$. The system is strained in the reverse direction until $\frac{e}{N} < 10^{-20}$ where updates to e_{thresh} and $\delta\gamma$ are implemented again. This procedure is stopped when $\delta\gamma < 10^{-6}$ and $\frac{e}{N} < 10^{-20}$ and the system is being reverse strained.

Using this procedure we are able to obtain configurations close to the jamming strain, but to study the marginal stability of the shear jamming transition we need to generate configurations that are *just* shear-jammed. Quantitatively this means the configurations has a single self-stress state, or the contact network has one unique force-balance solution [24]. For a given jammed configuration with N_c contacts and N particles which are not rattlers, the number of self-stressed states is given by $N_{ss} = N_c - (N-1)d$ with periodic boundary conditions [24]. We observe that for large system sizes configurations obtained using the SJ procedure to obtain shear jammed configurations are not close enough to jamming and have multiple self-stressed states.

To obtain configurations with single self-stressed state we adapt the procedure described for isotropic jamming in [24] for shear jamming.

3.2.1 Iterative procedure to generate configurations with single self-stressed states ($N_{SS} = 1$)

We now describe the iterative procedure to generate configuration with a single self-stressed state. The potential energy U scales with respect to the distance from the jamming strain γ_j as

$$U \propto (\gamma - \gamma_j)^2 \tag{3.1}$$

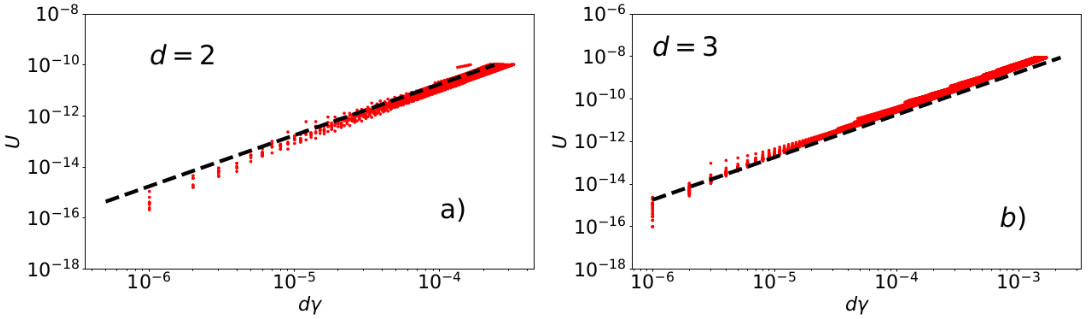

Figure 3.2: Evolution of potential energy U during the final reverse shear from the SJ procedure. $U \sim d\gamma^2$, this information is used in IP to go closer to γ_J for **a)** $d = 2$ **b)** $d = 3$

This dependence is shown in Fig. 3.2 for two and three dimensions. If we assume that we know the value of γ_j, and start with an initial jammed configuration at $\gamma_0 > \gamma_j$, we can generate n logarithmically placed configurations between γ_0 and $\gamma_j + (\gamma_0 - \gamma_j) \times 10^{-1}$ using the iteration

$$\begin{aligned} \log(\gamma_{i+1} - \gamma_J) - \log(\gamma_i - \gamma_J) &= -\frac{1}{n} \\ \gamma_{i+1} &= \gamma_J + (\gamma_i - \gamma_J) \times 10^{-\frac{1}{n}} \end{aligned} \tag{3.2}$$

However, we do not know the precise value of γ_j, but can iteratively approximate γ_j as well. From Eq. 3.1 we have

$$\begin{aligned} \sqrt{\frac{U_{i+1}}{U_i}} &= \frac{\gamma_{i+1} - \gamma_J}{\gamma_i - \gamma_J} \\ \gamma_J &= \frac{\gamma_{i+1} - \gamma_i \times \sqrt{\frac{U_{i+1}}{U_i}}}{\left(1 - \sqrt{\frac{U_{i+1}}{U_i}}\right)} \end{aligned} \tag{3.3}$$

If we calculate a new strain γ_{i+1} using Eq. 3.2 and use that strain to calculate a new jamming strain using Eq. 3.3, then we have an iterative procedure to approximate γ_j better and also find configurations close to it. With $\tilde{\gamma}_i$ being the jamming strain estimated at the i'th iteration, we have

$$\gamma_{i+1} = \tilde{\gamma}_i + (\gamma_i - \tilde{\gamma}_i) \times 10^{-\frac{1}{n}} \tag{3.4}$$

$$\tilde{\gamma}_{i+1} = \frac{\gamma_{i+1} - \gamma_i \times \sqrt{\frac{U_{i+1}}{U_i}}}{\left(1 - \sqrt{\frac{U_{i+1}}{U_i}}\right)} \tag{3.5}$$

Configurations generated using this procedure are analyzed by removing the rattlers recursively. After removing the rattlers if the configurations satisfies $N_c = (N-1)d + 1$ then the configuration has only one self-stressed state and we use it for the force and gap distribution analysis, while others are discarded.

Using this procedure we generate shear-jammed configurations with a single self-stressed state, whose structure and forces we analyze to study the marginal stability condition. We follow similar procedures for the data regarding the isotropic case, with density instead of the strain as the control variable.

3.2.2 Hessian and the stiffness matrix

In a $d = 3$ system we have a total of 6 independent strain direction represented as $\eta_{xx}, \eta_{yy}, \eta_{zz}, \eta_{xz}, \eta_{yz}, \eta_{xy}$. Deforming the system costs energy and all deformations are a linear sum of these strains. We define therefore the matrix of elastic constants.

$$C_{\alpha\beta\gamma\sigma} = \frac{1}{V}\frac{d^2U}{d\eta_{\alpha\beta}d\eta_{\gamma\delta}}$$

or the stiffness matrix. The elastic constants for a configuration at mechanical equilibrium is given by [105]

$$C_{\alpha\beta\kappa\lambda} = \frac{1}{V}\frac{\partial^2 U}{\partial\eta_{\alpha\beta}\partial\eta_{\kappa\lambda}} + \frac{1}{V}\sum_{ij,\chi\delta} \boldsymbol{\Xi}^{i\chi}_{\alpha\beta}.(\boldsymbol{H^{-1}}^{\chi\delta}_{ij}.\boldsymbol{\Xi}^{j\delta}_{\kappa\lambda}) \tag{3.6}$$

where

$$\boldsymbol{H}^{\alpha\beta}_{ij} = \frac{\partial^2 U}{\partial r_{i\alpha}\partial r_{j\beta}}$$

is the Hessian and

$$\boldsymbol{\Xi}^{i\alpha}_{\kappa\lambda} = -\frac{\partial^2 U}{\partial r_{i\alpha}\partial\eta_{\kappa\lambda}}$$

In Eq. 3.6 the first term represents the contribution to elastic constant due to the affine displacement of the particles. The second term can be understood as follows. During AQS shear protocol, the first step is the affine transformation of the particle co-ordinates according to the strain applied. After this affine transformation there will be forces which are unbalanced, give rise to the non-affine displacement field of the particles. The contribution of these non-affine displacements is the second term of Eq. 3.6.

For a system of particles interacting *via* a pair-wise potential, the expression for $C_{\alpha\beta\kappa\lambda}$ above can be evaluated as follows. Defining

$$t_{ij} = \frac{\partial u(r_{ij})}{\partial r_{ij}}; c_{ij} = \frac{\partial^2 u(r_{ij})}{\partial r_{ij}^2}$$

we have

$$\boldsymbol{\Xi}^{i\alpha}_{\kappa\lambda} = -\sum_j (r_{ij}c_{ij} - t_{ij})\eta^{\alpha}_{ij}\eta^{\kappa}_{ij}\eta^{\lambda}_{ij} \tag{3.7}$$

and

$$\frac{\partial^2 U}{\partial \eta_{\alpha\beta} \partial \eta_{\kappa\lambda}} = \frac{1}{V} \sum_{ij} (r_{ij} c_{ij} - t_{ij}) r_{ij} \eta_{ij}^{\alpha} \eta_{ij}^{\beta} \eta_{ij}^{\kappa} \eta_{ij}^{\lambda} \tag{3.8}$$

where r_{ij} is the distance between the centers of particles that are in contact and $\hat{n}_{ij}$ is the unit vector connecting the centers of the two particles.

Using Eq. 3.7 and Eq. 3.8 in Eq. 3.6 and using the eigenvectors of the Hessian we can calculate the elastic constants. Derivation of equation(3.6) and other details can be found in [105].

After calculating the stiffness matrix, we diagonalize the matrix to get the eigenvalues and eigenvectors. It is observed that close to the jamming strain some eigen-values take negative values. As discussed in [106] the procedures used to generate jammed configurations does not guarantee that the configurations are stable against any strain perturbation. Therefore these configurations generally can have negative eigenvalues for the stiffness matrix. In calculating the scaling of eigenvalues near jamming, we discard configurations for which any of the eigenvalues are negative. We have compared the values of the stiffness matrix elements obtained using Eq. 3.6 with the values obtained through a finite difference formula and have confirmed that consistent results are obtained.

3.2.3 Fabric Anisotropy

The fabric tensor is defined as

$$\boldsymbol{F} = \frac{1}{V} \sum_{i<j} \frac{\vec{r}_{ij}}{|\vec{r}_{ij}|} \otimes \frac{\vec{r}_{ij}}{|\vec{r}_{ij}|}$$

This is analogous to the stress tensor and one can compute the eigenvalues of this tensor. The fabric anisotropy is defined as

$$R_A = \frac{\lambda_1 - \lambda_3}{\lambda_1 + \lambda_2 + \lambda_3}$$

where the $\lambda_1 > \lambda_2 > \lambda_3$. The fabric anisotropy being zero implies that no direction in space is special and therefore the system is iso-tropic. The anisotropy of the configurations that are shear jammed at different densities is shown in Fig.3.5. R_A has a non-monotonic behavior and it approaches zero as we shear jam configurations close to the isotropic jamming density ϕ_j.

The components of the stress tensor are calculated using $\sigma_{\alpha\beta} = \frac{1}{V} \sum_{i<j} f_{ij}^{\alpha} r_{ij}^{\beta}$, where f_{ij} are the inter-particle forces, and the pressure as $P = \frac{1}{3} \operatorname{tr}(\sigma)$. We calculate the density of states $D(\omega)$ which is the distribution of $\omega = \sqrt{\lambda}$ where λ's are the eigenvalues of the Hessian, for configurations over a range of strains above the jamming strain. As in the case of isotropic jamming we observe a plateau in $D(\omega)$ for small ω, before $D(\omega)$ decreases to zero as $\omega \to 0$. The frequency ω^* at which $D(\omega)$ decreases to half the plateau value is identified as the crossover frequency.

We note that the jammed configurations analyzed contain *rattlers*, particles with less than $d + 1$ contacts. We remove rattlers recursively, by identifying them in each iteration from the configurations till no rattlers remain. The percentage of rattler particles is approximately 0.05% for the cases considered. The average contact number, as well as distribution of gaps and forces reported, are obtained after the rattlers are removed. However, the packing fractions we report are calculated with the total number of particles.

3.3 Results

3.3.1 Critical Scaling

Stress and pressure

In Fig. 3.3(a), we show the variation of the shear stress σ_{xy} vs $d\gamma$ for 3D, demonstrating linear behavior $\sigma_{xy} \sim d\gamma$ above the jamming strain. The pressure exhibits the same linear behavior and the excess contact number $\delta z = z - z_c$ varies with the distance from the jamming strain as $\delta z \sim \sqrt{d\gamma}$, with $z_c = 2d$, as observed for isotropic jamming. We show the scaling of the pressure and δz with $d\gamma$ in Fig. 3.4.

Density of states

In Fig. 3.3(b), we show the VDOS $D(\omega)$, which exhibits a plateau at low frequencies corresponding to excess modes, which extend towards zero frequency as the jamming strain is approached from above. The frequency at which the crossover to the plateau occurs, $\omega^* \sim \delta\phi^{\frac{1}{2}}$ for isotropic jamming [95, 14], and we observe the same scaling near the shear jamming transition, as shown in Fig. 3.3(b)(inset).

Eigenvalues of the stiffness matrix

In Fig. 3.3 (c), we show the eigenvalues of the stiffness matrix, investigated in [50] for shear jamming in frictionless packings. As in [50], we find a nearly constant largest eigenvalue that is finite at the shear jamming point, and five nearly degenerate (but less so than in [50]) eigenvalues which are zero at shear jamming, and whose magnitude grows roughly as $d\gamma^{1/2}$ for larger strains. In Fig. 3.3(d) we show the overlap of the eigenvector corresponding to the largest eigenvalue with the bulk strain direction and the shear strain direction, as a function of density ϕ. Interestingly, the overlap of shear strain with the stiffest eigenvector shows a non-monotonic behavior. This is correlated with the anisotropy of the configurations at shear jamming, quantified by the fabric anisotropy, which also shows a similar non-monotonic behavior with changing ϕ, as shown in Fig. 3.5, and also observed in [93]. These results taken together demonstrate that the nature of criticality near the shear jamming point is the same as that near the isotropic jamming point.

3.3.2 Force exponent

We now describe the results regarding the forces and the structure of the shear jammed configurations. It is convenient to consider the cumulative probability of forces, $G(f) = \int_0^f P(f')df'$. With the gap defined as $h = \frac{r-\sigma}{\sigma}$, the cumulative probability of gaps is $G(h) = \int_0^h P(h')dh'$. For isotropic

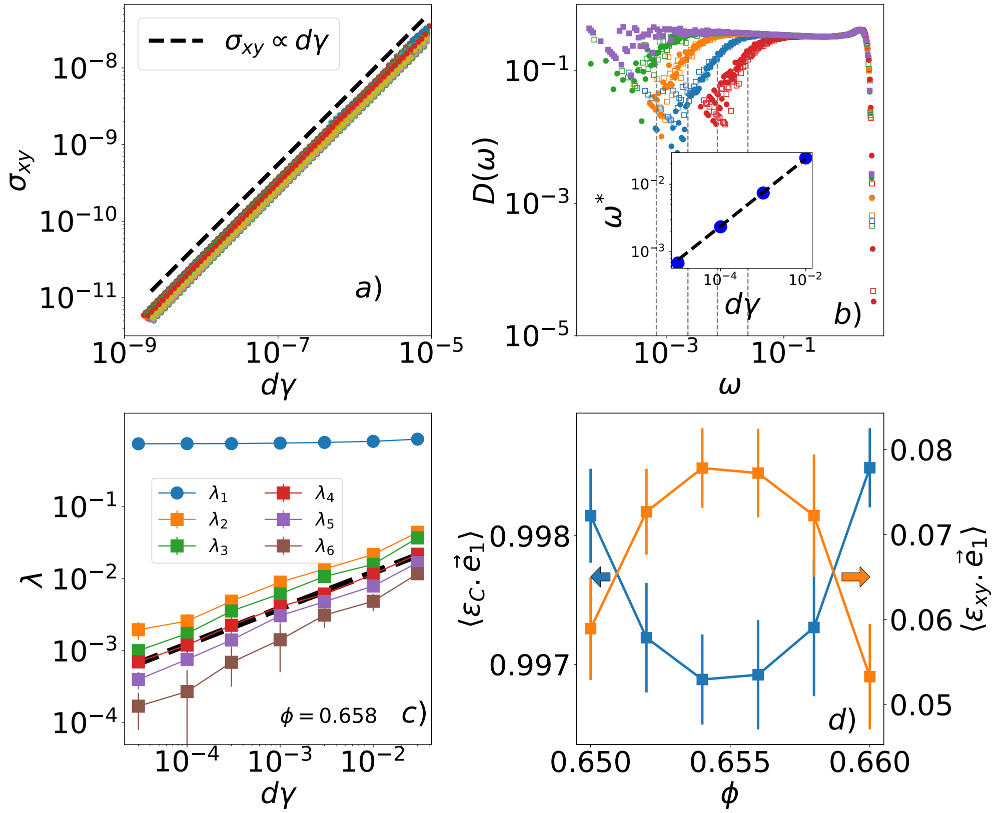

Figure 3.3: **a)** Stress σ_{xy} vs $d\gamma = \gamma - \gamma_j$ obtained by the iterative procedure with fit line $\sigma_{xy} \sim d\gamma$. **b)** VDOS $D(\omega)$ of configurations at various $d\gamma$. The green, orange, blue and red symbols represent $d\gamma = 10^{-5}, 10^{-4}, 10^{-3}, 10^{-2}$ respectively. The square and circle symbols represent $\phi = 0.658, 0.656$ respectively. The violet curve is $D(\omega)$ calculated for isotropically jammed configurations with $N_{SS} = 1$. **Inset:** The cross-over frequency ω^* is calculated by choosing the frequency at which $D(\omega)$ becomes approximately half of the plateau value. These values are marked in **b)**. The spaced line shows the scaling $\omega^* \sim d\gamma^{\frac{1}{2}}$. **c)** Eigenvalues of the stiffness matrix λ_i as a function of $d\gamma$ (for $N = 8192$). One eigenvalue is significantly larger than the others and this corresponds to the bulk and shear modulus C_{xyxy}. The dashed line denotes an exponent of $\frac{1}{2}$. $\lambda_i > \lambda_{i+1}$ **d)** Inner product of the eigenvector corresponding to the largest eigenvalue $\vec{e}_1$ of the stiffness matrix (for $d\gamma = 10^{-5}$) with compressive (blue) and shear (orange) strain directions.

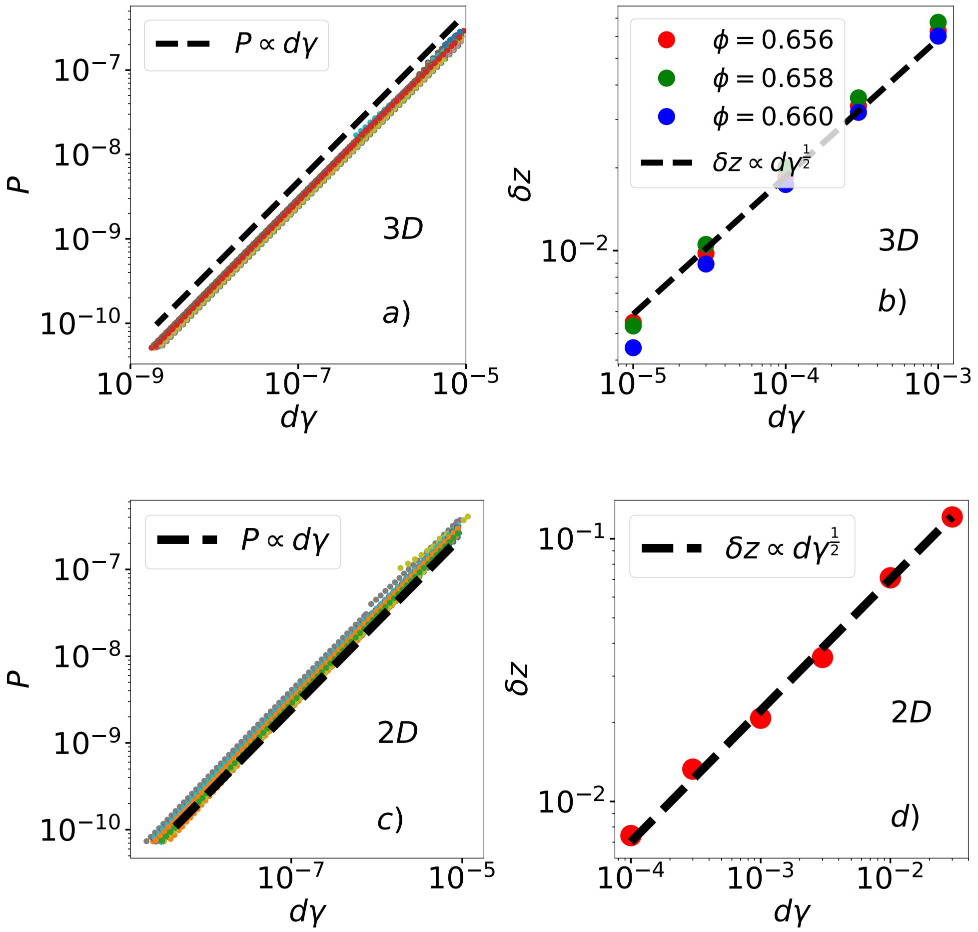

Figure 3.4: Scaling near the shear jamming transition for 3D and 2D soft-spheres **a)** Pressure $P \sim d\gamma$. Data is from the iterative procedure IP. Data from individual runs are shown. **b)** Excess contact number $\delta z \sim d\gamma^{\frac{1}{2}}$. **c)** and **d)** are the corresponding results in 2D. In **c)**, **d)** the density is 0.8499.

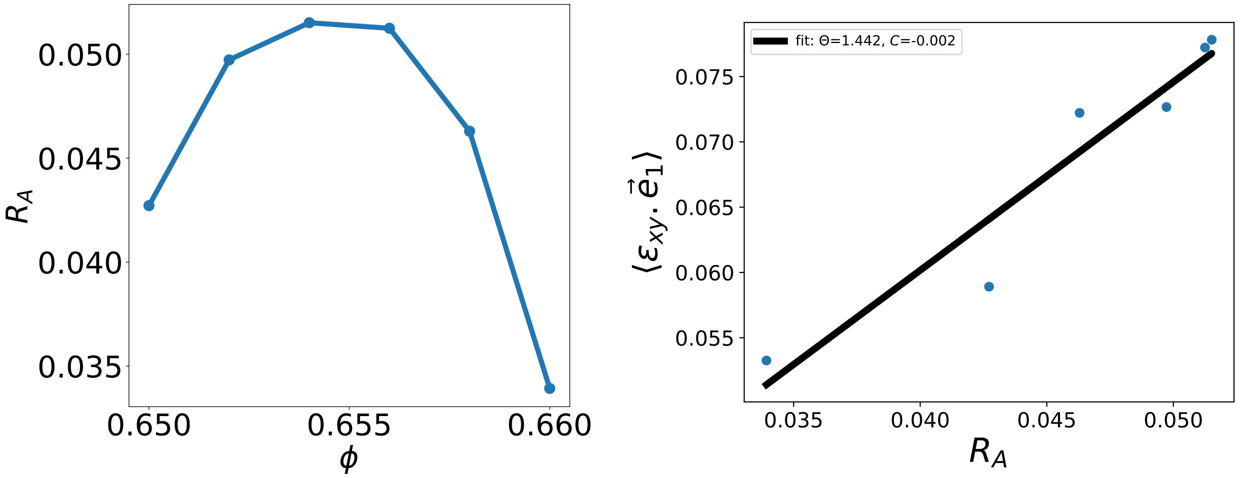

(a) (b)

Figure 3.5: Fabric anisotropy R_A of shear jammed configurations at different densities above ϕ_J. The anisotropy shows a non-monotonic behavior similar to the projection of the strain vector on the stiffest eigen-vector of the stiffness matrix. b) The scatter plot of the projection of shear strain on the first eigenvector and the fabric anisotropy shows a linear dependence.

jamming, the cumulative probability for forces (normalized to the mean value) is described by a power law $G(f/\langle f \rangle) \sim f^{1+\theta}$ and for gaps, $G(h) \sim h^{1-\gamma}$. As shown in [22] contacts carrying small forces can be mechanically isolated or be strongly coupled with the rest of the system. Opening a mechanically isolated contact will result in only a local rearrangement of the contact network, while opening a strongly coupled contact will result in an extended response. Small forces which correspond to localized modes have a distribution characterized by exponent θ_l and the forces corresponding to extended modes are characterized by exponent θ_e. The inequalities discussed in [22] in the two cases are,

$$\gamma \geq \frac{1}{2+\theta_e} \quad ; \quad \gamma \geq \frac{1-\theta_l}{2} \tag{3.9}$$

If the jammed system is marginally stable and the above inequalities Eq. 3.9 are saturated (if they become equalities) then the following relation holds:

$$\theta_e \gamma = \theta_l \tag{3.10}$$

The force-distribution calculated by including all the forces in the system is characterized by exponent $\theta = \min(\theta_l, \theta_e)$. In order to extract the θ_l and θ_e, we have to identify contacts associated with localized and extended modes correctly. Although the mean-field theory of hard-sphere glasses does not contain a prediction for θ_l, based on the predicted values $\theta_e = 0.42311..$ and $\gamma = 0.41268..$ and Eq. 3.10, one has $\theta_l = 0.17462$. Charbonneau *et al.* [24] explored how to identify the contacts

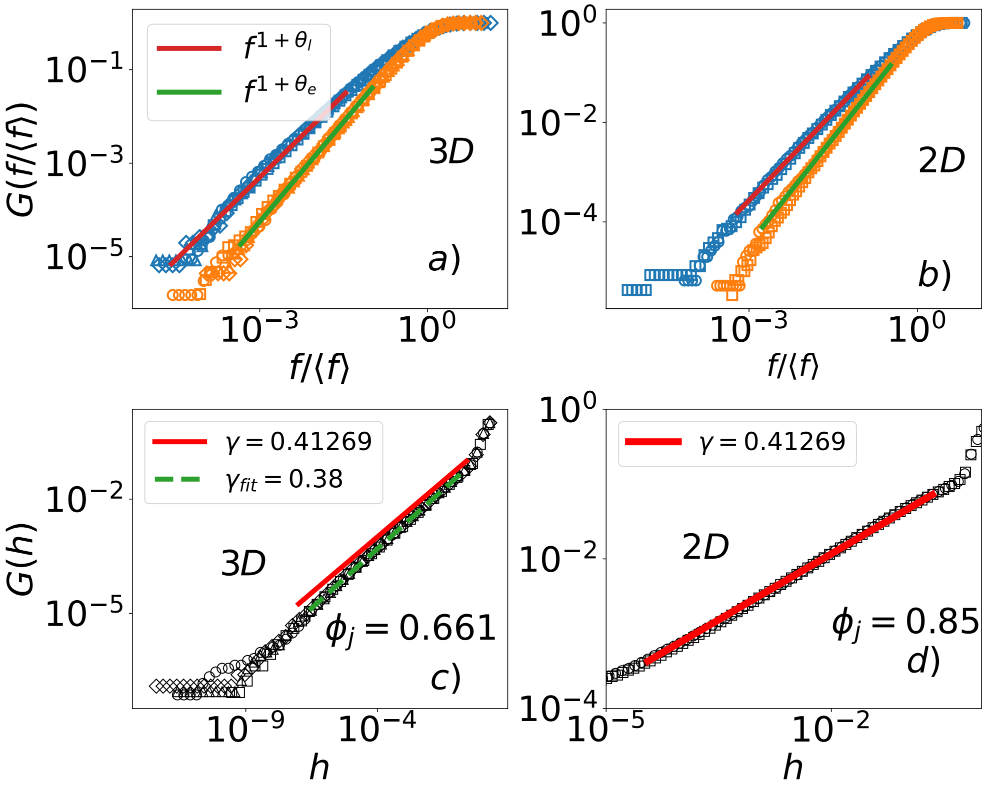

Figure 3.6: Inter-particle forces and gaps in shear jammed configurations and comparison with isotropically jammed configurations. All configurations analyzed have a single self-stressed state. Symbols $\Diamond, \bigcirc, \Box, \triangle$ represent isotropic compression,$\phi = 0.660, 0.658, 0.656$ respectively in $3D$ and symbols $\bigcirc, \Box$ represent $\phi = 0.8499, 0.8485$ in $2D$. **a)-b)** The cumulative distribution of forces $G(f/\langle f\rangle)$. The blue symbols represent localized forces and the orange symbols represent the extended forces. Comparison with exponents obtained from mean-field theory is shown. **c)-d)** The cumulative distribution of gaps h. The red line shows the exponent from mean field theory.

which carry small mechanically isolated forces. The mechanically isolated contacts are associated with “buckler" particles which are particles with $d + 1$ contacts. As shown in [24] the force distribution calculated by including only the bucklers, $P_l(f)$, exhibits an exponent of $\theta_l = 0.17462$. The force exponent calculated by using the distribution of the remaining forces is $P_e(f)$ shows an exponent of $\theta_e = 0.42311$. We follow the same procedure to analyse configurations with a single self-stressed state identified by $N_c = (N - 1)d + 1$. As opposed to isotropic jamming, for the shear jamming transition we need take into account the effect of shear while classifying bucklers. However, we observe that for configurations at small-strains, classification of bucklers as particles with $d + 1$ contacts is sufficient to obtain meaningful results. The cumulative probabilities of forces, separately for bucklers (localized modes) and the rest (extended modes), shown in Fig. 3.6 (a) and (b) for 3D and 2D, show that indeed, the predicted values of θ_e and θ_l describe the data extremely well.

3.3.3 Gap exponent

In Fig. 3.6 (c) and (d) we show the distribution of gaps for 3D and 2D. For 3D, while we find the mean field prediction of $\gamma = 0.41268\ldots$ closely describes the data, a value of $\gamma = 0.38$ is a better description of the data. Indeed, results in several works [22, 21, 93, 26], both for isotropic and shear jamming, are consistent with such a smaller exponent, which would correspond to a weak violation of the stability condition. However, the role of finite size effects in the observed departures at very small gaps has recently been investigated [26], emphasizing that finite size effects are much more pronounced for gaps rather than forces. A scaling collapse over several orders of magnitude supports the accuracy of the mean field exponent for three dimensional packings. Our analysis of finite size effects for shear jamming, shown in Fig. 3.8, clearly support the same conclusion. On the other hand, the results for 2D, shown in 3.6 (d) agree very well with the mean field predictions. Thus, we conclude that the marginal stability conditions (Eq. 3.9), which have been shown to be valid for isotropic jamming, *are* indeed also valid for shear jamming.

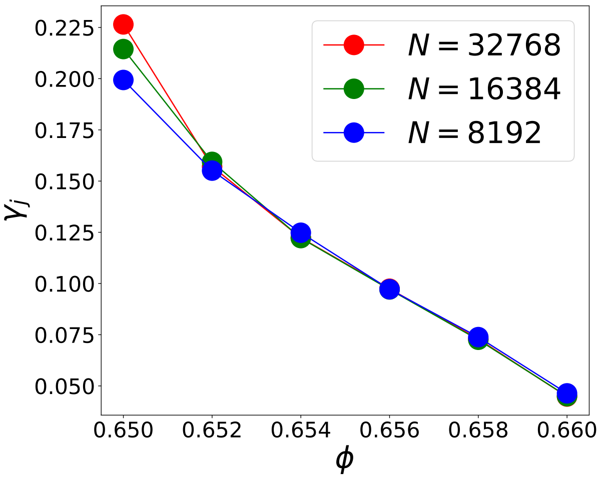

Figure 3.7: Dependence of γ_j on the density of the system ϕ shown for various system sizes.

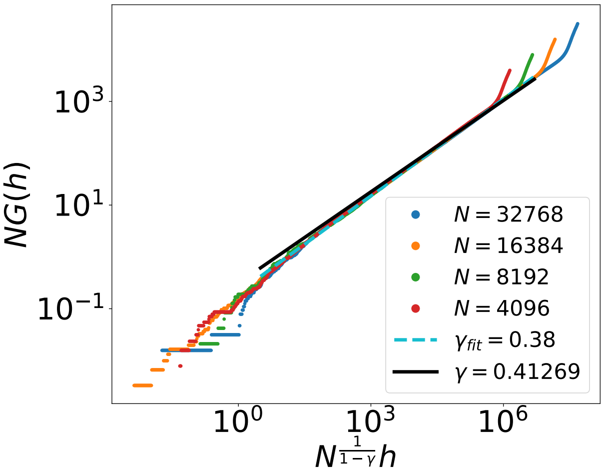

Figure 3.8: Finite size scaling of gap distribution $G(h)$ demonstrating that the mean field exponent of $\gamma = 0.41269$ convincingly fits the data in the region of data collapse. Also shown is a fit with $\gamma_{fit} = 0.38$ for comparison.

3.3.4 System size dependence of the jamming strain and finite size scaling of the gap distribution

The dependence of the jamming strain on the system size is shown in Fig. 3.7. Configurations at the isotropic jamming density $\phi_j \approx 0.66$ are generated for $N = 2^{12}, 2^{13}, 2^{14}, 2^{15}$ and are decompressed to densities such that $\phi_J < \phi < \phi_j$. These configurations are sheared uniformly to observe shear jamming at some strain $\gamma_j(\phi)$. Although we observe weak size dependence at the lowest densities, close to ϕ_J (as also in [93]), for most of the range of densities, we do not observe any significant size effects.

We analyze the gap distribution $G(h)$ obtained from different system sizes. We use the finite size scaling form given in [26] $c(h) \sim N^{-1}\tilde{c}(hN^{\frac{1}{1-\gamma}})$, employing the mean field value of the exponent γ. The results in Fig. 3.8 show convincing data collapse, with the data in the collapsed region being extremely well described by the mean field γ value. A smaller γ_{fit} value of 0.38 also describes the data reasonably well, but from the data collapse, one may conclude that such a fit is affected by the finite size deviations at small x values. We do not have an understanding of why the gap distribution has a more prominent size dependence compared to force distribution.

3.4 Conclusion

In summary, we have numerically analyzed configurations of soft spheres in two and three dimensions accurately generated at the shear jamming point, and above, for densities below the density ϕ_j at which they exhibit isotropic jamming, but above the minimum isotropic jamming density ϕ_J. We show that several quantities, such as the pressure P, the excess contact number, and a crossover frequency ω^* in the VDOS $D(\omega)$ exhibit critical scaling that is identical to that at the isotropic jamming point, with the shear stress in addition displaying the same scaling as the pressure. We confirm the behavior of the eigenvalues of the stiffness matrix which have been investigated [50] to argue that shear jamming has the same symmetry as isotropic jamming, and show that the rotation of the eigenvector of the largest eigenvalue in the shear strain direction is correlated with the anisotropy of the shear jammed structures. We show that the marginal stability condition is met for shear jamming to the same degree as for isotropic jamming, with exponents predicted by the mean field theory of the glass transition and jamming in hard spheres (although our results indicate that better finite size analysis is warranted for the gap distribution). Our results thus strongly support the idea that shear jamming displays the same critical behavior and marginal stability as isotropic jamming.

Chapter 4

Rigidity transition associated with shear jamming [1] [2]

---

[1] This work is done in collaboration with Dr. H.A Vinutha at Department of Physics, Institute for Soft Matter Synthesis and Metrology, Georgetown University, Washington, DC, USA and Prof. Dapeng Bi at Department of Physics, Northeastern University, MA 02115, USA.

[2] A preprint of this chapter can be found at https://arxiv.org/pdf/2301.12179.pdf.

4.1 Introduction

In the previous chapter we showed that shear jamming and isotropic jamming share many features of a continuous phase transition. Our results strongly support a unified description of isotropic and shear jamming.

In contrast, the manner in which the contact network acquires rigidity is strongly discontinuous [56] for frictionless isotropic jamming. At the jamming point, the entire system (barring a small percentage of *rattlers*, described later) acquires rigidity discontinuously. From the Maxwell criterion for the rigidity of networks of nodes connected by edges representing distance constraints, the contact network of a configuration with N particles in D dimensions can be rigid when contacts result in at least $N_c = D(N-1)$ constraints on the non- global degrees of freedom. In general, this is a necessary but not sufficient condition. Therefore, isotropic jamming occurs at the *isostatic point*, where the system has just the minimum number of contacts per particle, Z required, $Z_{iso} = 2D$ (from $\frac{NZ_{iso}}{2} = ND$)). This discontinuous rigidity transition is different from the continuous transition observed in random spring networks [107, 108] for which the rigid component of the system grows continuously beyond rigidity percolation, which does not occur at the isostatic point, and is preceded by the presence of both rigid and over-constrained regions.

Results available for shear jamming appear to suggest that the rigidity transition is continuous, in contrast to isotropic jamming[57, 58, 59, 55]. Computational investigation of the rigidity transition for frictional two dimensional ($2D$) systems sheared at finite rates [57] revealed a broad distribution of rigid cluster sizes with increasing mean size as the jamming transition is approached, supporting a continuous rigidity transition, although becoming “sharper” as the shear rate is lowered. Similar results have been recently reported from analysis of sheared granular packings in experiments [59]. Following the observation that sheared *frictionless packings* acquire geometric characteristics associated with jamming [52], the rigidity transition in such packings in $2D$ was analysed by including constraints associated with friction [55]. The size distribution of overconstrained clusters, similar to [57], exhibits a broad distribution, supporting a continuous rigidity transition. In addition, the rigidity transition associated with jamming in frictional systems was studied in lattice models of jamming where a continuous transition was observed except in a limiting case corresponding to infinite friction [58].

These observations suggest that the nature of the rigidity transition could be an exception to the commonality of isotropic and shear jamming phenomenology outlined earlier. In this chapter, we therefore investigate carefully the nature of the rigidity transition for both sheared frictional and frictionless packings, under both quasi-static and at finite shear rates. We find that the rigidity transition is unambiguously discontinuous under quasistatic shear. Such a transition appears rounded in the case of finite shear rate, but the dependence on shear rate clearly supports an approach to a discontinuous transition in the limit of vanishing shear rate.

4.2 Models and Methods

4.2.1 Frictionless shear jamming

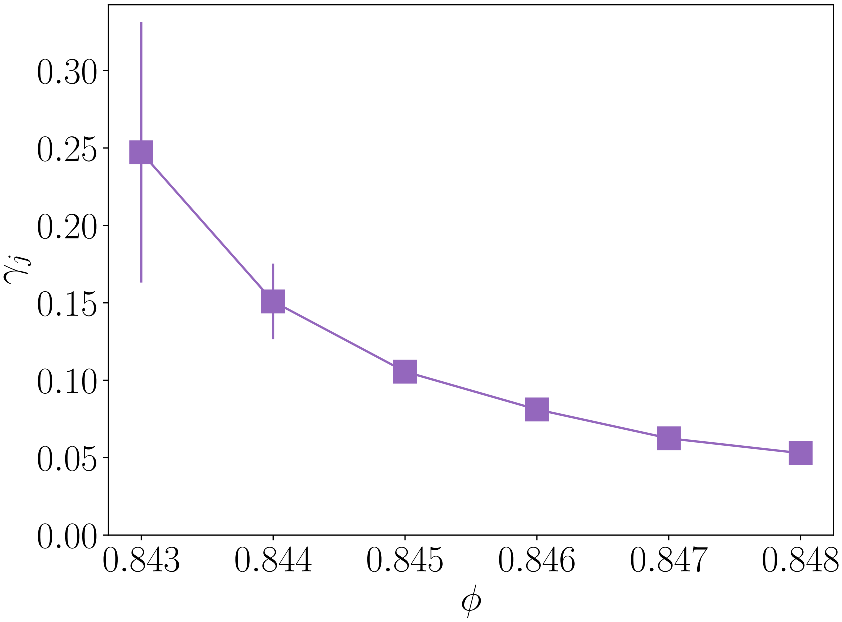

Figure 4.1: **Jamming strain γ_j vs ϕ for unjammed configurations above ϕ_J.**

We obtain shear jamming packings using the methodology described in the previous chapters which we describe briefly here. The packings are obtained by shearing unjammed soft-sphere configurations above the minimum jamming density ϕ_J. As descibed in [101, 109, 53, 54], well annealed disk-packings jam at a packing fraction higher than ϕ_J. For generating frictionless shear jamming configurations, we start by equilibrating hard-disk configurations at $\phi = 0.8$ using HOOMD [104]. These configurations are compressed quasi-statically using O'hern procedure [8] to generated jammed configurations at $\phi_j > \phi_J$, where $\phi_j \approx 0.85$ and $\phi_J \approx 0.84$. Configurations when decompressed to densities ϕ such that $\phi_j > \phi > \phi_J$ unjam. These unjammed configurations undergo shear jamming when subjected to AQS shear. We study a system of $N = 16384$ particles at a density of $\phi = 0.8485$. The results presented in this chapter are generated from 3 independent samples.

4.2.2 Discrete Element Method

We use Discrete Element Method (DEM) to simulate frictional disks introduced by Cundall and Strack [110] using LAMMPS [83]. In this system, soft-spheres interact using the linear and tangential spring dashpot model. The model includes damping in both normal and tangential directions, in addition to global viscous damping, helping the system reach force balance. The normal and tangential spring constants k_n and k_t is set to 2.0. The normal velocity damping η_n is set to 3.0 and the tangential damping η_t is set to $\frac{1}{2}\eta_n$. The global damping term η is also set to ≈ 3.

	k_n	K_t	$\Delta\gamma$	η_n	η_t	μ	η	dt	ρ_{disk}	σ_2/σ_1	ϕ	N
I	2.	2.	10^{-4}	3.	$\frac{1}{2}\eta_n$	1.	$\frac{m}{0.35}$	0.002	1.	1.4	0.81	16384
II	2.	2.	10^{-3}	3.	$\frac{1}{2}\eta_n$	1.	$\frac{m}{0.35}$	0.002	1.	1.4	0.81	2000
III	1.	1.	10^{-4}	0.1	$\frac{1}{2}\eta_n$	0.1	10m	0.002	1.	1.4	0.83	4096
IV	1.	1.	10^{-3}	0.1	$\frac{1}{2}\eta_n$	0.1	0.1m	0.002	1.	1.4	0.83	4096

Table 4.1: Values used in the simulations. The first column represents the different sets of simulations: I is for the $\mu = 1.0$ finite rate simulations described in the main draft. II is for the $\mu = 1.0$ quasi-static simulations described in the main draft. III is for the finite rate shear simulations for $\mu = 0.1$. IV is for the quasi-static shear simulations with $\mu = 0.1$.

Friction is implemented in the simulations as follows. Two particles are in contact when there is a finite overlap δ between them. This will result in a repulsive force between the particles which is modeled using a harmonic spring. One can also model it using a non-linear spring, then the interaction is Hertzian. Along with the repulsive spring, there is also a damping term that depends on the component of the relative velocity along the vector connecting the centers of the two springs. Therefore the repulsive force acting between two particles i and j is

$$\vec{F}_N = k_n \delta \mathbf{n}_{ij} - m_{eff} \eta_n \mathbf{v}_n \tag{4.1}$$

where k_n is the stiffness of the repulsive spring, η is the co-efficient of damping, δ is $\frac{\sigma_i+\sigma_j}{2} - |\mathbf{r}_{ij}|$, $\mathbf{n}_{ij}$ is the unit vector connecting the centers of the two disks in contact and $\mathbf{v}_n$ is the component of the relative velocity of the two disks along $\mathbf{n}_{ij}$, $\mathbf{v}_n = (\mathbf{v}_j - \mathbf{v}_i) \times \mathbf{n}_{ij}\mathbf{n}_{ij}$. The friction that acts between the particles is modeled using a tangential spring with a stiffness co-efficient k_t. In addition to the spring, there is also a damping term that depends on the relative tangential velocity just like the normal component. This contribution to the contact force is

$$\vec{F}_t = k_t \mathbf{\Delta s} - m_{eff} \eta_t \mathbf{v}_t \tag{4.2}$$

where $\mathbf{\Delta s}$ is the tangential displacement acquired during the existence of the contact and $\mathbf{v}_t$ is the tangential relative velocity. The tangential relative velocity is given by

$$\mathbf{v}_t = (\mathbf{v}_r - \mathbf{v}_n) - (R_i \Omega_i - R_j \Omega_j) \times \mathbf{n}_{ij} \tag{4.3}$$

where

$$\mathbf{v}_r = \mathbf{v}_i - \mathbf{v}_j \tag{4.4}$$

and Ω_i is the angular velocity of particle i. The tangential displacement is then calculated as

$$\mathbf{\Delta s} = \int_{t_0}^{t} \mathbf{v}_t dt. \tag{4.5}$$

We computing $\mathbf{\Delta s}$ we have to take care of the tumbling rotation of the pair in contact which changes the tangential plane, this is done by removing any component of the tangential displacement along $\mathbf{n}_{ij}$ and rescaling to preserve the magnitude [111]. Therefore the entire force acting between two particles is,

$$F_{ij} = (k_n \delta \mathbf{n}_{ij} - m_{eff}\eta_n \mathbf{v}_n) - (k_t \mathbf{\Delta s}_t + m_{eff}\eta_t \mathbf{v}_t). \tag{4.6}$$

With this force, one writes the equations of motion for the system

$$m_i \frac{d^2\mathbf{r}_i}{dt} = \sum_j \mathbf{F}_{ij} - \eta \mathbf{v}_i \tag{4.7}$$

$$I_i \frac{d\Omega_i}{dt} = \sum_j \mathbf{F}^t_{ij} R_i - \eta \Omega_i \tag{4.8}$$

where the η term represents a global damping term, for both translational and rotational motion. This helps the system reach force balance faster and can be thought of as arising from the friction of the granular material with the bottom plate of the experiment.

The time period of one-half oscillation of the linear spring dashpot model for the normal force is given by

$$t_c = \frac{\pi}{\omega}; \omega = \sqrt{(k_n/m_{12} - \gamma_0^2)} \tag{4.9}$$

where $\gamma_0 = \eta_n/m_{12}$ and $m_{12} = m_1 m_2/(m_1 + m_2)$. The timestep dt for DEM is chosen to be much less that t_c.

Finite rate and quasi-static shear of frictional systems

Shear is conducted by applying an affine transformation which increments the strain in the system by $\Delta\gamma$. This is followed by relaxation using the DEM. Because of the damping terms, the system will eventually settle into a force-balanced equilibrium configuration if one waits long enough. If we perform the dynamics till the system relaxes completely, then this procedure is quasi-static. In practice, we consider the system to have reached force/torque balance when the total force (sum of total forces acting on the disks) is less than 10^{-11} or when the total kinetic energy of the system is less than 10^{-19}. The simulation is stopped when the number of timesteps reaches 2×10^9 regardless. There is an apparent divergence in the timescale required to relax the system at the shear jamming transition as pointed out in [69] and thus it is difficult to achieve force-balance near the shear jamming transition. If one stops the relaxation after a predetermined set of steps then shear is conducted at a finite rate. For a given $\dot{\gamma}$ and $\Delta\gamma$, the time required for DEM relaxation before the affine transformation to achieve finite rate is $\Delta\gamma/\dot{\gamma}$. Therefore one has to perform DEM relaxation for $\Delta\gamma/(\dot{\gamma}dt)$ timesteps to achieve the finite rate. The dt we use in DEM simulations is 0.002.

We perform finite rate shear on a system size of $N = 16384$ particles, while the quasi-static simulations are done on $N = 2000$ particle system. We consider systems with $\mu = 0.1$ and $\mu = 1.0$. For $\mu = 1.0$, for finite rate shear results we use 10 samples at each $\dot{\gamma}$, except for the highest and lowest $\dot{\gamma}$ where we have used 20 samples and for the quasi-static case we have used 16 samples. For

$\mu = 0.1$, for finite rate shear results we have used 10 samples and 5 for quasi-static. The quasi-static simulation with $\mu = 1.0$ was performed by H.A Vinutha.

Generalized isostaticity

A major distinction between frictionless and frictional jamming is the isostatic contact number Z at which jamming can occur in the absence of redundant constraints, which has been shown to range from $D+1$ to $2D$ depending on the friction co-efficient μ [112, 35, 52, 55] with $Z_{iso} = D+1$ for $\mu = \infty$. This can be understood using the generalized isostaticity condition, obtained by considering additional conditions due to the "mobilized contacts"[112]. The tangential frictional force between two particles has an upper bound due to the Coulomb threshold: $f_t \leq \mu f_n$ and the mobilized contacts are those for which $\frac{f_t}{f_n} \approx \mu$. Considering a configuration with N particles and $n_m N$ mobilized contacts, the conditions that the contact network at jamming has to satisfy are DN force balance conditions, $\frac{D(D-1)}{2}N$ torque balance conditions, and $n_m N$ Coulomb conditions. The number of constraints imposed by the contacts is $\frac{NDZ}{2}$ (since each contact constrains one translational and $D-1$ rotational degrees of freedom). Z is by default computed excluding *rattlers* (particles with less than the minimum number of contacts necessary for local rigidity, $=3$ for frictionless, and 2 for frictional particles in 2D), and represented by Z_{NR} for clarity. Defining $Z_\mu = Z_{NR} - \frac{2n_m}{D}$, the generalized iso-staticity condition is

$$Z_\mu^{iso} = Z_{NR} - \frac{2n_m}{D} = D + 1. \tag{4.10}$$

For $2D$ networks arising in several contexts including jamming, the onset of rigidity has been analysed by employing the pebble game algorithm[107]. Each node of the network represents a disk in the present context and is assigned k pebbles ($k = 2$ for frictionless disks and $k = 3$ for frictional disks) representing the degrees of freedom. The constraints imposed by each contact are represented by 1 or 2 edges (2 for the frictional case, 1 for the frictionless case, as well as for a mobilised contact). A (k, l) pebble game ($l = 2$ indicates the global degrees of freedom) assigns pebbles recursively to edges, and based on such an assignment, decomposes the network into rigid clusters that are mutually floppy. Rigid clusters with redundant bonds (with no assigned pebbles) are termed over-constrained. A more detailed description of the algorithm is provided in the next section. We employ the pebble game to monitor the size of the largest rigid cluster in the system primarily, as well as the distribution of the size of rigid clusters.

4.2.3 Pebble game algorithm

As mentioned previously, the pebble game algorithm is an algorithm to check if a given 2D graph is rigid or not. If a graph is rigid, then the nodes of the graph cannot be moved without changing the length of the edges. Any such displacement of vertices such that the length of the edges does not change is called a floppy mode. In the context of jamming, the graph we analyze for rigidity is the contact network. The particle centers become the vertices of the graph, and each contact is represented by an edge in this graph. According to Laman's Theorem [113] a graph in $2D$ with N

sites and $2N-3$ edges is minimally rigid iff there exist no subgraph with n sites and more than $2n-3$ edges. A subgraph that violates this condition is called over-constrained. The pebble game is an algorithm to check if this condition is valid for a given graph. The pebble game starts with each vertex having $k=2$ pebbles indicating the degrees of freedom each vertex has and we try to cover every edge with a pebble indicating a degree of freedom lost in the system due to the edge following the rules of the pebble game which we describe below. The number of free pebbles (the ones that remain on the vertices) after the pebble game indicates the number of floppy modes the system has. We cannot constrain $l=3$ degrees of freedom as these are two global translations and a rotation. The original $(k=2, l=3)$ pebble game algorithm by [114] was extended to general (k,l) pebble game by Lee and Streinu [115] which we described below. We use $(k=2, l=2)$ pebble game for frictionless contact network and $(k=3, l=2)$ for frictional contact network. Since we use periodic boundary condition $l=2$ as the global rotation is not floppy mode.

- **Initialization**
    1. The pebble game starts with all vertices having k pebbles each and all edges are uncovered. Any site cannot have more than k pebbles at any time.
- **Assigning pebbles to bonds**
    1. Consider an edge E that connects vertices a and b.
    2. The rule for covering an edge is that the total number pebbles at its vertices is atleast $l+1$. Then use a pebble from a or b to cover E. The edge is now directed from $a(b)$ to $b(a)$ if a pebble of $a(b)$ is used (this pebble is now used to cover E and is not free).
- **Allowed pebble moves.**
    1. If the sites a and b together do not have $l+1$ free pebbles, then it means that pebbles are used to cover other edges connected to a or b.
    2. We can free a pebble at either sites by searching along the directed edges. Consider an edge E' that connects a and a' and a pebble of a is used to cover E'. If a' has a free pebble, then that pebble can be used to cover E' and the pebble that was covering E' can be freed. In doing so the direction of E' is reversed. If a' does not have a free pebble, then one can repeat the same process on the edges directed away from a' and try to free a pebble and so on. The process is repeated on all the edges directed away from a. Similarly at b. So that at the end of the directed search, we have $l+1$ free pebbles for covering E. Note that we can always free l pebbles because they are associated with global degrees of freedom.
- **Identifying independent and redundant bonds**
    1. All edges covered by pebbles are marked independent.

2. If we can't cover E after the pebble search, then E is marked a redundant bond, and all the sites visited in the failed directed search are over-constrained.
3. This process is repeated till all edges are either marked independent or redundant.

- **Rigid cluster decomposition.**
    1. We will assign a label to each independent edge such that all independent edges belonging to the same rigid cluster will have the same label.
    2. Consider an unlabeled independent bond E between a and b. We will assign a label to this edge to indicate the rigid cluster it belongs to. Currently, the cluster consists of only E.
    3. Using the directed search from the edges connected to a and b, we free l pebbles and bring them to sites a and b. These pebbles are now locked to E.
    4. We loop over all sites a' connected to a and b and see if we can free a pebble at a' using the directed search.
    5. If we can free a pebble at a' then this site is floppy with respect to E and so are all the sites visited during the search.
    6. If we cannot free a pebble at a' then this site is rigid with respect to E and so are all the sites visited during the search. We assign the label of E to all the edges connecting the rigid sites.
    7. We remove all identification of rigid and floppy and consider the next unlabeled edge.

At the end of this process, all independent bonds are assigned a label indicating the rigid cluster it belongs to. Therefore the system has been decomposed into rigid clusters which are mutually floppy. We have also identified the over-constrained regions. The number of free pebbles at the end of the process indicates the number of degrees of freedom the system has or the number of floppy modes.

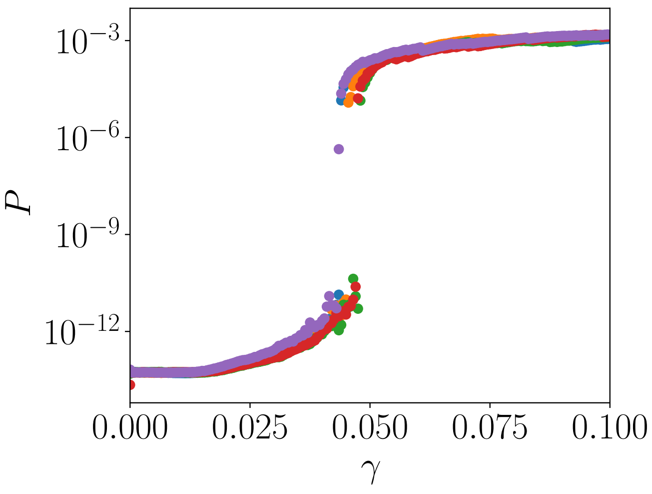

Figure 4.2: **Pressure as a function of strain γ for frictionless shear.** Shear jamming can be identified by the jump in pressure. Different colours indicate independent samples.

4.3 Results

4.3.1 Frictionless shear jamming

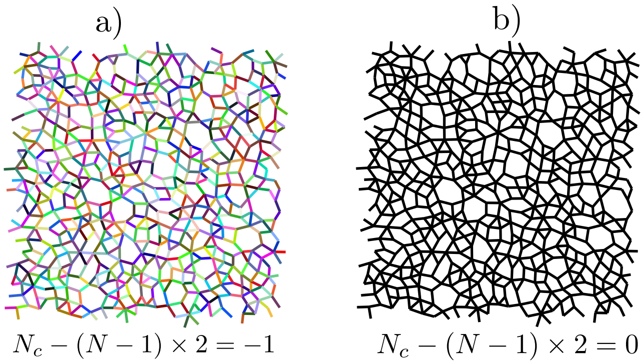

Figure 4.3: **Rigidity transition in sheared frictionless disk packings.** Pebble game analysis on the isostatic networks yields a single rigid cluster consisting of the whole system (**b**). Removal of one bond from that network results in a complete loss of rigidity, with the pebble game decomposing the system into multiple small rigid clusters indicated by the different colors (**a**)).

Jamming is identified in the frictionless system when energy minimization cannot remove all the overlaps in the system. This, therefore, results in finite forces in the system. These finite forces result in a finite pressure in the system, which can be used to identify jamming transition. Pressure as a function of strain for different independent configurations is shown in Fig. 4.2. As discussed in

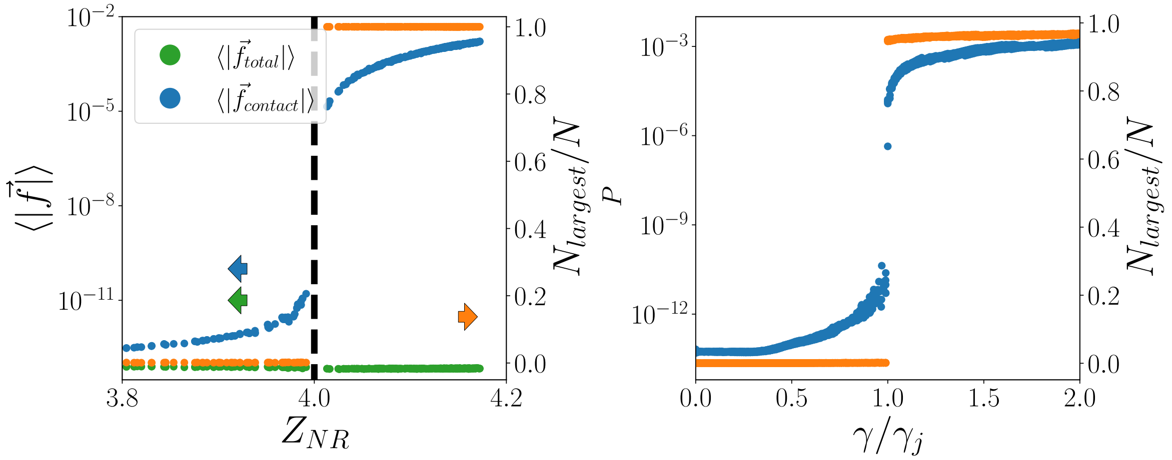

Figure 4.4: **Rigidity transition associated with shear jamming in frictionless systems.** The isostatic value in frictionless disks is 4; this is the point where jamming occurs. Z_{NR} is the non-rattler coordination number. For this analysis, we only consider jammed configurations. $N = 16384; \phi = 0.8485$. **b)** Rigidity transition as a function of γ. Rigidity transition coincides with the shear jamming transition. γ_j is the strain value where P crosses 10^{-9}.

[101, 109] at the point where this transition occurs the configuration is iso-static $Z_{NR} = Z_{iso} = 4 = 2d$. Note that the coordination number is calculated after recursively removing the rattlers. This strongly discontinuous rigidity transition is therefore common for frictionless isotropic and shear jamming.

We perform the rigidity analysis using ($k = 2, l = 2$) pebble game [114] ($l = 2$ because in systems with periodic boundary conditions there are only 2 global degrees of freedom). The results of this analysis are summarized in Fig. 4.4.

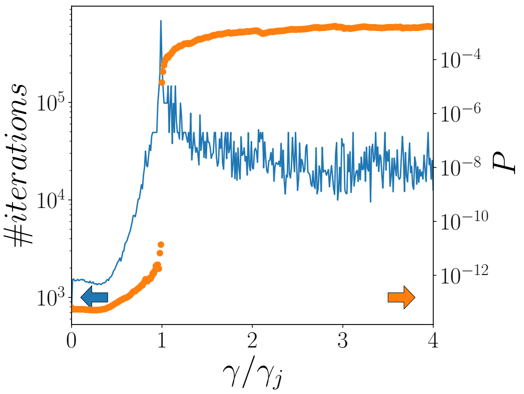

Figure 4.5: Apparent divergence in the number of iterations required. This is similar to the results observed by [69] for frictional shear jamming.

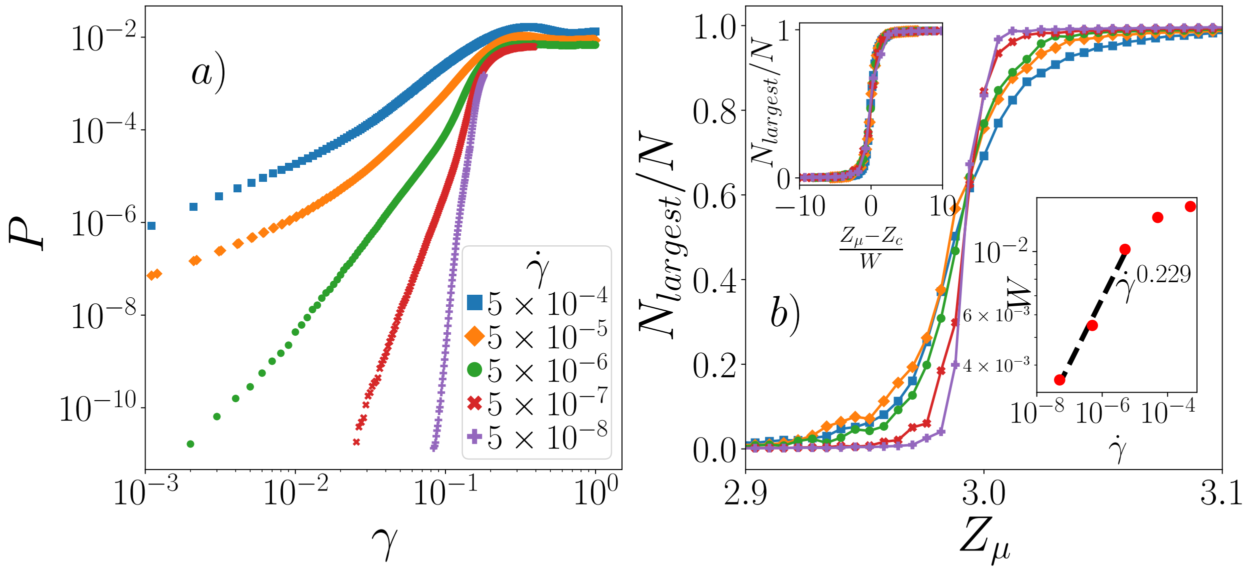

Figure 4.6: **Finite rate shear for $N = 16384$ with $\mu = 1$. a)** Shear stress σ_{xy} vs γ. **b)** Fraction of the largest rigid cluster with total number of particles as a function of $Z_m = Z_{NR} - n_m$ where Z_{NR} is the average co-ordination number calculated after recursively removing particles with one contact and n_m is the average number of mobilized contacts per particle (see text for details). As $\dot{\gamma}$ is reduced the transition becomes "sharper".

Frictionless shear jamming is also associated with a probable divergence in the iterations required by the conjugate gradient to reach a force-balance configuration. The plot of iterations required by CG vs strain γ is shown in Fig. 4.5.

4.3.2 Finite rate shear of frictional systems

Now, we discuss the results from finite rate shear of frictional systems. Shear is conducted at rates $\dot{\gamma}$'s with $\dot{\gamma} = 5 \times 10^{-4}, 5 \times 10^{-5}, 5 \times 10^{-6}, 5 \times 10^{-7}, 5 \times 10^{-8}$. The main observation from this set of simulations is that the rigidity transition associated with shear jamming becomes "sharper" or discontinuous as one reduces the shear rate: an observation also made in [57]. As shown in Fig. 4.6a, the increase in stress σ_{xy} is noticeably more pronounced for smaller shear rates.

To characterize the rigidity of these configurations we follow [57, 59, 55] and use $(k = 3, l = 2)$ pebble game on the contact network. Note that in the finite rate simulations, we do not simulate the system till it achieves force balance (unless force-balance occurs in the fixed time-steps required) and therefore for jammed as well as unjammed configurations, the forces in the system are finite. As shown in Fig. 4.7, pressure and stress in the system therefore do not show a drastic change while the system undergoes shear jamming.

In the graph (contact network) subjected to pebble game analysis, every mobilized contact represent one edge, while other contacts represent two edges as explained in [57, 59]. We use a

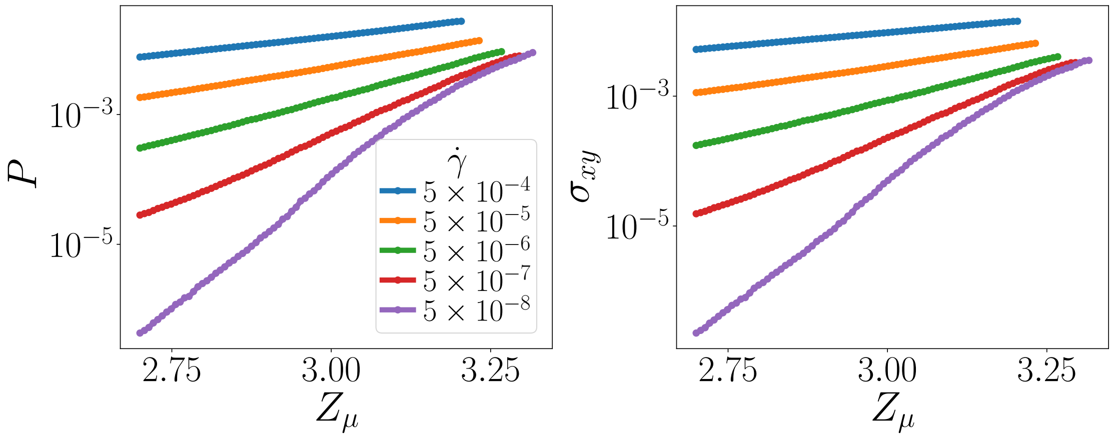

Figure 4.7: **LEFT** Pressure vs $Z_\mu = Z_{NR} - n_m$. **RIGHT** σ_{xy} vs Z_μ. For finite rate shear the jamming transition is not drastic in P and σ_{xy}.

threshold δ to identify mobilized contacts, - if $\frac{|\vec{f_t}|}{|\vec{f_n}|} > \mu - \delta$ then the contact is mobilized. Since in our simulations $\mu = 1$ and is a high value, very few of our contacts are sliding and the choice of δ is not very important. The value of δ used is 10^{-12} for most of the results with $\mu = 1.0$ unless specified otherwise. A discussion on the choice of δ for smaller μ is also presented. Even though the system is not in force balance when sheared at a finite rate, we identify rattlers as particles with just one contact and remove them recursively. Z_{NR} is the average co-ordination number of the remaining system. For the remaining contact network we perform pebble game analysis. The result of the pebble game analysis is shown in Fig. 4.6 (b) where the size of the largest rigid cluster is as the average contact number $Z_{NR} - n_m$ is varied. We define $Z_{NR} - n_m = Z_\mu$ for convenience. It is again clear that the transition becomes sharper as one reduces $\dot{\gamma}$. Interestingly the transition occurs at $Z_\mu \approx 3$ for all shear rates. We fit the data using the logistic function $f(x) = \left[1 + e^{-\frac{x - Z_c}{W}}\right]^{-1}$ (as a reasonable but arbitrary choice) and use W as a measure of the width of the transition region. As the top left inset in 4.6 (b) shows, the data can be collapsed using the fit values, with $Z_c \approx 2.99$. In the lower right inset, we show the behavior of W, whose dependence on $\dot{\gamma}$ can be described by a power law that implies that the transition becomes discontinuous at $\dot{\gamma} \to 0$. To our knowledge, this has not been reported for shear jamming transition.

We also show the rigidity analysis of configurations as a function of strain γ in Fig. 4.11. The strain at which rigidity transition occurs seems to have a non-monotonic dependence on $\dot{\gamma}$, a result we do not understand yet.

We also calculate P_∞, the probability that a given disk belongs to a rigid cluster spanning in both x and y directions. For this analysis, we consider the largest rigid cluster in the system and check if this cluster spans in both x and y direction. To do this, we consider the system along with 8 adjacent images. If the largest rigid cluster in the system does not span in either direction then when considered along with the images the number of clusters (when one considers only the

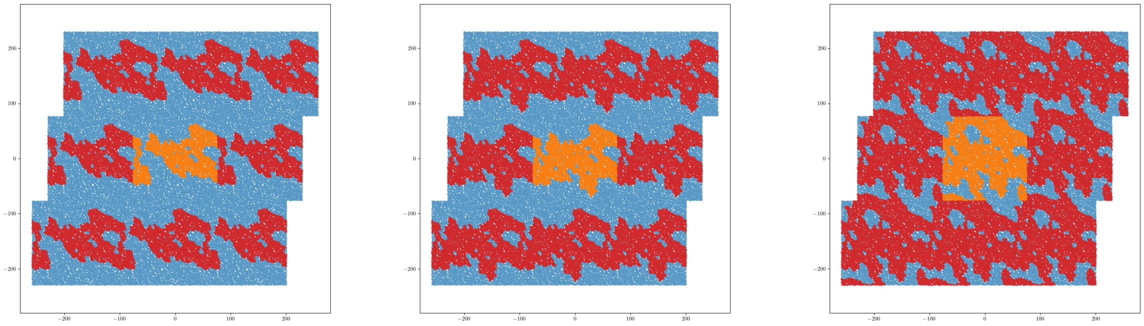

(a) Non percolating rigid cluster (b) Rigid cluster percolating in a single direction (c) System spanning rigid cluster

Figure 4.8: **Identifying a percolating cluster**. The red networks are the images of the rigid cluster, with the rigid cluster being the orange cluster in the middle.

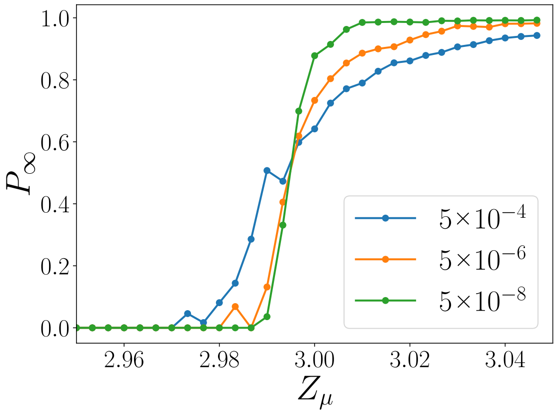

Figure 4.9: P_∞ **for three different shear rates.** The transition becomes sharper for lower shear rates.

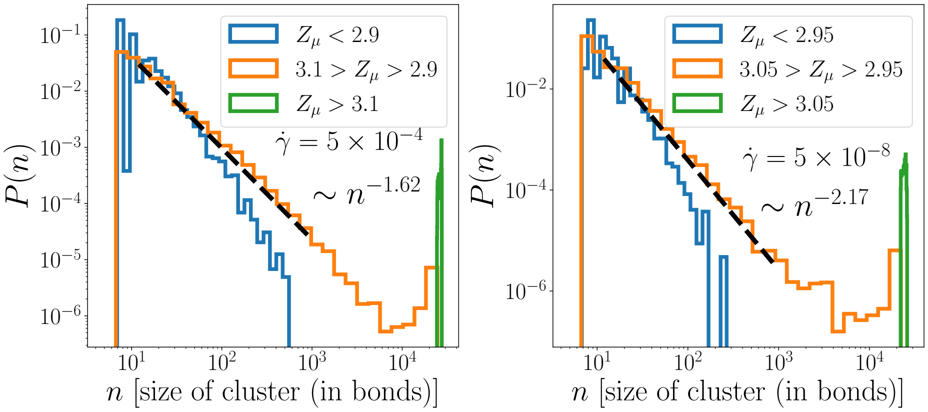

Figure 4.10: **Comparison of cluster size distribution between high and low $\dot{\gamma}$ studied. a)** $\dot{\gamma} = 5 \times 10^{-4}$ and **b)** $\dot{\gamma} = 5 \times 10^{-8}$. Both cases show the distribution of the size of rigid clusters for a range of Z_μ below 3 and a range covering 3 and for a range above 3. Comparing the distribution of cluster sizes for the range covering 3, we see that $\dot{\gamma} = 5 \times 10^{-4}$ shows a broader distribution compared to the one at $\dot{\gamma} = 5 \times 10^{-8}$ as quantified by the exponent characterizing the power law distribution, showing that the transition taking a discontinuous nature as one lowers the shear rate.

largest cluster) in the system will be 9. If the largest cluster spans only in one direction, then when considered along with images, the number of clusters will be 3. In the case of the largest cluster spanning both directions, the number of clusters will be 1. For each strained sample we identify the rigid cluster which spans in both directions and compute $P_\infty = N_{largest}/N$. The result of this analysis is shown in Fig. 4.9. This shows that for finite shear rates, the transition is continuous although it gets sharper as one reduces the shear rate.

Next, we study the cluster size distribution as shown in Fig. 4.10 shown for the largest and the smallest $\dot{\gamma}$ studied. For both cases, we divide the region studied (in Z_μ) into three regimes - before jamming transition, a regime covering the transition, and after the transition and the distribution of the rigid cluster sizes is computed separately for each of them. The distributions in the regime covering the transition are quantified by an exponent characterizing the powerlaw distribution of the rigid clusters. For $\dot{\gamma} = 5 \times 10^{-4}$, the exponent is -1.62 and for $\dot{\gamma} = 5 \times 10^{-8}$, the exponent is 2.17. While the transition is of continuous nature for both the shear rates studied, the transition tends to become sharper as one reduces the shear rate. This along with the results from quasi-static shear show clearly how the nature of the rigidity transition changes as $\dot{\gamma} \to 0$.

We also present related results on the choice of the threshold δ used to determine mobilized contacts and the behavior n_m. As shown in Fig. 4.12, changing the threshold from $\delta = 10^{-6}$ to $\delta = 10^{-12}$ does not qualitatively affect the rigidity transition for the shear rates considered. However, as shown in Fig. 4.13, the behavior of n_m is affected by the choice of δ.

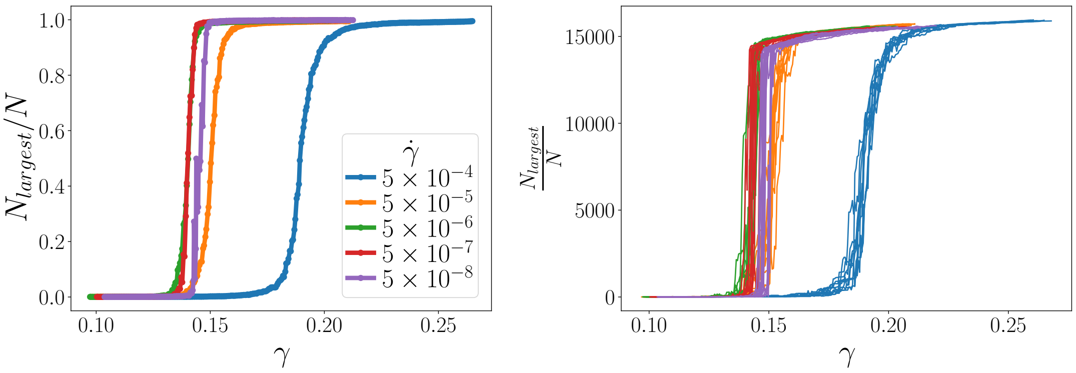

Figure 4.11: Size of the largest cluster with respect to γ. **LEFT** Averaged over samples. **RIGHT** Individual samples. We do not have an understanding of why the jamming strain depends on shear rate in a non-monotonic manner. We can possibly attribute this to the non-standard way in which finite shear rate is implemented in this work. Further investigation using the standard method is needed.

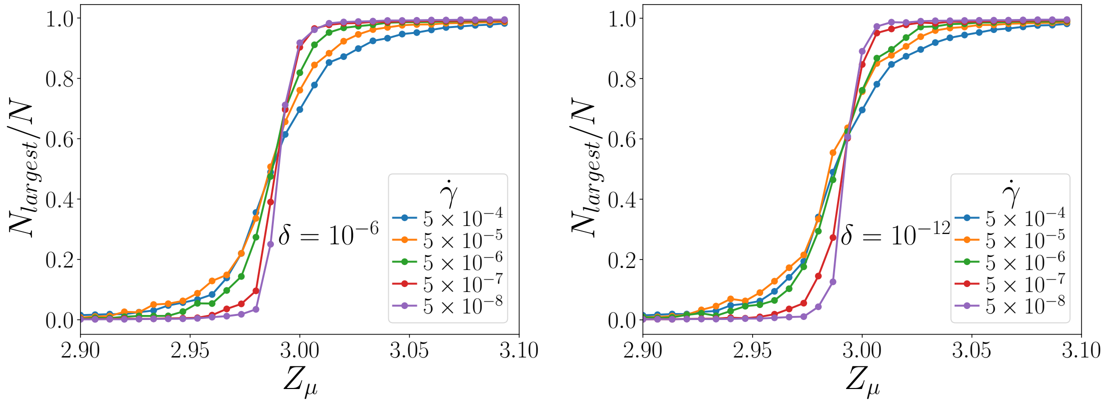

Figure 4.12: Size of the largest cluster with respect to Z_μ for different values of the threshold δ for identifying mobilized contacts. **LEFT** $\delta = 10^{-6}$.**RIGHT** $\delta = 10^{-12}$. The behavior of n_m as the threshold is changed is not understood. The choice of threshold to identify n_m is not clear and further investigation is required.

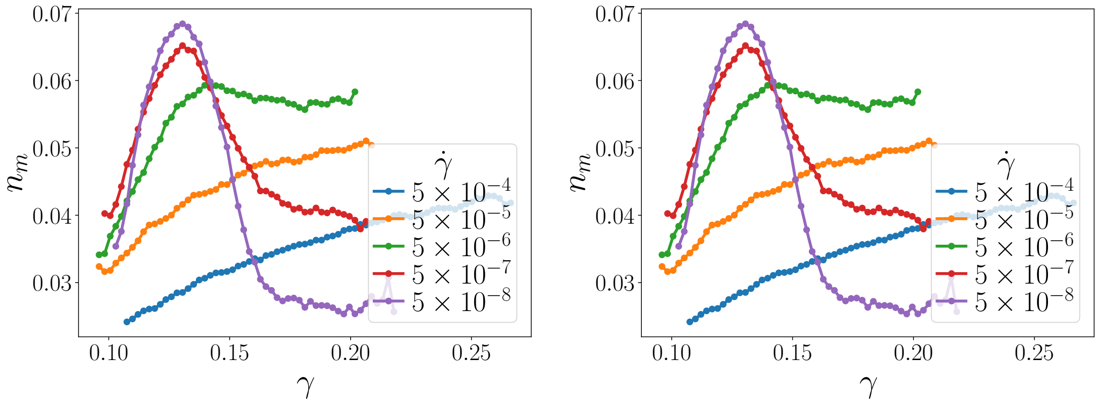

Figure 4.13: n_m vs γ for different values of the threshold δ for identifying mobilized contacts. **LEFT** $\delta = 10^{-6}$.**RIGHT** $\delta = 10^{-12}$.

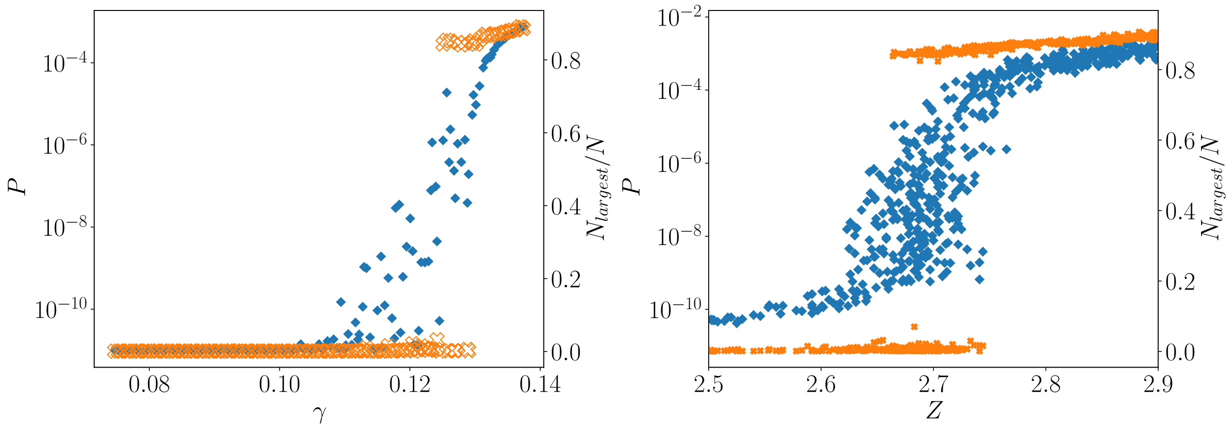

Figure 4.14: **Rigidity analysis of configurations undergoing quasi-static shear. LEFT** The pressure P (diamonds) and the size of the largest cluster (crosses) is plotted against γ for a single sample. This shows that the rigidity transition is abrupt and coincides with the shear jamming transition similar to the scenario in frictionless shear jamming. **RIGHT** The same data is plotted against Z, the average co-ordination number before removing any rattlers. This shows that the transition occurs at $Z \approx 2.7$.

4.3.3 Quasi-static shear of frictional systems

Quasi-static shear deformation of frictional systems is done by applying the affine transformation and relaxing the system using DEM till the system reaches force balance. As noted before the relaxation near the jamming transition is very slow and therefore it is hard to generate force-balance solutions near the jamming transition. Therefore the discussion is limited to $N = 2000$ system size. We analyzed the configurations obtained through DEM relaxation using $(k = 3, l = 2)$ pebble game, and the results are shown in Fig. 4.14. The rigidity transition for the quasi-static shear is abrupt, with a rigid cluster that consists on the majority of the system appearing instantaneously. This transition also coincides with the jamming transition as identified by a jump in P.

Given configurations that are fully relaxed, we define rattlers as particles that do not have finite forces acting on them. Particles with a single contact cannot sustain a non-zero force on that contact. So we remove these single contacts recursively. In addition, given a friction co-efficient μ, particles with two contacts can be in force balance with finite forces if the angle between the two contacts is large enough. If the angle between the two contacts is θ then if $\mu < \tan(\frac{\pi}{2} - \frac{\theta}{2})$ then these contacts cannot carry forces (Discussed in detail later in the chapter). So we remove these contacts as well recursively.

Given the inadequate force-balance at the transition, we use the following protocol to identify the load carrying mechanical forces [69] - non mechanical contacts are defined as $\frac{|\vec{f}^{ij}_{contact}|}{|\vec{f}^{i}_{total}|} < 10^2$. However, this procedure is not necessary to understand the rigidity transition.

The configurations after removing rattlers are analyzed using $(k = 3, l = 2)$ pebble game, and the results are shown in Fig. 4.16 when we consider only geometric rattlers, Fig. 4.15 when we

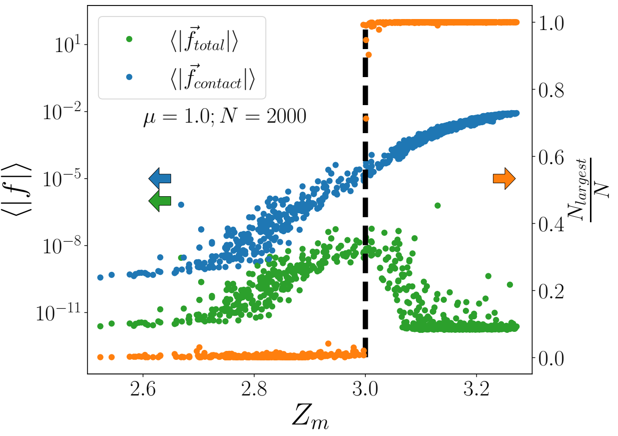

Figure 4.15: **Rigidity analysis of quasi-statically shear jammed frictional disks** with removing non-mechanical contacts. The size of the largest rigid cluster discontinuously jumps to approximately the system size as $Z_{NR} - n_m$ crosses 3, the iso-static value. The transition is contact forces is more smeared out in this case because we selectively remove small forces when we remove non-mechanical forces. The presence of finite forces, while the system does not have a spanning rigid cluster, is likely an artifact due to the fact that force-balance of these configurations is not adequate as timescales diverge at the transition.

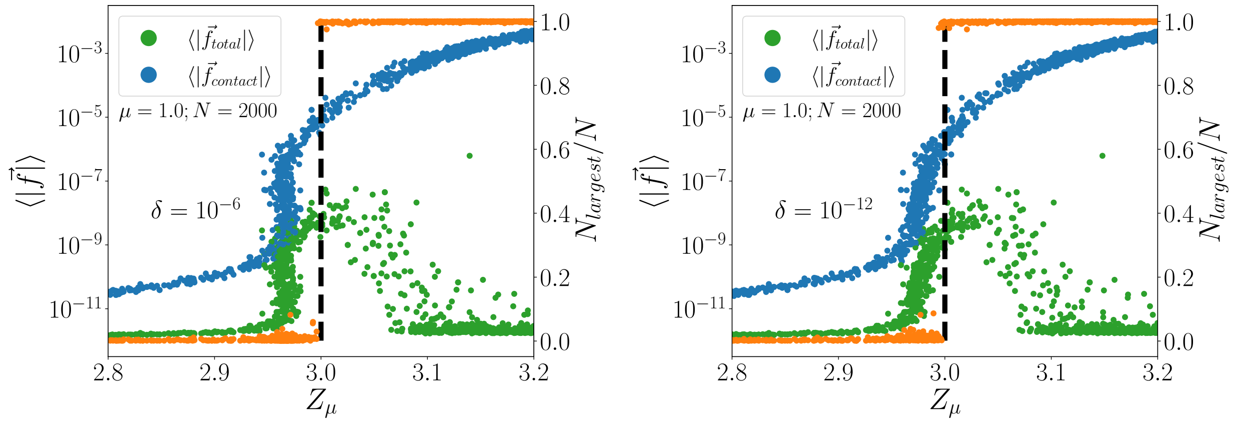

Figure 4.16: **Rigidity transition for quasi-static shear without removing rattlers LEFT** For $\delta = 10^{-6}$. **RIGHT** For $\delta = 10^{-12}$. The rigidity transition is abrupt and approximately coincides with the shear jamming transition as identified from the contact forces. Since the choice of n_m affects the number of constraints in the system, it affects where we observe rigidity transition in the system and its proximity to the shear jamming transition.

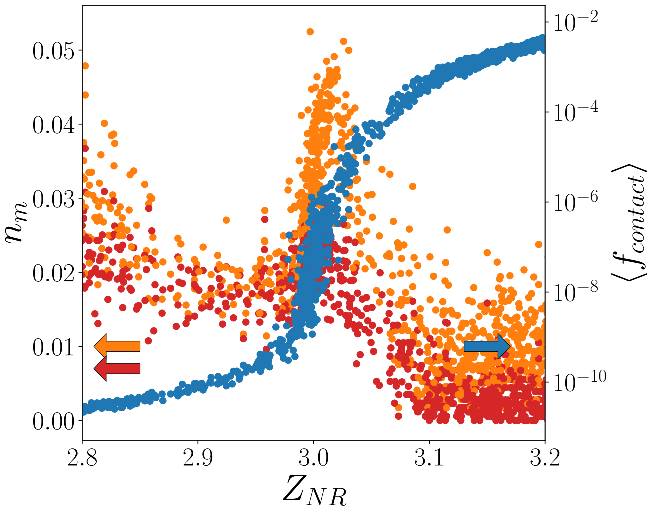

Figure 4.17: **Fraction of mobilized/sliding contacts and forces as a function of Z_{NR}.** Z_{NR} calculated without removing non-mechanical contacts. $\delta = 10^{-6}$ for the orange data points and $\delta = 10^{-12}$ for the red data points.

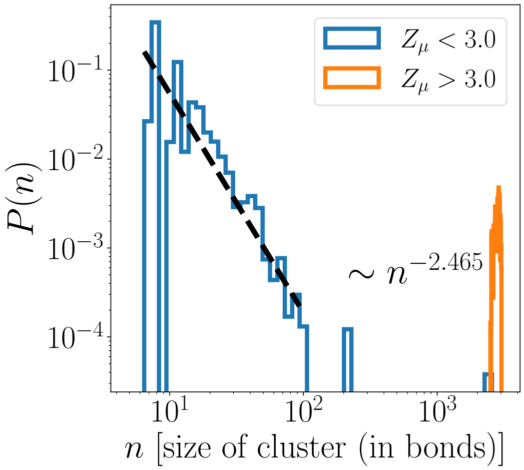

Figure 4.18: **Distribution of rigid cluster sizes for quasi-static shear.** The distribution clearly shows a gap, which is reflective of the abrupt transition.

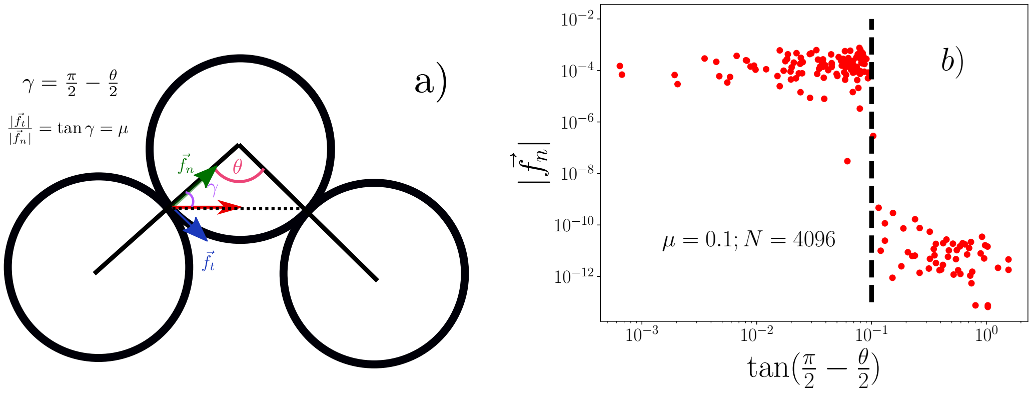

Figure 4.19: **Minimum contact angle required for force-balance. a)** The schematic shows a particle with two contacts with an angle θ between the contacts. The red arrow, green and blue arrows depict the total, normal and tangential force at the contact respectively. For the central particle to be force-balance the total contact force (red arrow) should be along the dotted line depicted. Therefore the angle between the total contact force and the normal force should be $\gamma = \frac{\pi}{2} - \frac{\theta}{2}$. However, the maximum angle between the total contact force and the normal force is constrained by the Coulomb condition $\frac{|\vec{f}_t|}{|\vec{f}|_n} = \mu$. Therefore the minimum angle θ such that the central particle can be in force-balance with finite forces is such that $\mu < \tan(\frac{\pi}{2} - \frac{\theta}{2})$. **b)** Normal force magnitude (for a contact) as a function of the angle between contacts for particles with two contacts shown for a single configuration with $\mu = 0.1$. This shows that when the condition $\mu < \tan(\frac{\pi}{2} - \frac{\theta}{2})$ is crossed, there cannot be finite forces along the contacts.

remove non-mechanical contacts also recursively. As shown in the figure, as Z_μ crosses isostatic value 3, a rigid cluster consisting of the whole system appears. The rigidity transition provides an approximate identification of the shear jamming transition, however from the definition of Z_μ the number of mobilized contacts n_m affects the quality of this identification. Given that the pebble game is a constraint counting algorithm, the transition always occurs at $Z_\mu = 3$, however, this value could be slightly different from where the transition occurs as seen from contact forces. We see that choice of a smaller threshold δ for the identification of mobilized contacts gives better identification. The behavior of n_m for quasi-static shear is shown in Fig. 4.17. We also compute the distribution of the rigid cluster sizes and the results are shown in Fig. 4.18. The distribution below jamming shows a larger exponent of ≈ 2.5 compared to the finite shear rate and in addition, also shows a gap.

These results resemble a striking similarity with the behavior of the frictionless system as shown in Fig. 4.4.

As mentioned earlier, our results are consistent with the results of [57] as reducing the shear rate results in a sharper rigidity transition. We in addition study quasi-static shear as well where rigidity transition is found to be discontinuous. Since at the rigidity transition, the largest rigid cluster is practically the whole system, the behavior of P_∞ is similar to $N_{largest}/N$.

4.3.4 Identifying rattlers

Given configurations in force balance, we can remove rattlers. We recursively remove all particles with just one contact as those contacts cannot carry forces. In addition, we recursively remove all particles with two contacts such that the angle between the two contacts θ satisfies $\mu < \tan(\frac{\pi}{2} - \frac{\theta}{2})$. This is the minimum angle between two contacts such that the particle is in force-balance as shown in Fig. 4.19 with finite forces. Z_{NR} is the average coordination number of the remaining system.

4.3.5 Over-constrained networks and floppy modes in frictional and frictionless shear

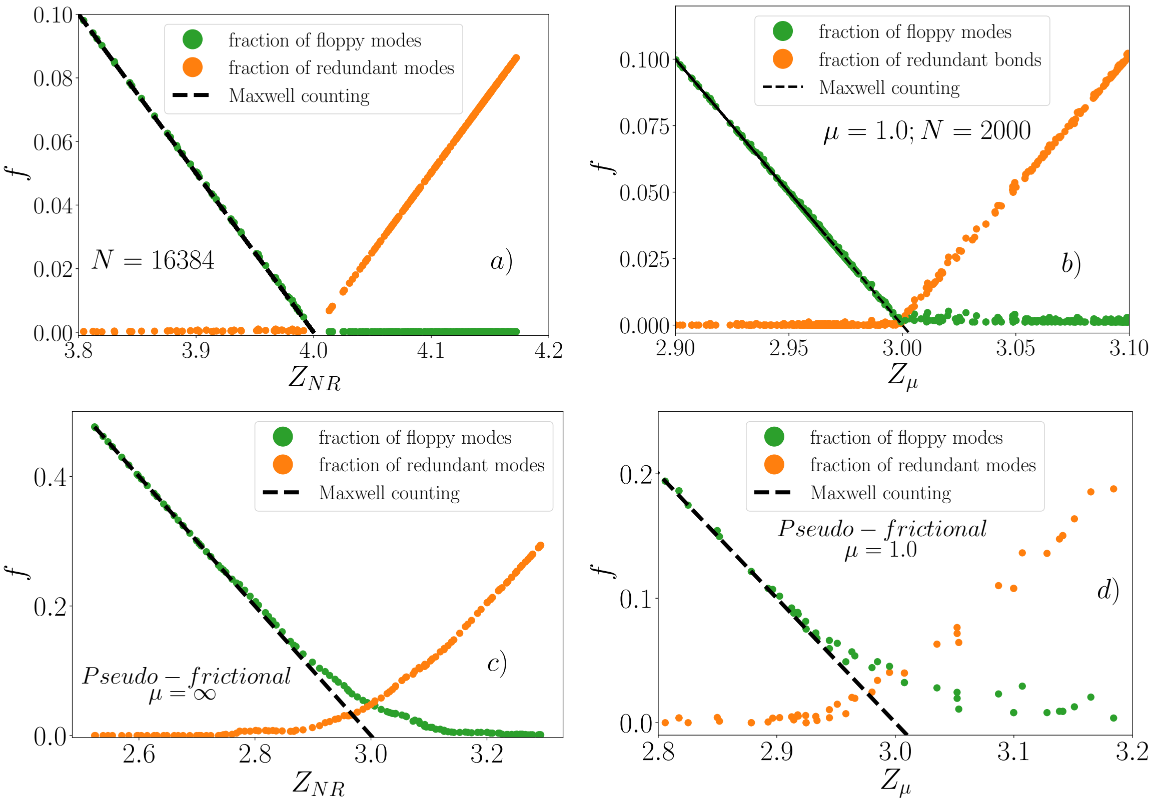

Figure 4.20: **Fraction of redundant contacts and floppy modes in frictionless and frictional systems under shear. a)** Frictionless systems. **b)** Frictional system with $\mu = 1.0$. For both systems, redundant bonds do not appear until the jamming transition. Also once rattlers are removed, there are no floppy modes after jamming. Due to these reasons, Maxwell's counting correctly identifies the jamming and the rigidity transition. **c)** Redundant bonds and floppy modes in pseudo-frictional case analyzed in [55]. **d)** Pseudo-frictional case with finite friction coefficient $\mu = 1.0$.

Here we highlight interesting differences in the rigidity transition in jamming from the rigidity transition in other networks. For rigidity percolation studies in bond-diluted lattice systems, redundant bonds exist inside non-percolating rigid clusters alongside floppy modes in the system [114]. This is in contrast to jamming in frictionless and frictional disk packings, where redundant bonds do not appear in the system until the jamming transition where a percolating rigid cluster emerges which comprises the whole system. In addition, floppy modes are not present in the system after jamming, provided that rattlers are removed. This is why Maxwell counting gives a very good identification of jamming transition since all bonds added are independent until jamming. These results are summarised in Fig. 4.20. We observe that the procedure followed in [55] does not capture this feature of jamming as shown in Fig. 4.20 (c) and (d).

4.3.6 Rigidity transition for system with $\mu = 0.1$

Finite rate shear

Finite rate shear simulations are performed at three different rates: $\dot{\gamma} = 5 \times 10^{-4}, 5 \times 10^{-6}, 5 \times 10^{-8}$ for a system of $N = 4096$ particles. The behavior of the $\mu = 0.1$ system when $\dot{\gamma}$ is lowered is similar to what is observed for $\mu = 1.0$. Noticeably the transition occurs around $Z_\mu = 3.0$. The packing fraction ϕ studied here is $\phi = 0.83$.

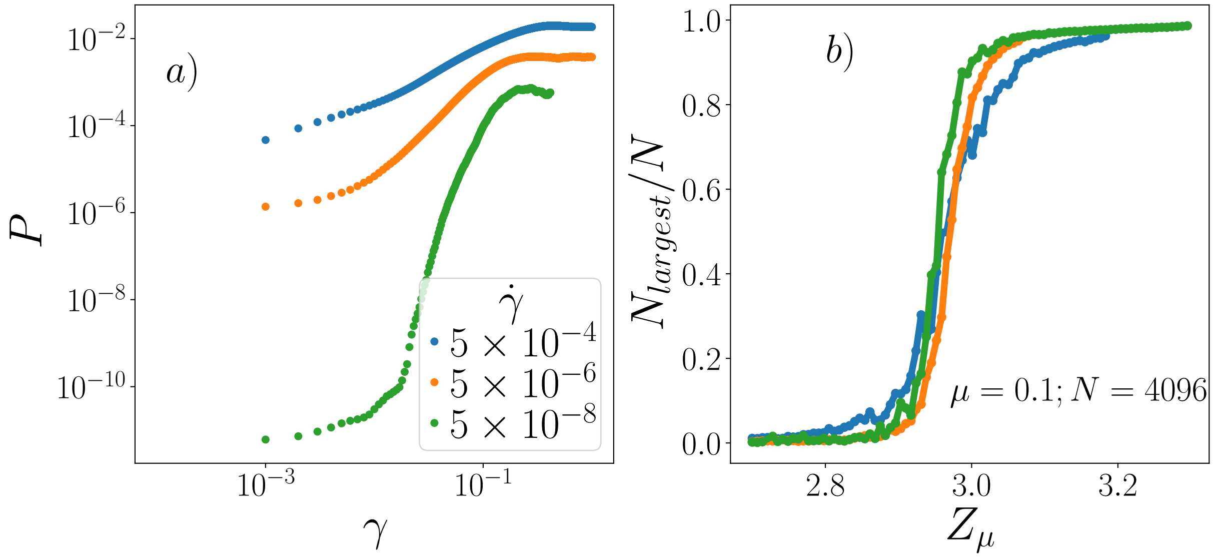

Figure 4.21: **Results for** $\mu = 0.1$. **a)** Evolution of stress σ_{xy} is similar to that of the high friction case. **b)** The transition for $\mu = 0.1$ does get sharper as one lowers the shear rate. however, is less pronounced than how it is for $\mu = 1.0$. In addition, the transition seems to occur before the isostatic value $Z_{NR} - n_m = 3.0$. The number of mobilized contacts n_m is computed as number of contacts having $\frac{|\vec{f}_t|}{|\vec{f}_n|} > \mu - 10^{-8}$ per particle. As described in the main text, for the pebble game analysis we remove all particles with one contact.

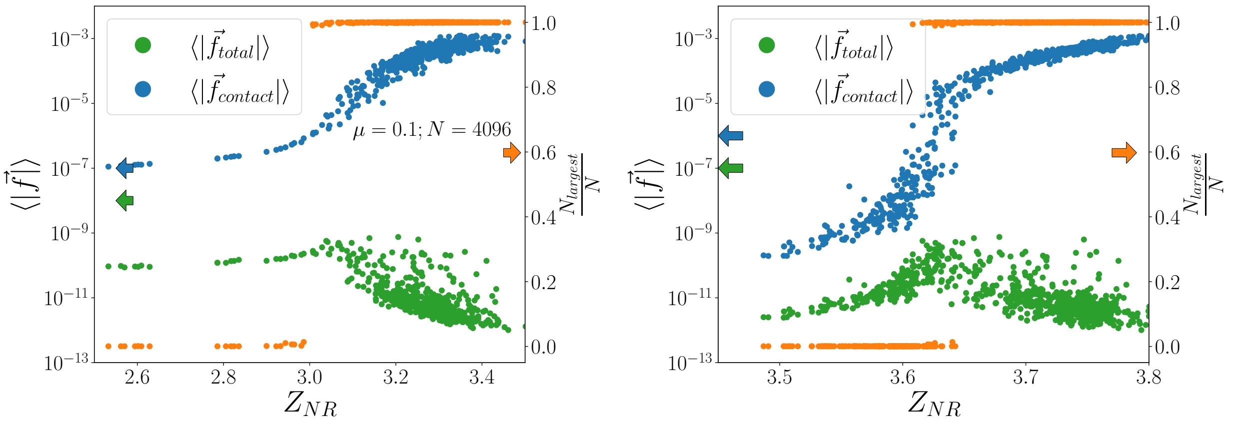

Figure 4.22: **Result of pebble game analysis for $\mu = 0.1$. LEFT** This results show that for quasi-statically sheared systems the emergence of a rigid cluster in the system is instantaneous, as shown in the main text for $\mu = 1$. The number of mobilized contacts n_m is computed as number of contacts having $\frac{|\vec{f}_t|}{|\vec{f}_n|} > \mu - 10^{-8}$ per particle **RIGHT** Same data shown without subtracting n_m from the Z_{NR}. In identifying mobilized contacts we have also included contacts for which $|\vec{f}_n| < 10^{-7}$ as these contacts are assumed to be sliding as well. (See discussion on mobilized contacts)

Quasi-static shear

Here we discuss the associated results when shear simulations are performed quasi-statically for $\mu = 0.1$. Here we change the constant associated with global damping to a smaller number $\eta = 0.1$ as mentioned in Table. 4.1. These give us better force-balanced configurations because simulations with a higher value of η have significant viscous forces which contribute to the force balance of the particles. Using a lower η reduces the effect of the viscous forces since we are interested in mechanical force balance. Rattlers are removed recursively and this contact network is analyzed using the pebble game algorithm with the results shown in Fig. 4.22. In this case, as well, the transition is correctly identified by Z_μ crossing 3. Fig. 4.22 also shows that the rigidity transition occurs abruptly with the rigid percolating cluster.

4.3.7 Determining mobilized contacts

Here we show how the threshold to identify mobilized contacts is calculated in different scenarios. As discussed in the main text, a contact is considered mobilized if $\frac{|\vec{f}_t|}{|\vec{f}_n|} > \mu - \delta$ where δ is the threshold. In this section, we show the effect of δ on our results. For the high friction case considered ($\mu = 1.0$), the number of mobilized contacts is low as shown in previous works [35, 57, 112]. Therefore the effect of the choice of the threshold is more pronounced for the $\mu = 0.1$ where the number of mobilized contacts is significant. Choice of δ affects the results of pebble game as the number of edges in the graph analyzed depends on δ. Choosing a larger δ results in fewer edges in the graph as we replace each sliding contact with a single edge and others with a double edge. Therefore it is “easier” for the pebble game to detect a rigid cluster for a smaller value of δ and otherwise.

We confine the discussion of identifying mobilized contacts to just the quasi-static case. In the case of quasi-static shear, we can unambiguously detect the shear jamming transition from the presence of the finite force contact network. The correct δ should therefore detect the rigid or over-constrained network at the strain value where finite forces exist. As we show this happens only at an intermediate value of δ. A related point that needs to be discussed is how finite forces are identified given the limitations of the numerical procedure used. For unjammed configurations as well, the DEM relaxation method does not completely remove the overlaps such that the forces are numerically zero. Instead as can be seen in Fig. 4.19 (b), one can categorize forces into finite and non-finite depending on the magnitude. Therefore we consider $|\vec{f}_{contact}| \geq 10^{-7}$ to be finite forces. For weak contact forces mobilization cannot be meaningfully computed.

We consider shear jamming of a single sample with $\mu = 0.1$ (Fig. 4.23 (a) and (b)) and $\mu = 1.0$ (Fig. 4.23 (c)). As shown in Fig. 4.23 (a), the transition to finite forces is correctly identified by $\delta = 10^{-3}, 10^{-6}$, while $\delta = 10^{-6}, 10^{-8}$ detects a rigidity transition at an earlier strain. We consider this first transition to be spurious and an artifact of inadequate numerical relaxation as the forces do not undergo a transition at this strain. The rigidity transition associated with the occurrence of finite forces in the system is discontinuous. To circumvent this issue we identify contact forces with $|\vec{f}_n| < 10^{-7}$ to be sliding contacts as these particles can be considered to be weakly in touch. We choose $\delta = 10^{-8}$ for analysis of configurations with $\mu = 0.1$ and $\delta = 10^{-12}$ for configurations with $\mu = 1.0$. We also show the distribution of contact mobilization for the quasi-static case in Fig. 4.24 and Fig. 4.25.

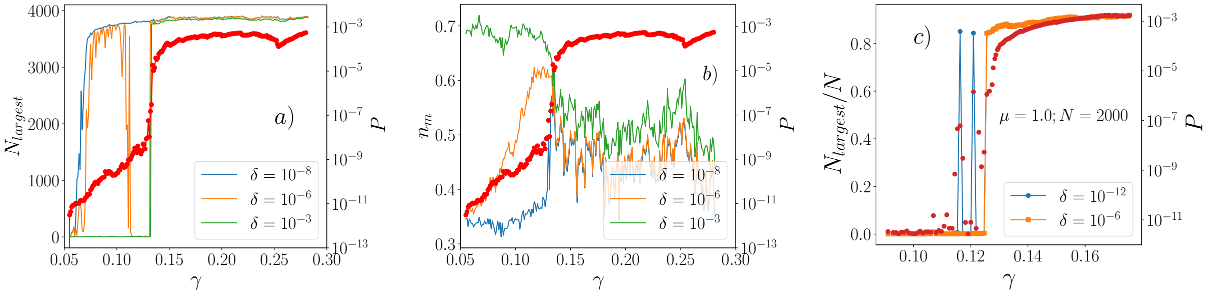

Figure 4.23: **Rigidity transition associated with shear jamming for different δ, where δ is the threshold for identifying mobilized contacts**. **a)** If we consider the presence of finite forces to be where shear jamming transition occurs with finite forces being defined as $P > 10^{-7}$, then $\delta = 10^{-3}, 10^{-6}$ detects a rigidity transition correctly. As explained in the text, $\delta = 10^{-8}$ detects a transition much earlier. We consider the rigidity transition detected by $\delta = 10^{-6}, 10^{-8}$ in the strain interval $[0.05, 0.1]$ to be spurious and an artifact of inadequate numerical relaxation. **b)** The fraction of mobilized contacts n_m for the corresponding sample. The difference is the number of mobilized contacts is most pronounced before the jamming transition and a high value n_m corresponds to floppy regions with no system spanning rigid cluster **a)** and **b)** Show a single sample with $\mu = 0.1$. **c)** Dependence of rigidity transition on the choice of δ for $\mu = 1.0$ quasi-static shear. Given that the number of mobilized contacts is very small for high friction, the choice of δ does not make a significant difference

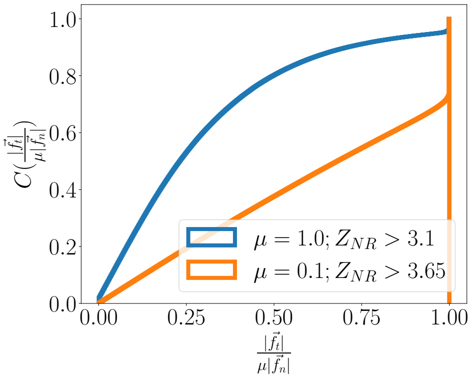

Figure 4.24: **Cumulative distribution of mobilization** $m = \frac{|\vec{f}_t|}{\mu|\vec{f}_n|}$ **for steady state configurations for** $\mu = 1.0$ **and** $\mu = 0.1$ **quasi-static shear.** For $\mu = 1.0$ the number of mobilized contacts is low compared to $\mu = 0.1$.

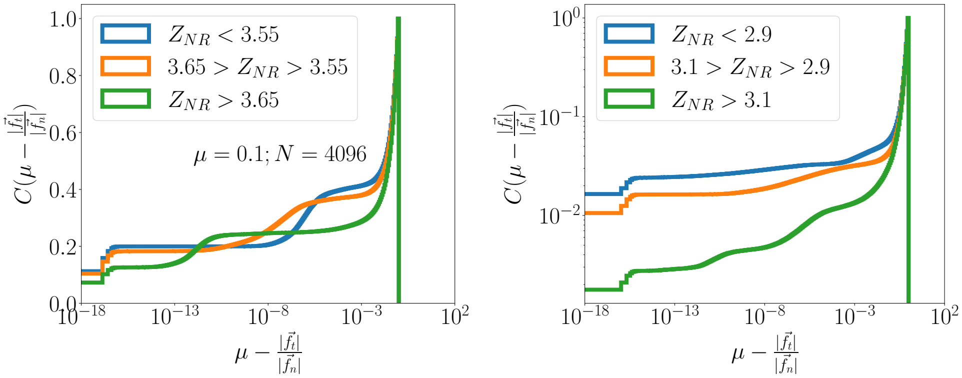

Figure 4.25: **Distribution of contact forces near the Coulomb threshold for quasi-static shear.** The number of contacts near the mobilization change as the system undergoes a shear jamming transition. Note that below jamming (the blue curve in both graphs) the contact forces are not very large in magnitude.

4.4 Conclusions

Before closing, we briefly compare our results and conclusions with previous work mentioned earlier. While the conclusion in [57] differ from ours, the sharpening of the rigidity transition has also been noted in [57]. In [55], shear was applied to frictionless disk assemblies before friction were included in the rigidity analysis. While this procedure captures many features of sheared frictional disks, like the anisotropy and the emergence of a contact network that supports jamming in the presence of friction, a subtle but important differences in the organization of contacts exist. Specifically, using the procedure of [55], the fraction of redundant bonds rises continuously from below the isostatic contact number, whereas they are strictly zero below the frictional jamming point. The absence of redundant bonds before the rigidity transition is a characteristic feature of jamming, as compared to rigidity percolation in spring networks and other systems [108]. Our results differ from the analysis of experimentally sheared disk packings in [59], for which we do not have a ready explanation, since the experimental protocol should be expected to closely agree with the quasistatic shear we employ, an inconsistency that needs to be further investigated.

In summary, our results unambiguously demonstrate that the rigidity transition associated with shear jamming in both frictionless and frictional disk packings is discontinuous in nature when conditions of force and torque balance are met. Thus, the nature of the emergence of rigidity is the same for isotropic and shear jamming. Features that suggest a continuous transition are associated with partial relaxation of unbalanced forces, as our results for finite shear rate demonstrate, but such behavior approaches discontinuous change as the shear rate vanishes. Our results thus establish a key additional element in the shared phenomenology of isotropic and shear jamming.

Chapter 5

Conclusions and future directions

5.1 Summary of observations and results

The main contribution of this thesis is the characterization of the frictionless soft-sphere systems under shear deformation and uniting the rigidity transition in isotropic and shear jamming in frictional and frictionless systems. We have shown that a frictionless system is a simple model where various behavior of real granular material can be observed like shear jamming and dilatancy. We have shown that shear jamming and dilatancy are essentially the same phenomena with the former manifesting when sheared under constant volume ensemble and the former under constant pressure ensemble. We have also characterized the criticality of the shear jamming transition. It is explicitly shown that much of the critical behavior associated with isotropic jamming can be observed for the shear jamming transition as well. It is shown that shear jammed packings are marginally stable, again a feature it shares with isotropic jamming. However, the geometry of the contact network of shear jammed and isotropically jammed configurations differ from each other. The contact network of the shear jammed configurations are anisotropic. This in turn has implications for the stiffness matrix of the jammed configurations. The eigenvalues and the eigenvectors of the stiffness matrix represent moduli and strains respectively. At jamming (both shear and isotropic) only one eigenvalue is non-zero. For isotropic jamming, this eigenvalue corresponds to the bulk modulus and the for shear jamming this eigenvalue corresponds to both shear and bulk modulus. Similarly, the eigenvector associated with the non-zero eigenvalue (first eigenvector) corresponds to compressive strain for isotropically jammed configurations while for shear jammed configurations the first eigenvector is a linear combination of compressive and shear strain. We have shown that the projection of the first eigenvector onto the shear strain is proportional to the anisotropy of the configuration.

The picture that emerges from the above observations is that there is no “typical” jammed configuration. The nature of the jammed configuration depends on how that jammed configuration was arrived at and the path is remembered in the geometry of the contact network. Nevertheless various other critical properties like isostaticity, scaling of excess contact number, pressure, force, and gap exponents, etc are universal for all jammed configurations. In addition to the above observations, the rigidity transition in frictional and frictionless shear jamming has been shown to be a discontinuous transition. This makes discontinuous rigidity transition a feature of jamming of repulsive disks.

5.2 Future directions

Here I outline a few directions of research which could be pursued.

5.2.1 On the marginal stability condition

A central assumption in the derivation is that there are contacts for which the response when opened is either localized or extended. While evidently this assumption seems to hold, it would be interesting to explicitly show these responses. Response in large systems does not tend to extend all over the system, they are localized forces. Do these responses tend to extend across the system if the interaction gets “stiffer”? As shown by Vinutha *et al* [55], the force balance solutions on the contact network generated from frictionless disks with friction added obey the marginal stability condition. It would be interesting to show this from the DEM simulations.

5.2.2 On the non-monotonicity of the anisotropy for shear jammed states with $\phi > \phi_J$

As shown in Fig. 3.3 and Fig. 3.5 the anisotropy of shear jammed configurations vary non-monotonically as density is varied from ϕ_J to ϕ_j. A possible explanation is as follows. We can understand that the anisotropy should tend to zero as we approach ϕ_j as configurations near ϕ_j jam at very small strains. Therefore the configurations will tend to be nearly isotropic when shear jammed. How do we understand the decreased anisotropy of shear jammed configurations near ϕ_J? When sphere packings are sheared initially the contact network is formed along the compressive direction. Upon further shearing the contact network is developed along the dilative direction as well. So the anisotropy is maximum where the contact network is predominantly along the compressive direction. Shear jamming occurs when the contact network crosses the isostatic point, so the above-described behavior could be happening independently of shear jamming. That is, for configurations under shear near ϕ_J, jamming happens at large strains where the contact network is more isotropic (where the contact network has formed along both compressive and dilative directions). It would be interesting to explain the non-monotonicity of the fabric anisotropy and this would require a definition of contact network for unjammed configurations - a way to identify just touching contacts.

Additionally, can we observe this non-monotonic anisotropy for frictional shear jamming below ϕ_J? One can imagine that the frictional shear jammed configurations near ϕ_J is isotropic as they jam at a small strain thereby similar to the behavior of frictionless shear jamming near ϕ_j. Similarly, there is a minimum density below which frictional shear jamming cannot be experienced - similar to ϕ_J in frictionless shear jamming.

5.2.3 Timescale divergence associated with jamming

We have described before how the jamming transition shows many features of a second order transition. However, some quantities jump to a non-zero value at the jamming transition like the average coordination number and the largest eigenvalue of the stiffness matrix, which is the bulk modulus for isotropic jamming and both the bulk and shear modulus for shear jamming. Nevertheless, there are length scales associated with jamming [95, 12] that diverge at the jamming point, supporting the picture that the transition could of continuous nature. The natural question that arises is if there is a timescale that diverges at the jamming transition. Such a timescale has been discovered for frictional shear jamming [69]. A similar diverging timescale associated with frictionless jamming, both isotropic as well as shear can also be found [116, 117]. For quasi-static deformation, this manifests as an increasingly large number of iterations that are required for the minimization algorithm to converge near the jamming transition.

The question I would like to address is what this divergence says about the potential energy landscape at the jamming transition. It has been shown that the potential energy landscape near the jamming transition is ultrametric and hierarchical, reflecting the marginal stability condition [118]. Perhaps one can show this nature of the landscape using the diverging timescale.

Bibliography

[1] MD Rintoul and Salvatore Torquato. Computer simulations of dense hard-sphere systems. *The Journal of chemical physics*, 105(20):9258–9265, 1996. (page 9).

[2] Jean-Pierre Hansen and Ian Ranald McDonald. *Theory of simple liquids: with applications to soft matter*. Academic press, 2013. (page 9, 9).

[3] Norman F Carnahan and Kenneth E Starling. Equation of state for nonattracting rigid spheres. *The Journal of chemical physics*, 51(2):635–636, 1969. (page 10).

[4] Michio Tokuyama and Yayoi Terada. Slow dynamics and re-entrant melting in a polydisperse hard-sphere fluid. *The Journal of Physical Chemistry B*, 109(45):21357–21363, 2005. (page 10).

[5] Pinaki Chaudhuri, Ludovic Berthier, and Srikanth Sastry. Jamming transitions in amorphous packings of frictionless spheres occur over a continuous range of volume fractions. *Physical review letters*, 104(16):165701, 2010. (pages 11, 28, 28, 28, 30, 42, 46, 48, 48).

[6] Misaki Ozawa, Takeshi Kuroiwa, Atsushi Ikeda, and Kunimasa Miyazaki. Jamming transition and inherent structures of hard spheres and disks. *Physical review letters*, 109(20):205701, 2012. (pages 11, 28, 28, 28).

[7] Michael P Allen and Dominic J Tildesley. *Computer simulation of liquids*. Oxford university press, 2017. (page 11).

[8] Corey S O'Hern, Leonardo E Silbert, Andrea J Liu, and Sidney R Nagel. Jamming at zero temperature and zero applied stress: The epitome of disorder. *Physical Review E*, 68(1):011306, 2003. (pages 12, 12, 12, 12, 12, 15, 15, 30, 40, 42, 46, 46, 46, 63).

[9] M van Hecke. Jamming of soft particles: geometry, mechanics, scaling and isostaticity. *J. Phys. Condens. Matter*, 22(3):033101, 2009. (pages 12, 12, 12, 12, 15, 15, 46, 46).

[10] Adrian Baule, Flaviano Morone, Hans J Herrmann, and Hernán A Makse. Edwards statistical mechanics for jammed granular matter. *Reviews of modern physics*, 90(1):015006, 2018. (pages 12, 14, 15).

[11] Wouter G Ellenbroek, Ellák Somfai, Martin van Hecke, and WIM vAN SAARLoos. Critical scaling in linear response of frictionless granular packings near jamming. *Physical review letters*, 97(25):258001, 2006. (pages 13, 21, 22).

[12] Andrea J Liu and Sidney R Nagel. The jamming transition and the marginally jammed solid. *Annu. Rev. Condens. Matter Phys.*, 1(1):347–369, 2010. (pages 13, 14, 46, 46, 46, 46, 89).

[13] Bingyu Cui, Giancarlo Ruocco, and Alessio Zaccone. Theory of elastic constants of athermal amorphous solids with internal stresses. *Granular Matter*, 21(3):1–6, 2019. (page 14).

[14] Matthieu Wyart, Sidney R Nagel, and Thomas A Witten. Geometric origin of excess low-frequency vibrational modes in weakly connected amorphous solids. *EPL (Europhysics Letters)*, 72(3):486, 2005. (pages 14, 14, 46, 52).

[15] Eric DeGiuli, Adrien Laversanne-Finot, Gustavo Düring, Edan Lerner, and Matthieu Wyart. Effects of coordination and pressure on sound attenuation, boson peak and elasticity in amorphous solids. *Soft Matter*, 10(30):5628–5644, 2014. (page 14, 14).

[16] Hideyuki Mizuno, Hayato Shiba, and Atsushi Ikeda. Continuum limit of the vibrational properties of amorphous solids. *Proceedings of the National Academy of Sciences*, 114(46):E9767–E9774, 2017. (page 14).

[17] Ning Xu, Vincenzo Vitelli, Andrea J Liu, and Sidney R Nagel. Anharmonic and quasi-localized vibrations in jammed solidsâmodes for mechanical failure. *EPL (Europhysics Letters)*, 90(5):56001, 2010. (page 14).

[18] Leonardo E Silbert, Deniz Ertaş, Gary S Grest, Thomas C Halsey, and Dov Levine. Geometry of frictionless and frictional sphere packings. *Physical Review E*, 65(3):031304, 2002. (page 15).

[19] Leonardo E Silbert, Andrea J Liu, and Sidney R Nagel. Structural signatures of the unjamming transition at zero temperature. *Physical Review E*, 73(4):041304, 2006. (page 15).

[20] Aleksandar Donev, Salvatore Torquato, and Frank H Stillinger. Pair correlation function characteristics of nearly jammed disordered and ordered hard-sphere packings. *Physical Review E*, 71(1):011105, 2005. (page 15).

[21] Patrick Charbonneau, Eric I Corwin, Giorgio Parisi, and Francesco Zamponi. Universal microstructure and mechanical stability of jammed packings. *Physical review letters*, 109(20):205501, 2012. (pages 15, 46, 46, 57).

[22] Edan Lerner, Gustavo Düring, and Matthieu Wyart. Low-energy non-linear excitations in sphere packings. *Soft Matter*, 9(34):8252–8263, 2013. (pages 15, 15, 15, 20, 20, 20, 21, 46, 46, 46, 55, 55, 57).

[23] Matthieu Wyart. Marginal stability constrains force and pair distributions at random close packing. *Physical review letters*, 109(12):125502, 2012. (pages 15, 15, 46, 46).

[24] Patrick Charbonneau, Eric I Corwin, Giorgio Parisi, and Francesco Zamponi. Jamming criticality revealed by removing localized buckling excitations. *Physical review letters*, 114(12):125504, 2015. (pages 15, 16, 16, 21, 21, 46, 47, 48, 48, 48, 55, 56).

[25] Yoav Kallus and Salvatore Torquato. Marginal stability in jammed packings: Quasicontacts and weak contacts. *Physical Review E*, 90(2):022114, 2014. (page 20).

[26] Patrick Charbonneau, Eric I. Corwin, R. Cameron Dennis, Rafael Díaz Hernández Rojas, Harukuni Ikeda, Giorgio Parisi, and Federico Ricci-Tersenghi. Finite-size effects in the microscopic critical properties of jammed configurations: A comprehensive study of the effects of different types of disorder. *Phys. Rev. E*, 104:014102, Jul 2021. (pages 21, 21, 57, 57, 59).

[27] Rafael Díaz Hernández Rojas, Giorgio Parisi, and Federico Ricci-Tersenghi. Inferring the particle-wise dynamics of amorphous solids from the local structure at the jamming point. *Soft Matter*, 17(4):1056–1083, 2021. (page 21).

[28] Giorgio Parisi, Pierfrancesco Urbani, and Francesco Zamponi. *Theory of simple glasses: exact solutions in infinite dimensions.* Cambridge University Press, 2020. (pages 21, 21, 46).

[29] Giorgio Parisi and Francesco Zamponi. Amorphous packings of hard spheres for large space dimension. *Journal of Statistical Mechanics: Theory and Experiment*, 2006(03):P03017, 2006. (page 21).

[30] Giorgio Parisi and Francesco Zamponi. Mean-field theory of hard sphere glasses and jamming. *Reviews of Modern Physics*, 82(1):789, 2010. (pages 21, 28).

[31] Jorge Kurchan, Giorgio Parisi, and Francesco Zamponi. Exact theory of dense amorphous hard spheres in high dimension i. the free energy. *Journal of Statistical Mechanics: Theory and Experiment*, 2012(10):P10012, 2012. (page 21).

[32] Jorge Kurchan, Giorgio Parisi, Pierfrancesco Urbani, and Francesco Zamponi. Exact theory of dense amorphous hard spheres in high dimension. ii. the high density regime and the gardner transition. *The Journal of Physical Chemistry B*, 117(42):12979–12994, 2013. (page 21).

[33] Patrick Charbonneau, Jorge Kurchan, Giorgio Parisi, Pierfrancesco Urbani, and Francesco Zamponi. Exact theory of dense amorphous hard spheres in high dimension. iii. the full replica symmetry breaking solution. *Journal of Statistical Mechanics: Theory and Experiment*, 2014(10):P10009, 2014. (page 21).

[34] Leonardo E Silbert. Jamming of frictional spheres and random loose packing. *Soft Matter*, 6(13):2918–2924, 2010. (pages 21, 22).

[35] Silke Henkes, Martin van Hecke, and Wim van Saarloos. Critical jamming of frictional grains in the generalized isostaticity picture. *EPL (Europhysics Letters)*, 90(1):14003, 2010. (pages 22, 66, 83).

[36] TS Majmudar, M Sperl, Stefan Luding, and Robert P Behringer. Jamming transition in granular systems. *Physical review letters*, 98(5):058001, 2007. (page 22).

[37] Dapeng Bi, Jie Zhang, Bulbul Chakraborty, and Robert P Behringer. Jamming by shear. *Nature*, 480(7377):355–358, 2011. (pages 22, 23, 28, 28, 46).

[38] Ivo R Peters, Sayantan Majumdar, and Heinrich M Jaeger. Direct observation of dynamic shear jamming in dense suspensions. *Nature*, 532(7598):214–217, 2016. (page 22).

[39] Daniel Bonn, Morton M Denn, Ludovic Berthier, Thibaut Divoux, and Sébastien Manneville. Yield stress materials in soft condensed matter. *Reviews of Modern Physics*, 89(3):035005, 2017. (page 22).

[40] Alexandre Nicolas, Ezequiel E Ferrero, Kirsten Martens, and Jean-Louis Barrat. Deformation and flow of amorphous solids: Insights from elastoplastic models. *Reviews of Modern Physics*, 90(4):045006, 2018. (page 22).

[41] M E Cates, J P Wittmer, J.-P. Bouchaud, and P Claudin. Jamming, force chains, and fragile matter. *Phys. Rev. Lett.*, 81:1841–1844, 1998. (pages 22, 22, 28).

[42] Jie Ren. *Nonlinear dynamics and network properties in granular materials under shear*. PhD thesis, Duke University, 2013. (page 23).

[43] Trushant S Majmudar and Robert P Behringer. Contact force measurements and stress-induced anisotropy in granular materials. *nature*, 435(7045):1079–1082, 2005. (page 23).

[44] Jie Ren, Joshua A Dijksman, and Robert P Behringer. Reynolds pressure and relaxation in a sheared granular system. *Physical review letters*, 110(1):018302, 2013. (pages 24, 28, 28, 28, 39, 46).

[45] Osborne Reynolds. Lvii. on the dilatancy of media composed of rigid particles in contact. with experimental illustrations. *The London, Edinburgh, and Dublin Philosophical Magazine and Journal of Science*, 20(127):469–481, 1885. (pages 24, 28, 28, 44).

[46] Michio Otsuki and Hisao Hayakawa. Critical scaling near jamming transition for frictional granular particles. *Physical Review E*, 83(5):051301, 2011. (page 24).

[47] Massimo Pica Ciamarra, Raffaele Pastore, Mario Nicodemi, and Antonio Coniglio. Jamming phase diagram for frictional particles. *Physical Review E*, 84(4):041308, 2011. (page 24).

[48] Pierre-Emmanuel Peyneau and Jean-Noël Roux. Frictionless bead packs have macroscopic friction, but no dilatancy. *Physical review E*, 78(1):011307, 2008. (pages 24, 28, 29, 29, 38, 40, 42, 44).

[49] Emilien Azema, Farhang Radjai, and Jean-Noël Roux. Internal friction and absence of dilatancy of packings of frictionless polygons. *Physical Review E*, 91(1):010202, 2015. (pages 24, 28, 44).

[50] Marco Baity-Jesi, Carl P Goodrich, Andrea J Liu, Sidney R Nagel, and James P Sethna. Emergent SO (3) symmetry of the frictionless shear jamming transition. *Journal of Statistical Physics*, 167(3-4):735–748, 2017. (pages 24, 24, 25, 28, 29, 29, 46, 46, 47, 52, 52, 52, 59).

[51] Thibault Bertrand, Robert P Behringer, Bulbul Chakraborty, Corey S O'Hern, and Mark D Shattuck. Protocol dependence of the jamming transition. *Physical Review E*, 93(1):012901, 2016. (pages 24, 29, 46).

[52] H. A. Vinutha and Srikanth Sastry. Disentangling the role of structure and friction in shear jamming. *Nature Physics*, 12(6):578–583, 2016. (pages 24, 24, 28, 29, 46, 62, 66).

[53] Pallabi Das, H. A. Vinutha, and Srikanth Sastry. Unified phase diagram of reversible–irreversible, jamming, and yielding transitions in cyclically sheared soft-sphere packings. *Proceedings of the National Academy of Sciences*, 117(19):10203–10209, 2020. (pages 24, 30, 31, 48, 63).

[54] Nishant Kumar and Stefan Luding. Memory of jamming–multiscale models for soft and granular matter. *Granular Matter*, 18(3):1–21, 2016. (pages 24, 28, 38, 46, 63).

[55] H. A. Vinutha and Srikanth Sastry. Force networks and jamming in shear-deformed sphere packings. *Physical Review E*, 99(1):012123, 2019. (pages 24, 46, 47, 62, 62, 66, 71, 81, 82, 86, 86, 89).

[56] Wouter G Ellenbroek, Varda F Hagh, Avishek Kumar, MF Thorpe, and Martin Van Hecke. Rigidity loss in disordered systems: Three scenarios. *Physical review letters*, 114(13):135501, 2015. (pages 25, 62).

[57] Silke Henkes, David A Quint, Yaouen Fily, and Jennifer M Schwarz. Rigid cluster decomposition reveals criticality in frictional jamming. *Physical review letters*, 116(2):028301, 2016. (pages 25, 62, 62, 62, 71, 71, 71, 80, 83, 86, 86).

[58] Kuang Liu, Silke Henkes, and JM Schwarz. Frictional rigidity percolation: A new universality class and its superuniversal connections through minimal rigidity proliferation. *Physical Review X*, 9(2):021006, 2019. (pages 25, 62, 62).

[59] Kuang Liu, Jonathan E Kollmer, Karen E Daniels, JM Schwarz, and Silke Henkes. Spongelike rigid structures in frictional granular packings. *Physical Review Letters*, 126(8):088002, 2021. (pages 25, 62, 62, 71, 71, 86).

[60] Dion J Koeze and Brian P Tighe. Sticky matters: Jamming and rigid cluster statistics with attractive particle interactions. *Physical review letters*, 121(18):188002, 2018. (page 25).

[61] Andrea J Liu and Sidney R Nagel. Nonlinear dynamics: Jamming is not just cool any more. *Nature*, 396(6706):21, 1998. (pages 28, 29, 42).

[62] Robin J Speedy. On the reproducibility of glasses. *The Journal of chemical physics*, 100(9):6684–6691, 1994. (page 28).

[63] Robin J Speedy and Pablo G Debenedetti. The distribution of tetravalent network glasses. *Molecular Physics*, 88(5):1293–1316, 1996. (page 28).

[64] Robin J Speedy. Random jammed packings of hard discs and spheres. *Journal of Physics: Condensed Matter*, 10(19):4185, 1998. (page 28).

[65] Florent Krzakala and Jorge Kurchan. Landscape analysis of constraint satisfaction problems. *Physical Review E*, 76(2):021122, 2007. (page 28).

[66] Romain Mari, Florent Krzakala, and Jorge Kurchan. Jamming versus glass transitions. *Physical review letters*, 103(2):025701, 2009. (page 28).

[67] Sumantra Sarkar, Dapeng Bi, Jie Zhang, Robert P. Behringer, and Bulbul Chakraborty. Origin of rigidity in dry granular solids. *Phys. Rev. Lett.*, 111(6):068301, 2013. (page 28, 28).

[68] Sumantra Sarkar, Dapeng Bi, Jie Zhang, Jie Ren, R. P. Behringer, and Bulbul Chakraborty. Shear-induced rigidity of frictional particles: Analysis of emergent order in stress space. *Phys. Rev. E*, 93:042901, Apr 2016. (pages 28, 28, 38).

[69] H. A. Vinutha, Kabir Ramola, Bulbul Chakraborty, and Srikanth Sastry. Timescale divergence at the shear jamming transition. *Granular Matter*, 22(1):1–8, 2020. (pages 28, 46, 47, 65, 70, 77, 89).

[70] Ryohei Seto, Romain Mari, Jeffrey F Morris, and Morton M Denn. Discontinuous shear thickening of frictional hard-sphere suspensions. *Physical review letters*, 111(21):218301, 2013. (page 28, 28).

[71] Michio Otsuki and Hisao Hayakawa. Discontinuous change of shear modulus for frictional jammed granular materials. *Phys. Rev. E*, 95:062902, Jun 2017. (page 28, 28).

[72] Michio Otsuki and Hisao Hayakawa. Shear jamming, discontinuous shear thickening, and fragile states in dry granular materials under oscillatory shear. *Physical Review E*, 101(3):032905, 2020. (pages 28, 28, 38).

[73] Yuliang Jin, Pierfrancesco Urbani, Francesco Zamponi, and Hajime Yoshino. A stability-reversibility map unifies elasticity, plasticity, yielding, and jamming in hard sphere glasses. *Science advances*, 4(12):eaat6387, 2018. (pages 28, 46).

[74] Yiqiu Zhao, Jonathan Barés, Hu Zheng, Joshua E. S. Socolar, and Robert P. Behringer. Shear-jammed, fragile, and steady states in homogeneously strained granular materials. *Phys. Rev. Lett.*, 123:158001, Oct 2019. (pages 28, 38).

[75] Yuliang Jin and Hajime Yoshino. Exploring the complex free-energy landscape of the simplest glass by rheology. *Nature communications*, 8(1):1–8, 2017. (pages 28, 46).

[76] Pierfrancesco Urbani and Francesco Zamponi. Shear yielding and shear jamming of dense hard sphere glasses. *Physical review letters*, 118(3):038001, 2017. (pages 28, 29, 39, 47).

[77] Nicolaas P Kruyt and L Rothenburg. A micromechanical study of dilatancy of granular materials. *Journal of the Mechanics and Physics of Solids*, 95:411–427, 2016. (page 28).

[78] K Kesava Rao and Prabhu R Nott. *An introduction to granular flow/K. Kesava Rao, Prabhu R. Nott.* 2008. (page 28).

[79] Peter W Rowe. The stress-dilatancy relation for static equilibrium of an assembly of particles in contact. *Proceedings of the Royal Society of London. Series A. Mathematical and Physical Sciences*, 269(1339):500–527, 1962. (page 28).

[80] Robert P Behringer and Bulbul Chakraborty. The physics of jamming for granular materials: a review. *Reports on Progress in Physics*, 82(1):012601, 2018. (page 28).

[81] Cécile Clavaud, Antoine Bérut, Bloen Metzger, and Yoël Forterre. Revealing the frictional transition in shear-thickening suspensions. *Proceedings of the National Academy of Sciences*, 114(20):5147–5152, 2017. (page 28).

[82] Corrado Rainone, Pierfrancesco Urbani, Hajime Yoshino, and Francesco Zamponi. Following the evolution of hard sphere glasses in infinite dimensions under external perturbations: Compression and shear strain. *Physical review letters*, 114(1):015701, 2015. (page 29).

[83] Steve Plimpton. Fast parallel algorithms for short-range molecular dynamics. *Journal of computational physics*, 117(1):1–19, 1995. (pages 29, 48, 63).

[84] Erik Bitzek, Pekka Koskinen, Franz Gähler, Michael Moseler, and Peter Gumbsch. Structural relaxation made simple. *Physical review letters*, 97(17):170201, 2006. (pages 30, 31).

[85] Ludovic Berthier, Daniele Coslovich, Andrea Ninarello, and Misaki Ozawa. Equilibrium sampling of hard spheres up to the jamming density and beyond. *Phys. Rev. Lett.*, 116:238002, Jun 2016. (page 30, 30).

[86] Ludovic Berthier, Patrick Charbonneau, Yuliang Jin, Giorgio Parisi, Beatriz Seoane, and Francesco Zamponi. Growing timescales and lengthscales characterizing vibrations of amorphous solids. *Proceedings of the National Academy of Sciences*, 113(30):8397–8401, 2016. (page 30).

[87] Sumantra Sarkar, Elan Shatoff, Kabir Ramola, Romain Mari, Jeffrey Morris, and Bulbul Chakraborty. Shear-induced organization of forces in dense suspensions: signatures of discontinuous shear thickening. In *EPJ Web of Conferences*, volume 140. EDP Sciences, 2017. (page 38).

[88] Ryohei Seto, Abhinendra Singh, Bulbul Chakraborty, Morton M Denn, and Jeffrey F Morris. Shear jamming and fragility in dense suspensions. *Granular Matter*, 21(3):82, 2019. (page 38).

[89] Brian P Tighe. Shear dilatancy in marginal solids. *Granular Matter*, 16(2):203–208, 2014. (page 39).

[90] Ada Altieri and Francesco Zamponi. Mean-field stability map of hard-sphere glasses. *Physical Review E*, 100(3):032140, 2019. (page 40).

[91] Wen Zheng, Shiyun Zhang, and Ning Xu. Jamming of packings of frictionless particles with and without shear. *Chinese Physics B*, 27(6):066102, 2018. (page 40, 40).

[92] Claus Heussinger and Jean-Louis Barrat. Jamming transition as probed by quasistatic shear flow. *Physical review letters*, 102(21):218303, 2009. (page 42).

[93] Yuliang Jin and Hajime Yoshino. A jamming plane of sphere packings. *Proceedings of the National Academy of Sciences*, 118(14), 2021. (pages 44, 46, 47, 47, 52, 57, 59).

[94] Takeshi Kawasaki and Kunimasa Miyazaki. Shear jamming and shear melting in mechanically trained frictionless particles. *arXiv preprint arXiv:2003.10716*, 2020. (page 44).

[95] M Wyart. On the rigidity of amorphous solids. In *Annales de Physique*, volume 30, pages 1–96, 2005. (pages 46, 52, 89).

[96] Matthieu Wyart, Leonardo E Silbert, Sidney R Nagel, and Thomas A Witten. Effects of compression on the vibrational modes of marginally jammed solids. *Physical Review E*, 72(5):051306, 2005. (page 46).

[97] Carl P. Goodrich, Andrea J. Liu, and James P. Sethna. Scaling ansatz for the jamming transition. *Proceedings of the National Academy of Sciences*, 113(35):9745–9750, 2016. (page 46).

[98] Gaël Combe and Jean-Noël Roux. Strain versus stress in a model granular material: a devil's staircase. *Physical Review Letters*, 85(17):3628, 2000. (page 46).

[99] Patrick Charbonneau, Jorge Kurchan, Giorgio Parisi, Pierfrancesco Urbani, and Francesco Zamponi. Glass and jamming transitions: From exact results to finite-dimensional descriptions. *Annual Review of Condensed Matter Physics*, 8:265–288, 2017. (page 46).

[100] Eric DeGiuli, Edan Lerner, Carolina Brito, and Matthieu Wyart. Force distribution affects vibrational properties in hard-sphere glasses. *Proceedings of the National Academy of Sciences*, 111(48):17054–17059, 2014. (page 46).

[101] Varghese Babu, Deng Pan, Yuliang Jin, Bulbul Chakraborty, and Srikanth Sastry. Dilatancy, shear jamming, and a generalized jamming phase diagram of frictionless sphere packings. *Soft Matter*, 17(11):3121–3127, 2021. (pages 46, 48, 63, 70).

[102] Anton Peshkov and S Teitel. Critical scaling of compression-driven jamming of athermal frictionless spheres in suspension. *Physical Review E*, 103(4):L040901, 2021. (pages 46, 47).

[103] Joshua A Anderson, M Eric Irrgang, and Sharon C Glotzer. Scalable metropolis monte carlo for simulation of hard shapes. *Computer Physics Communications*, 204:21–30, 2016. (page 48).

[104] Joshua A Anderson, Jens Glaser, and Sharon C Glotzer. Hoomd-blue: A python package for high-performance molecular dynamics and hard particle monte carlo simulations. *Computational Materials Science*, 173:109363, 2020. (pages 48, 63).

[105] Anaël Lemaître and Craig Maloney. Sum rules for the quasi-static and visco-elastic response of disordered solids at zero temperature. *Journal of statistical physics*, 123(2):415–453, 2006. (pages 50, 51).

[106] Carl P Goodrich, Simon Dagois-Bohy, Brian P Tighe, Martin van Hecke, Andrea J Liu, and Sidney R Nagel. Jamming in finite systems: Stability, anisotropy, fluctuations, and scaling. *Physical Review E*, 90(2):022138, 2014. (page 51).

[107] DJ Jacobs and MF Thorpe. Generic rigidity percolation in two dimensions. *Physical Review E*, 53(4):3682, 1996. (pages 62, 66).

[108] MV Chubynsky, M-A Brière, and Normand Mousseau. Self-organization with equilibration: A model for the intermediate phase in rigidity percolation. *Physical Review E*, 74(1):016116, 2006. (pages 62, 86).

[109] Varghese Babu and Srikanth Sastry. Criticality and marginal stability of the shear jamming transition of frictionless soft spheres. *Physical Review E*, 105(4):L042901, 2022. (pages 63, 70).

[110] P. A. Cundall and O. D. L. Strack. A discrete numerical model for granular assemblies. *Geotechnique*, 29:47–65, 1979. (page 63).

[111] Stefan Luding. Cohesive, frictional powders: contact models for tension. *Granular matter*, 10(4):235–246, 2008. (page 65).

[112] Kostya Shundyak, Martin van Hecke, and Wim van Saarloos. Force mobilization and generalized isostaticity in jammed packings of frictional grains. *Physical Review E*, 75(1):010301, 2007. (pages 66, 66, 83).

[113] Gerard Laman. On graphs and rigidity of plane skeletal structures. *Journal of Engineering mathematics*, 4(4):331–340, 1970. (page 66).

[114] Donald J Jacobs and Bruce Hendrickson. An algorithm for two-dimensional rigidity percolation: the pebble game. *Journal of Computational Physics*, 137(2):346–365, 1997. (pages 67, 70, 82).

[115] Audrey Lee and Ileana Streinu. Pebble game algorithms and sparse graphs. *Discrete Mathematics*, 308(8):1425–1437, 2008. (page 67).

[116] Atsushi Ikeda, Takeshi Kawasaki, Ludovic Berthier, Kuniyasu Saitoh, and Takahiro Hatano. Universal relaxation dynamics of sphere packings below jamming. *Physical review letters*, 124(5):058001, 2020. (page 89).

[117] Ye Yuan, Weiwei Jin, Lufeng Liu, and Shuixiang Li. Shape effects on time-scale divergence at athermal jamming transition of frictionless non-spherical particles. *Physica A: Statistical Mechanics and its Applications*, 484:470–481, 2017. (page 89).

[118] RC Dennis and EI Corwin. Jamming energy landscape is hierarchical and ultrametric. *Physical review letters*, 124(7):078002, 2020. (page 90).